The Thesis Committee for Mustafa Badieh Al-Waily
Certifies that this is the approved version of the following thesis:

Depth-Registration of 9-Component 3-Dimensional Seismic Data in Stephens County, Oklahoma

APPROVED BY
SUPERVISING COMMITTEE:

Supervisor:

Bob Hardage

Kyle Spikes

Robert Tatham

Depth-Registration of 9-Component 3-Dimensional Seismic Data in Stephens County, Oklahoma

by

Mustafa Badieh Al-Waily, B.S.

Thesis

Presented to the Faculty of the Graduate School of
The University of Texas at Austin
in Partial Fulfillment
of the Requirements
for the Degree of

Master of Science in Geological Sciences

The University of Texas at Austin
May 2014

Dedication

I want to dedicate this work to my family and many friends. A special gratitude goes to my loving parents, Badeea Al-Waily and Ibtisam Ibrahim, whose words of encouragement pushed me towards the completion of my degree. My brother and sister, Ali and Sarah, were a source of constant moral support. A distance of 7,391 miles did not stop them from being there for me every single day. I also dedicate this work to my friends and colleagues for their love and support.

Acknowledgements

A special thanks to Dr. Bob A. Hardage, my supervisor, for his countless hours of reflecting, reading, encouraging, and patience throughout the entire process. I wish to thank my committee members, Dr. Kyle T. Spikes and Dr. Robert H. Tatham, who were extremely generous with their expertise and precious time. Thank you for agreeing to serve on my committee.

Thanks to the Exploration Geophysics Lab, Bureau of Economic Geology, for providing the 9C/3D seismic data. Special thanks to Michael V. DeAngelo and Randy L. Remington for setting up and helping me interpret seismic data and well data. Many thanks to Dr. William L. Fisher and Dr. Michael R. Hudec for helping me understand the structural geology of the area of interest. Landmark Graphics Corporation provided software for the basic 9C/3D seismic interpretation via their University Grant Program.

Thanks to the Jackson School of Geosciences for allowing me to conduct my research and for providing all the assistance needed. Thanks to the members of staff development and human resources department for their continued support. Special thanks to Philip Guerrero, the graduate program administrator, for his help and support. Many thanks to Thomas Hess and the Oklahoma Geological Survey for providing the well data used in this analysis. Thanks to Bob Penman for providing the thesis template. Thanks to Mohammed Alsaedi for listening to my work every day, and to Rebecca Morrison for proofreading my thesis.

Finally, thanks to my family, friends, and colleagues who endured this long process with me. Their love and support made this research an enjoyable experience.

Abstract

Depth-Registration of 9-Component 3-Dimensional Seismic Data in Stephens County, Oklahoma

Mustafa Badieh Al-Waily, M.S. Geo. Sci.
The University of Texas at Austin, 2014

Supervisor: Bob Hardage

Multicomponent seismic imaging techniques improve geological interpretation by providing crucial information about subsurface characteristics. These techniques deliver different images of the same subsurface using multiple waveforms. Compressional (P) and shear (S) waves respond to lithology and fluid variations differently, providing independent measurements of rock and fluid properties.

Joint interpretation of multicomponent images requires P-wave and S-wave events to be aligned in depth. The process of identifying P and S events from the same reflector is called depth-registration. The purpose of this investigation is to illustrate procedures for depth-registering P and S seismic data when the most fundamental information needed for depth-registration – reliable velocity data – are not available.

This work will focus on the depth-registration of a 9-component 3-dimensional seismic dataset targeting the Sycamore formation in Stephens County, Oklahoma. The survey area – 16 square miles – is located in Sho-Vel-Tum oilfield. Processed P-P, SV-

SV, and SH-SH wave data are available for post-stack analysis. However, the SV-data volume will not be interpreted because of its inferior data-quality compared to the SH-data volume. Velocity data are essential in most depth-registration techniques: they can be used to convert the seismic data from the time domain to the depth domain. However, velocity data are not available within the boundaries of the 9C/3D seismic survey.

The data are located in a complex area that is folded and faulted in the northwest part of the Ardmore basin, between the eastern Arbuckle Mountains and the western Wichita Mountains. Large hydrocarbon volumes are produced from stratigraphic traps, fault closures, anticlines, and combination traps. Sho-Vel-Tum was ranked 31st in terms of proved oil reserves among U.S. oil fields by a 2009 survey.

I will interpret different depth-registered horizons on the P-wave and S-wave seismic data volumes. Then, I will present several methods to verify the accuracy of event-registration. Seven depth-registered horizons are mapped through the P-P and SH-SH seismic data. These horizons show the structural complexity that imposes serious challenges on well drilling within the Sho-Vel-Tum oil field. Interval V_p/V_s – a seismic attribute often used as lithological indicator – was mapped to constrain horizon picking and to characterize lateral stratigraphic variations.

Table of Contents

List of Tables

List of Figures

Chapter 1: Introduction

This chapter introduces the concept of multicomponent seismic data acquisition and analysis, defines relevant terminology, discusses the research problem and significance, and describes the available well and seismic data.

OVERVIEW

Multicomponent seismic techniques have been the subject of research and development in the petroleum exploration arena for many years. These techniques became more popular in the last few decades with the introduction of the horizontal vibrator. They allow the use of complete seismic elastic wavefield in seismic stratigraphic interpretation. The science of elastic wavefield seismic stratigraphy assumes that seismic wave modes behave differently depending on lithology, porosity, and pore fluids (Hardage et al., 2011a). Although multicomponent seismic technology provides challenges in acquisition and processing, interpreters appreciate any additional information that may confirm their interpretations.

A breakthrough in this technology was introduced by deploying marine four-component (4C) sensors on the sea floor. These sensors have the ability to measure converted waves (P-SV). One of the applications of 4C seismic surveys was imaging below strata having a low saturation (gas clouds) of gas because low gas saturation attenuates P-wave signals. S-wave imaging can be extremely helpful by providing more information in areas where partially gas-saturated strata overlay deeper exploration targets. Shear wave data propagating orthogonal to the vertical plane described by the source and receiver (SH) are simpler to work with because, unlike shear waves propagating along the source-receiver plane (SV), there is no energy exchange between SH and P modes or between SH and SV modes at reflecting interfaces.

A 9C/3D survey uses 3-component sources and 3-component receivers to create 3D P-P, SV-SV, and SH-SH seismic volumes. In terms of processing, similar techniques used to process SV-SV and SH-SH volumes are used for P-P volumes. P-, SV-, and SH-waves propagate at different velocities through rocks, and they have different frequency spectra and reflectivity values at stratigraphic horizons.

Depth-registration between P and S images is an important challenge for seismic interpreters working with multicomponent seismic data. Interpreters must be accurate when choosing depth-equivalent targeted data windows in P-wave and S-wave images before seismic facies and seismic sequences can be combined into an elastic wavefield stratigraphy analysis. There are several methods used by interpreters to depth-register multicomponent data through the use of VSP data, dipole-sonic logs, images of thin-bed stratigraphy, images of structure, numerical registration of horizontal or vertical slices, and interpreter judgment (Hardage et al., 2011a).

NOMINAL DEFINITIONS

Important definitions are listed below for key terms necessary to understand this work. Some terms are intended for an audience with no or basic geosciences background.

Compressional (P) waves are elastic body waves where particle motion is in the direction of propagation. Conventional seismic data are usually acquired as P-waves. This type of wave is also called primary, longitudinal, push-pull, pressure, dilatational, rarefaction, or irrotational wave. In a homogenous medium, these waves are sensitive to two elastic constants – shear modulus and incompressibility (Sheriff, 2002).

Shear (S) waves are body waves where particle motion is perpendicular to the direction of propagation. This type of wave is also called secondary, transverse, rotational, distortional, equivolumnar, or tangential wave. S-waves are polarized in different ways. In a homogenous medium, shear-waves are sensitive to only one elastic constant – rigidity. An SH-wave is an S-wave which involves only horizontal motion. An SV-wave is an S-wave whose motion is entirely within a vertical plane. Converted waves are SV-waves generated by P-waves incident on interfaces at an angle other than the normal incidence (Sheriff, 2002). Figure 1 shows the different wave modes and their direction of earth displacement.

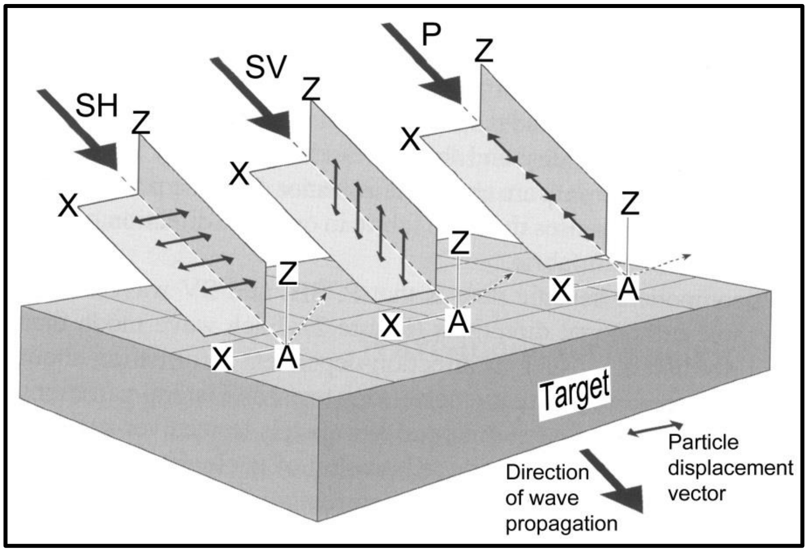

Figure 1. A full-elastic multicomponent seismic wavefield (after Hardage et al., 2011c). This seismic wavefield is composed of a compressional mode (P) and two shear modes (SV and SH) propagating through an isotropic media. A key difference to note is the direction in which the different wave modes are displacing the earth.

Sources are devices that provide energy for acquisition of seismic data, such as air guns, explosive charges or vibrators (The Oilfield Glossary, 2014).

Receivers detect the energy returned to the surface in the form of ground motion (on land) or pressure waves (marine) and transform it to electrical impulses (The Oilfield Glossary, 2014).

Two-way-travel time (TWT) is the time required for a seismic wave to travel from its source to a reflector and return back to a receiver (The Oilfield Glossary, 2014).

Fold is the multiplicity of common-midpoint data or the number of midpoints per bin (Sheriff, 2002). It is a count of how many times a point in the subsurface is imaged by seismic data.

A sample interval is typically the interval between digital samples of a recorded-time trace.

Seismic acquisition is the process of generating and recording seismic data. There are different receiver configurations, like distributing geophones on the Earth surface, towing hydrophones behind a seismic vessel, and other methods to record the seismic signal (The Oilfield Glossary, 2014). Figure 2 shows a simple 3-D seismic acquisition grid. Points in the subsurface are mapped by multiple pairs of sources and receivers.

Seismic processing is the process of alteration of seismic data to reduce noise, improve signal and migrate seismic events to their appropriate subsurface location. It facilitates better interpretation because it makes subsurface structures and geometries more apparent (The Oilfield Glossary, 2014).

Seismic interpretation is the process of analyzing seismic data to obtain reasonable geologic models and predictions about the structures of the subsurface. It is the primary concern for geophysicists (The Oilfield Glossary, 2014).

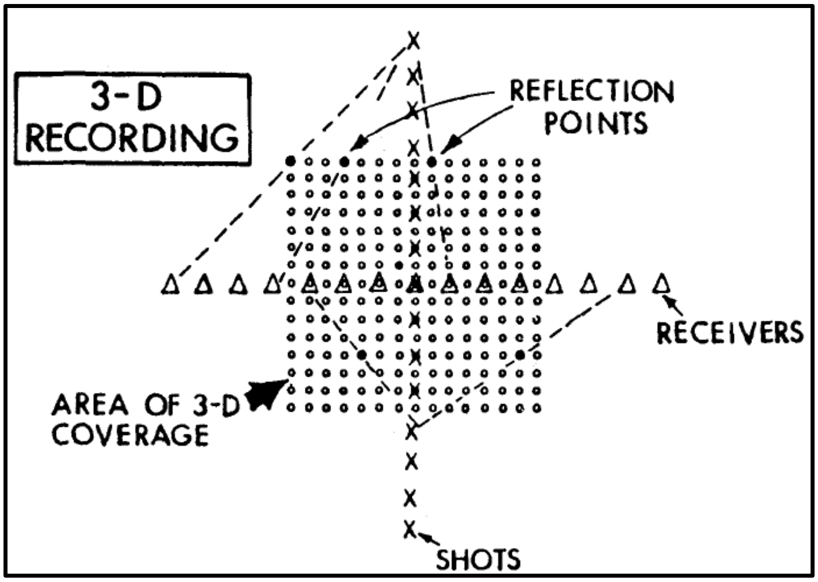

Figure 2. 3-D seismic acquisition diagram (Stommel and Graul, 1978).
Target subsurface points are imaged by multiple source-receiver pairs. The number of times a point gets imaged from a common depth point is called the "fold".

Acoustic impedance is the product of seismic wave velocity and bulk density. It is the physical property whose change determines the normal-incidence reflection coefficient (Sheriff, 2002).

Seismic reflection is the wave from a source that reflected from a subsurface reflector due to an acoustic-impedance contrast. The objective of seismic reflection analysis is to map the reflectors travel-time of primary reflections to infer geologic structure and stratigraphy (Sheriff, 2002).

The reflection coefficient is the ratio of the amplitude of the displacement of a reflected wave to that of the incident wave (Sheriff, 2002).

A synthetic seismogram, or simply a synthetic, is a result of one form of forward modeling to predict the seismic response from the subsurface. Specifically, it is a direct one-dimensional model of acoustic energy that travels through the different layers of the Earth (The Oilfield Glossary, 2014).

Gain control is a control for changing the amplification of amplifiers. It is used to compensate for changes in the strength of input signals. Automatic gain control (AGC) aims at keeping the output level within certain limits by using a feedback loop where the output level controls the gain (Sheriff, 2002).

Multicomponent seismic data are acquired in land, marine or borehole environment using receivers like geophones. 3-component (3C) seismic data involves three orthogonally-oriented geophones recording seismic signals. 4-component (4C) seismic data involves a hydrophone which adds an additional component. 9-component (9C) seismic data corresponds to the use of 3C sources and 3C receivers in the seismic acquisition stage. 9C data are acquired on land only (The Oilfield Glossary, 2014). Table 1 and Figure 3 summarize the possible options for a multicomponent seismic survey.

Table 1. Seismic data acquisition options and the wave modes associated with each case (after Hardage et al., 2011c).

Data-acquisition option	Source	Receiver	Captured mode(s)	
			Isotropic medium	Anisotropic medium
9C	XYZ	XYZ	P-P, P-SV, SV-SV, SV-P, SH-SH	P-P, P-SV_1, P-SV_2, SV_1-SV_1, SV_2-SV_2, SV_1-P, SV_2-P, SH_1-SH_1, SH_2-SH_2
6C	YZ	XYZ	P-P, P-SV, SH-SH	P-P, P-SV_1, P-SV_2, SH_1-SH_1, SH_2-SH_2
4C	Z or A	XYZH	P-P, P-SV	P-P, P-SV_1, P-SV_2
3C	Z	XYZ	P-P, P-SV	P-P, P-SV_1, P-SV_2
1C	Z	Z	P-P	P-P

X = radial, Y = transverse, Z = vertical, H = hydrophone, A = air gun, 1 = fast-S mode, 2 = slow-S mode

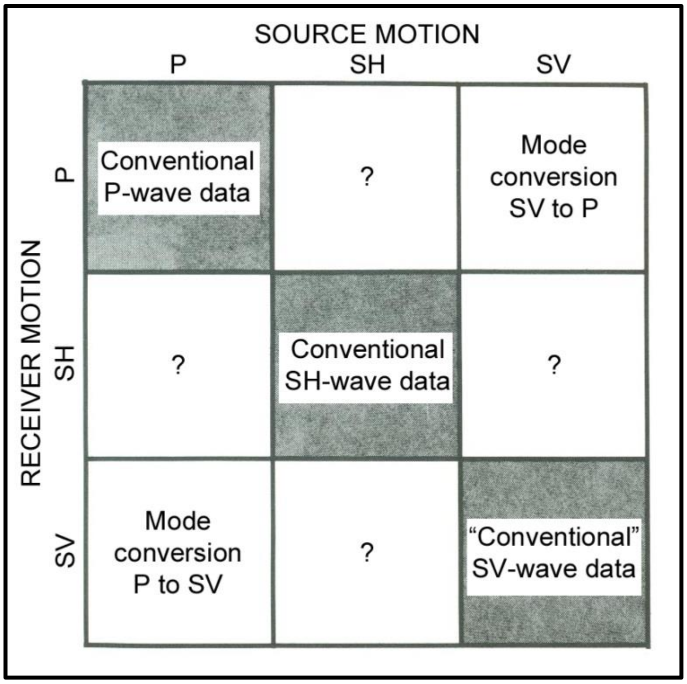

Figure 3. 9C seismology with a 3C source and a 3C receiver (after Tatham and McCormack, 1991a).
Question marks refer to some of the cross-terms that are still under research. The available data for this work is P-P, SH-SH, and SV-SV seismic volumes.

Depth-registration is the process of mapping events on P-wave data and S-wave data that are equivalent in depth. There are many quantitative and qualitative methods to achieve depth-registered events that will be discussed later in this work.

The V_p/V_s is the ratio of compressional-wave velocity to the shear-wave velocity. This ratio is an important parameter for interpreting lithology and fluid properties from seismic data and well data. For marine data, shear-wave velocity can be obtained from P-wave amplitude-variations-with-offset (AVO) analysis. For land data, the near-surface low-velocity layer often complicates S-wave data. So, it is necessary to collect both S-wave data with the P-wave data. In this case, the goal is to correlate the S-wave reflectors with their depth-equivalent P-wave reflectors (Gaiser, 1996). Using multicomponent seismic data, is it possible to approximate sand-shale ratios (McCormack et al., 1984), carbonate porosity (Robertson, 1987), limestone-dolomite content (Pardus et al., 1990), and even anisotropic parameters (Justice et al., 1987).

RESEARCH PROBLEM

P-wave and S-wave data propagate at different velocities in the subsurface. Thus, a reflection event from an interface will occur at different time coordinates in P-P image space than in S-S image space. With the lack of velocity data, depth-registration of P-wave and S-wave data becomes a more challenging task. The Sho-Vel-Tum field is structurally complex, and it is difficult to recreate the geological interpretation of the area based on well data. In this work, I will try to answer the question: is it possible to achieve good quality depth-registered horizons when no velocity data are available for guidance?

SIGNIFICANCE

This report will describe a first step in utilizing the full benefit of the seismic elastic wave field recorded by 3C geophones. Multiple horizons, including producing formations, will be depth-registered and transformed to P-wave and S-wave image times. The serious challenge of this interpretation was the lack of velocity data. This investigation will describe depth-registering techniques for P and S data when the most fundamental information needed for these techniques – reliable velocity data – is not available. Future work may utilize these results for further analysis once velocity data are obtained using sonic logs, VSPs, or velocity surveys.

SCOPE OF THE STUDY

This study focuses on depth-registration of a 9C/3D seismic dataset in Stephens County, Oklahoma. The survey area is 16 square miles and located within the Sho-Vel-Tum oil field. The data extend across a complex folded and faulted area in the northwest part of the Ardmore basin between the Arbuckle Mountains on the east and Wichita Mountains on the west. Prolific oil and gas production is obtained from stratigraphic traps, fault closures, anticlines, and combination traps. Sho-Vel-Tum was discovered in 1905, and was ranked the 31st largest oil field and 93rd largest gas field in the United States (U.S. Crude Oil, Natural Gas, and Natural Gas Liquids Proved Reserves, 2009).

DATASET

Two types of data were used: seismic data and well data. This section explains the extent and limitations of each type of data.

Seismic Data

This study uses multicomponent seismic data that were acquired by Vecta Exploration and processed by Fairfield in 1998.

Data Acquisition

A 9C/3D seismic survey was acquired over 15.8 square miles in Stephens County, Southern Oklahoma (Figure 4). The survey includes Sections 13, 24, 25, and 36 in T1N, R5W; Sections 16, 17, 18, 19, 20, 21, 28, 29, 30, 31, 32, and 33 in T1N, R4W; Sections 4, 5, and 6 in T1S, R5W; and Section 1 in T1S, R4W. Receiver spacing was 165 ft, and source spacing was 330 ft. The north-south receiver-line spacing was 1,320 ft while the east-west source-line spacing was 1,155 ft. The P-P volume has a sampling rate of 2 ms and extends to 3 seconds, whereas SH-SH and SV-SV volumes have a sampling rate of 4 ms and extend to 6 seconds. Vertical and horizontal vibrators were used to generate the 9C/3D data. P-wave data have higher signal-to-noise ratio (S/N) than S-wave data due to factors such as the higher vertical vibrator drive force as compared to that of a horizontal vibrator. Source-line and receiver-line spacing were larger than they should have been because the recording system that was deployed had only 2,000 data channels, which limited the number of 3C receivers in the acquisition template to approximately 660. Receiver spacing and receiver-line spacing had to be larger to create an acquisition template of appropriate dimensions.

This work will focus on 0 to 2 seconds of P-wave time (Figure 5) and 0 to 4 seconds of SH-wave time (Figure 6). SV-SV data were excluded because of their low S/N. The lower parts of the data volumes were cropped because of the lack of deep well control and low data quality. The fact that SH-waves reflect into only SH mode while SV-waves reflect into both SV and P modes have led some to call SH waves the "pure" shear mode (Hardage et al., 2011b, 93). They also explain that several S modes can be extracted from multicomponent seismic data, and each mode provides different geologic information. The inevitable SV to P mode conversion causes lower S/N when acquiring SV-SV data due to energy partitioning and interference of SV-SV reflections and SV-P conversions. Summing up (Hardage et al., 2011b, 95):

> Two key concepts are described by these data: (1) SV-SV data are contaminated with SV-P data but SH-SH data are not, and (2) SH velocity is different than SV velocity. Those two fundamental distinctions sometimes cause one of the S-wave modes, either SH-SH or SV-SV, to react to geologic conditions in a manner different from that of the other mode. It is often not apparent which mode, SH-SH or SV-SV, will provide more valuable information about a particular geologic target. The best policy is to acquire data that allow both S-wave images to be created.

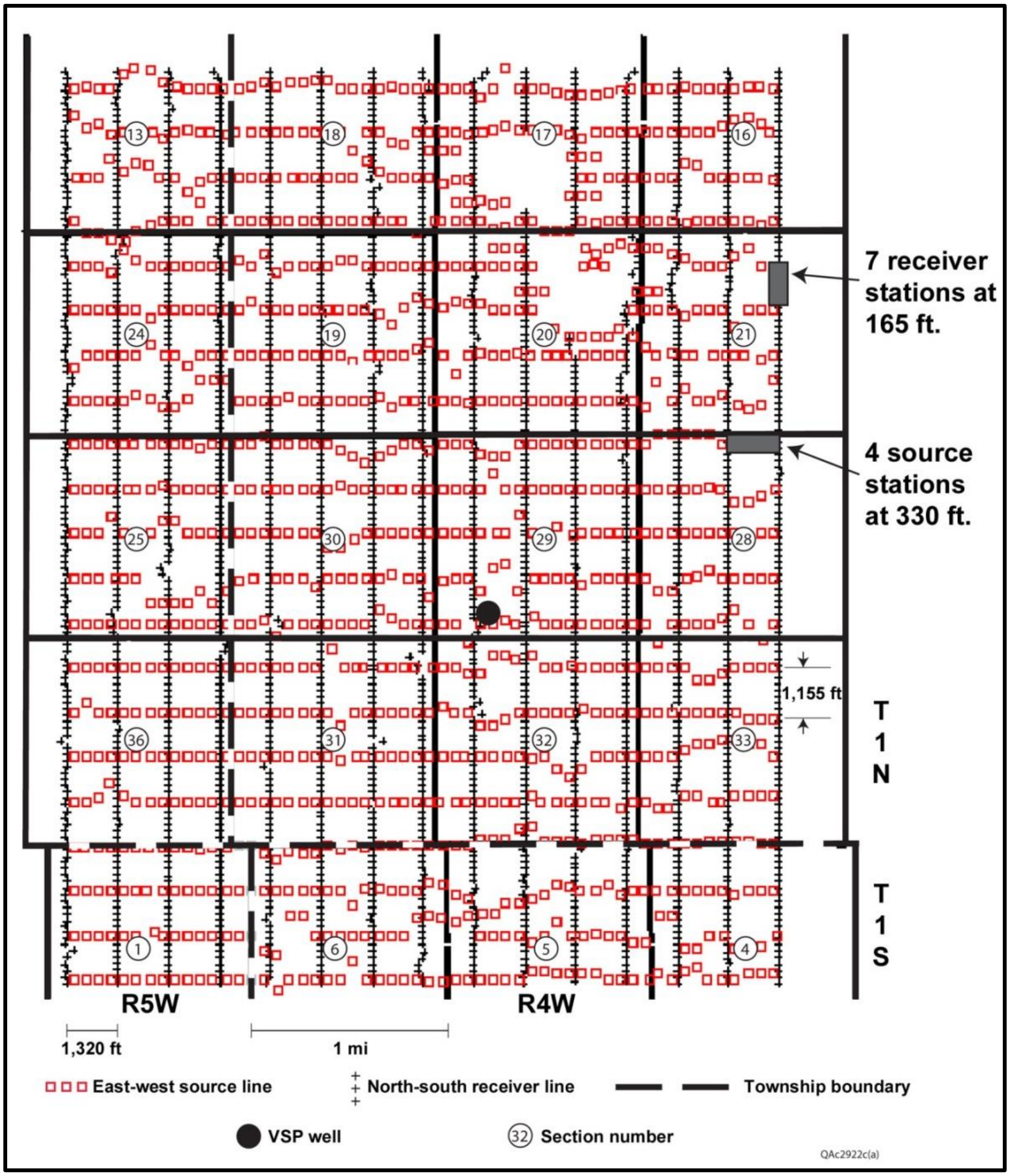

Figure 4. Seismic survey design in Stephens County, Oklahoma.

21 shot lines and 15 receiver lines were in place with line spacings of 1,155 ft and 1,320 ft, respectively. Full fold of 21 was achieved in 9.38 square miles of the total survey area of 15.84 square miles. Surface obstacles disturbed source-receiver placement in S17 and S20. This disturbance in the source-receiver grid affected the P-wave and SH-wave data quality in the areas having skipped stations.

Data Processing

Fully processed and migrated P-P, SH-SH, and SV-SV data volumes are used in post-stack multicomponent seismic analysis. My research will include migrated, post-stack data in only P and SH domains.

The processing steps for the P-wave data are the following: phase-shift migration, post-stack 1,000-ms time-variant scaling, post-stack time-variant filtering, spectral balancing 10 – 96 Hz, and *FXY* enhancement. The data have 32,368 traces over 15.84 square miles with 1,501 samples per trace over 3 seconds; the sampling interval is 2 ms.

The processing steps for the SH-wave data are the following: stack based on 82.5 ft X 165.0 ft bins, shear pre-gain and post-gain balance on all four data components, trace equalization 500 – 5,000 ms, and multiple band-pass filters (8 – 35 Hz over 0 – 2,000 ms; 8 – 25 Hz over 2,500 – 3,500 ms; and 8 – 18 Hz over 4,000 – 6,000 ms). The data have 32,368 traces over 15.84 square miles with 1,501 samples per trace over 6 seconds; the sampling interval is 4 ms.

Well Data

There are many wells within this seismic survey, none of which include any type of sonic logs or velocity data. The wells are clustered mainly in Sholem Alechem oilfield and Doyle East (Figure 7 and Figure 8). Twenty-one well log suites are available as images of electric surveys, obtained through the Oklahoma Geological Survey. Ten wells had some digital logs (gamma ray, density, and resistivity) as listed in Table 2. Few wells penetrate deep reservoirs; most wells target only shallow objectives.

Several velocity surveys were available at a distance of a few miles around the seismic survey. However, most of these surveys were too shallow to be extrapolated to the deep seismic data. The other surveys were of bad quality. In addition, a VSP test was attempted at the well site located in Figure 4, but the data acquisition was unsuccessful because the well casing was not properly cemented. All of these velocity data were excluded from this work.

Table 2. List of wells with digitized logs.

Well	Logs*	Depth (ft)	Well	Logs*	Depth (ft)
Wade 1	GR and ϕ_D	3,450 - 6,160	Ringer 1-32H	GR, ILD	1,300 - 8,670
	ILD	2,980 - 6,160			
Wade 2	GR and ϕ_D	3,500 - 6,260	Sea Prop 1	GR and ϕ_D	3,400 - 9,000
	ILD	2,830 - 6,260		ResD	970 - 9,000
Wade 4	GR, ϕ_D	3,400 - 6,420	Pollard 1	GR and ϕ_D	3,280 - 8,700
	ILD	2,800 - 6,420		ResD	800 - 8,750
Wade 3	GR, ϕ_D, and ILD	2,980 - 6,100	Gant 1-19	GR, AHT90, and ϕ_D	3,250 - 11,400
Mary Sands 1A	GR and ϕ_D	3,000 - 5,800	Vera 1-18	GR and ϕ_D	3,100 - 6,300
	ILD	600 - 5,820			

*GR: gamma ray; ϕ_D: density porosity; ILD, ResD, and AHT90: deep resistivity logs

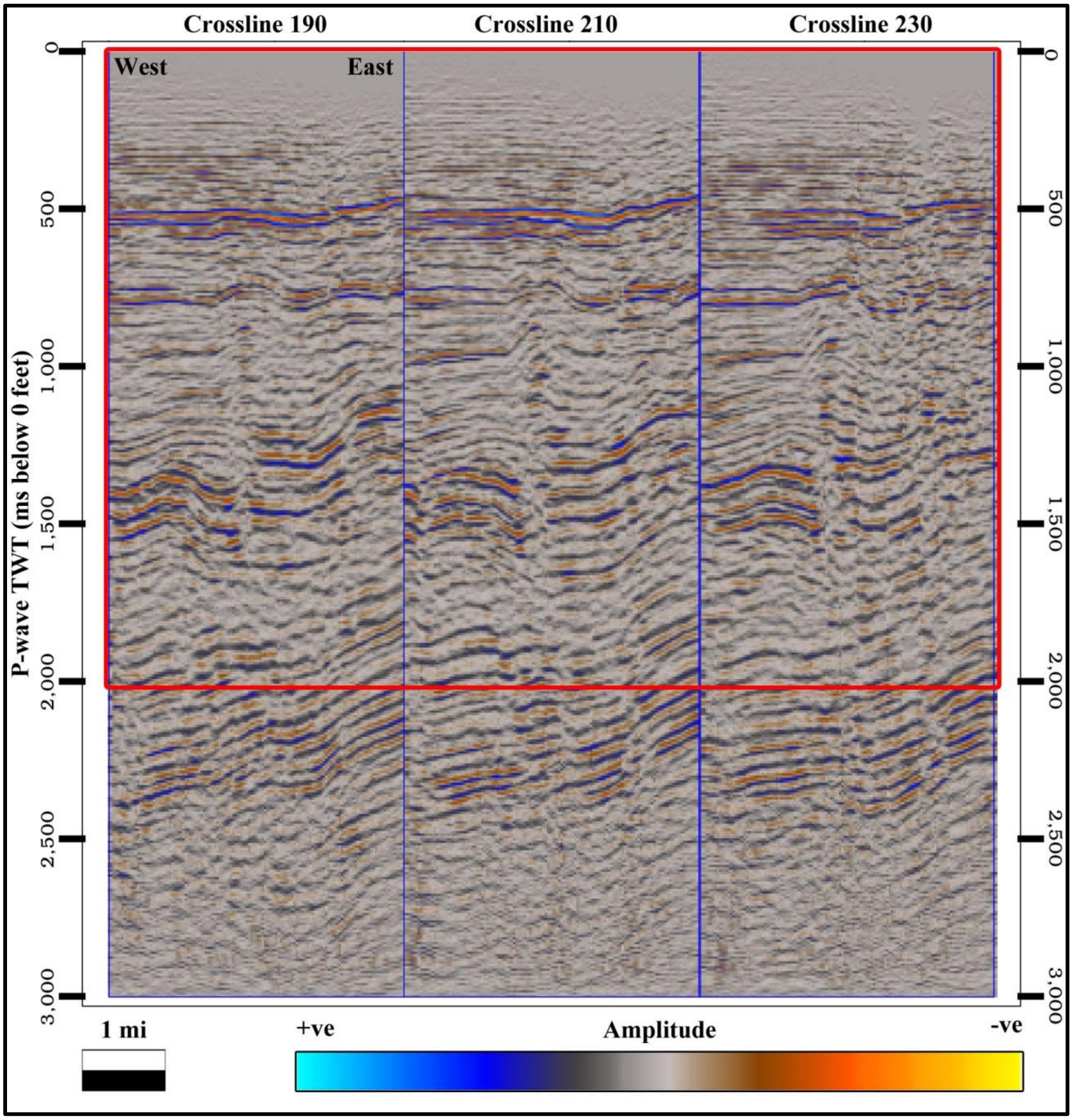

Figure 5. Available P-P seismic data.

This figure shows three parallel profiles that illustrate the 3 seconds of P-wave reflection data. The red outline defines the data that were analyzed. After careful analysis, the lower 1 second was deleted for two reasons. First, no well control penetrated that deep into the formations. Secondly, the low quality corresponding shear data (4 – 6 seconds in SH-wave domain) make it difficult to register the reflectors with those from the P-wave data. Figure 7 is the index map for the three seismic panels.

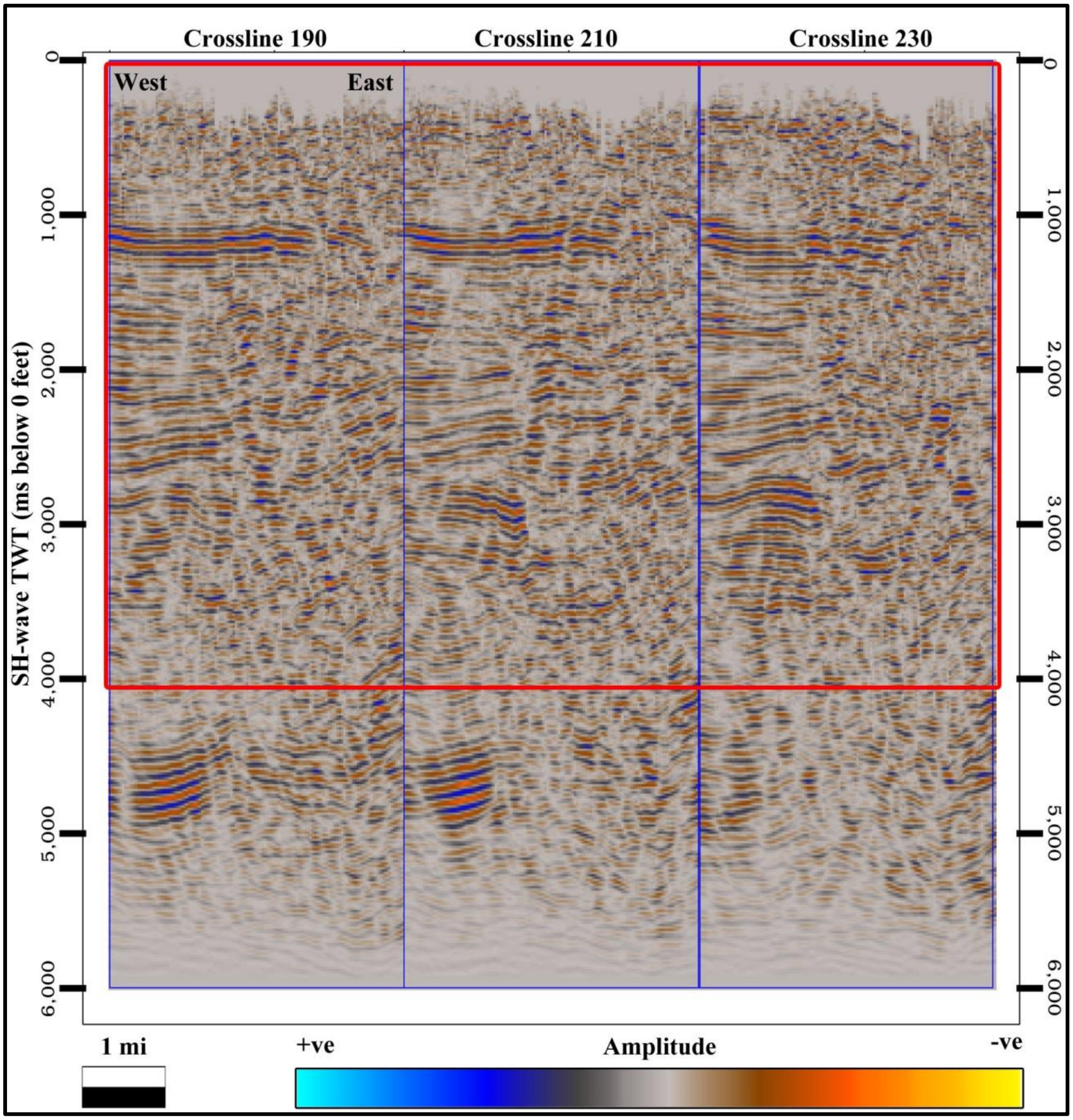

Figure 6. Available SH-SH seismic data.

This figure shows three parallel profiles that illustrate the 6 seconds of SH-wave reflection data. The red outline defines the data that were analyzed. After careful analysis, the lower 2 seconds were deleted for two reasons. First, no well control penetrated that deep into the formations. Secondly, the low quality corresponding compressional data (2 – 3 seconds in P-wave TWT) make it difficult to register the reflectors with those from the SH-wave data. Figure 7 shows the locations of the seismic panels.

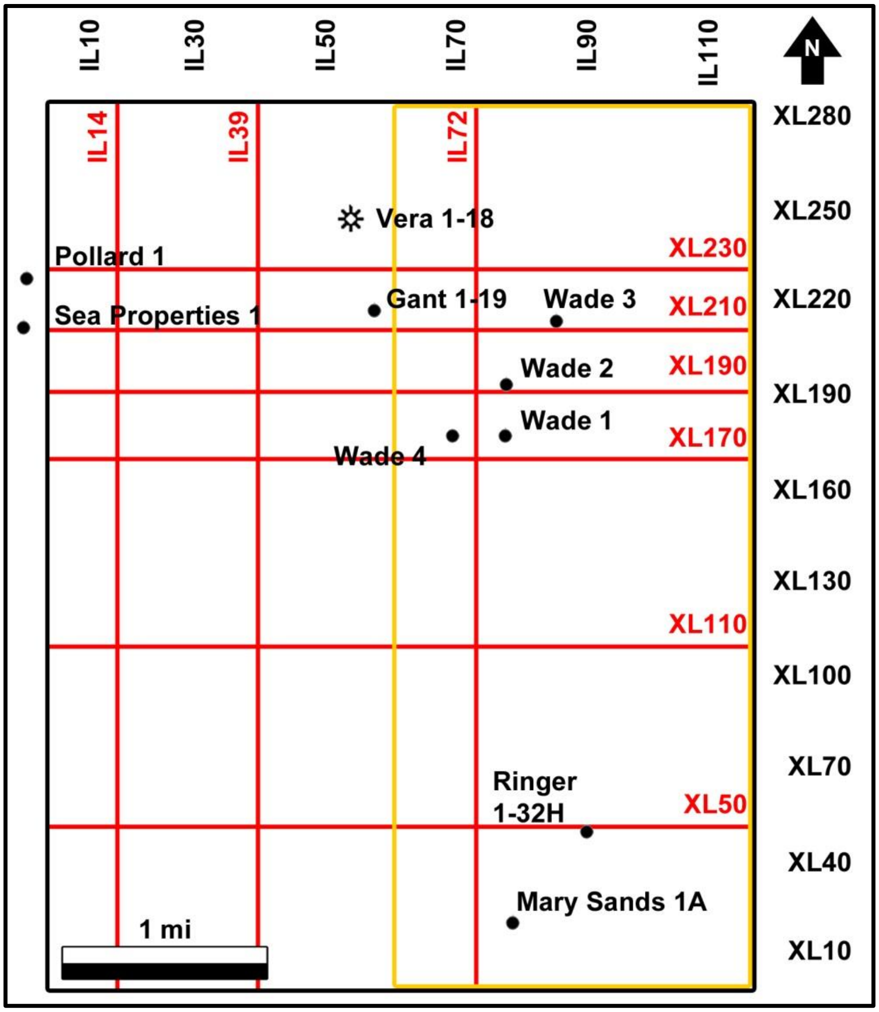

Figure 7. Well locations and index map.

Well Gant 1-19 penetrates deep formations. Wells Wade 1, Wade 2, Wade 3, Wade 4, and Vera 1-18 go through shallow reservoirs only. Those six wells were used for creating well-seismic ties (using density logs). Pollard 1 and Sea Properties 1 are outside the survey. Ringer 1-32H does not have density or sonic logs. Mary Sands 1A has a discontinuous log interval making it difficult to match the seismic data, and it was also excluded. The area highlighted by the orange rectangle covering the eastern portion of the survey has lower S/N for both P and SH data. Reflector continuity was greatly affected, especially in the SH-SH volume, which led to using manual picking.

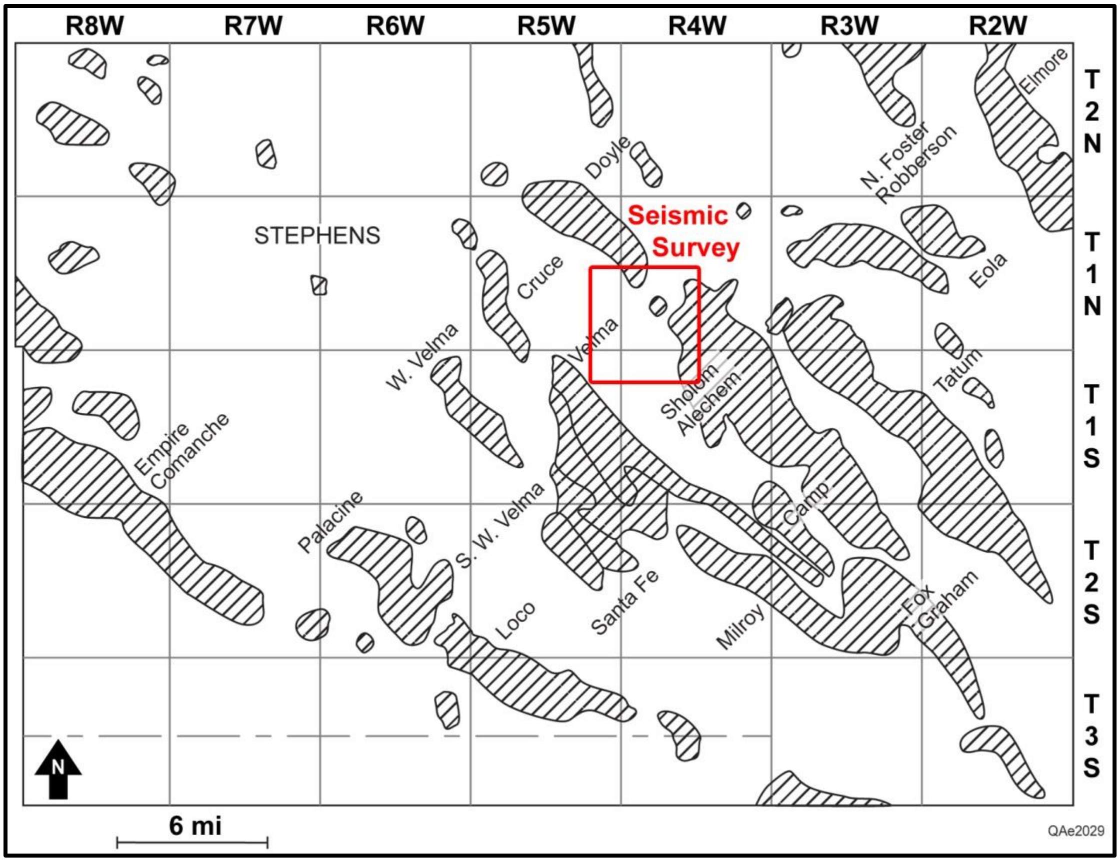

Figure 8. Location of Sho-Vel-Tum field and the 9C/3D seismic survey (modified from Hicks, 1956).
Sho-Vel-Tum field represents three oil and gas fields: Sholem Alechem, Velma, and Tatum in Stephens County, Oklahoma. They trend northwest-southeast and are combinations of structural and stratigraphic traps.

Chapter 2: Geological and Geophysical Review

This chapter discusses briefly the geology and stratigraphy of the Sho-Vel-Tum oil field and introduces some geophysical techniques described by others who approached similar problems.

GEOLOGY OF SOUTHERN OKLAHOMA

Geologic forces across Oklahoma have led to the subsidence of large areas to form sedimentary basins, whereas adjacent areas were folded and thrust upward forming uplifts. Most exposed rocks in Oklahoma are of sedimentary origin: shale, sandstone, limestone, and gypsum. Variable thickness sedimentary cover rests on a basement of igneous and metamorphic rocks that underlie all parts of the state. The Southern Oklahoma folded belt is structurally extreme and complex, including several major uplifts and basins. Paschal (1941) has published an extensive study regarding the major tectonic provinces of southern Oklahoma and their relation to oil and gas fields. Five tectonic provinces (Figure 9) form the Southern Oklahoma Belt: (1) the homogenous, continent-extending, Appalachain-Ouachita-Marathon mobile belt in addition to four heterogeneous mobile belts; two "uplifts" (2) Hunton-Tishomingo and (3) Amarillo-Wichita-Red River uplifts; and two "geosynclines" (4) Arkansas Valley and (5) Anadarko-Ardmore geosynclines. Evidence shows the latter geosyncline was formed by compression and squeezing. On the other hand, local structure of the uplifts is caused by "vertical uplifts", which results in prolific oil production, especially in rocks of Ordovician age, compared to conditions found in geosynclines. The term "geosyncline" is used in this context to refer to long, narrow structures that have "a great downward flexure on the earth's crust" as defined by Webster's dictionary. This study will focus on the Anadarko-Ardmore Basin because that is the location of the seismic survey data.

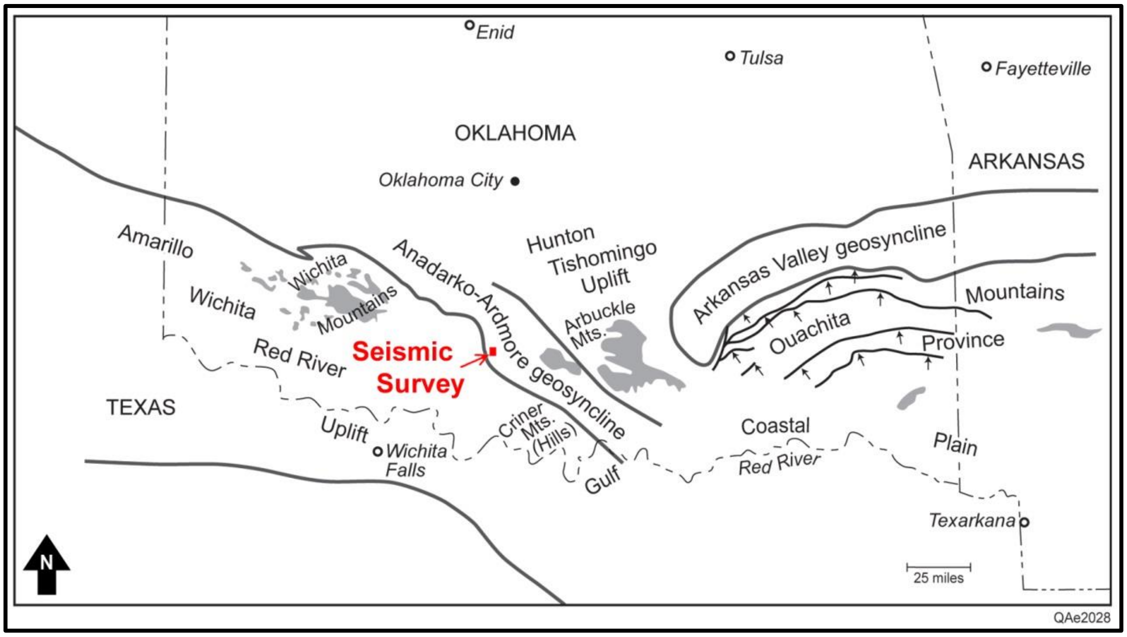

Figure 9. Major tectonic provinces in the Southern Oklahoma Belt (modified from Paschal, 1941).

Five tectonic provinces form the Southern Oklahoma Belt: (1) the homogenous, continent-extending, Appalachain-Ouachita-Marathon mobile belt in addition to four heterogeneous mobile belts; two "uplifts" (2) the Hunton-Tishomingo and (3) the Amarillo-Wichita-Red River uplifts; and two "geosynclines" (4) the Arkansas Valley and (5) the Anadarko-Ardmore geosynclines.

The southeast part of the Anadarko Basin and the southwest part of the Arkoma Basin are north of the Arbuckle Mountains, and are separated by the Pauls Valley uplift and the Hunton anticline. The Ardmore Basin, bounded by the buried Wichita Mountains and the Criner Hills anticline, is deep and narrow, and lies south of the Arbuckle Mountains (Figure 9 and Figure 10). The structure is complex to explore, but the sharp folding, faulting, and fracturing during the Late Mississippian-Early Pennsylvanian time created excellent structural traps for oil accumulation. This geosyncline is believed to have been formed by southerly lateral compression which folded sedimentary beds, especially those of Pennsylvanian and Mississippian age. Elongate anticlines and synclines were formed with axes roughly perpendicular to the exerted force.

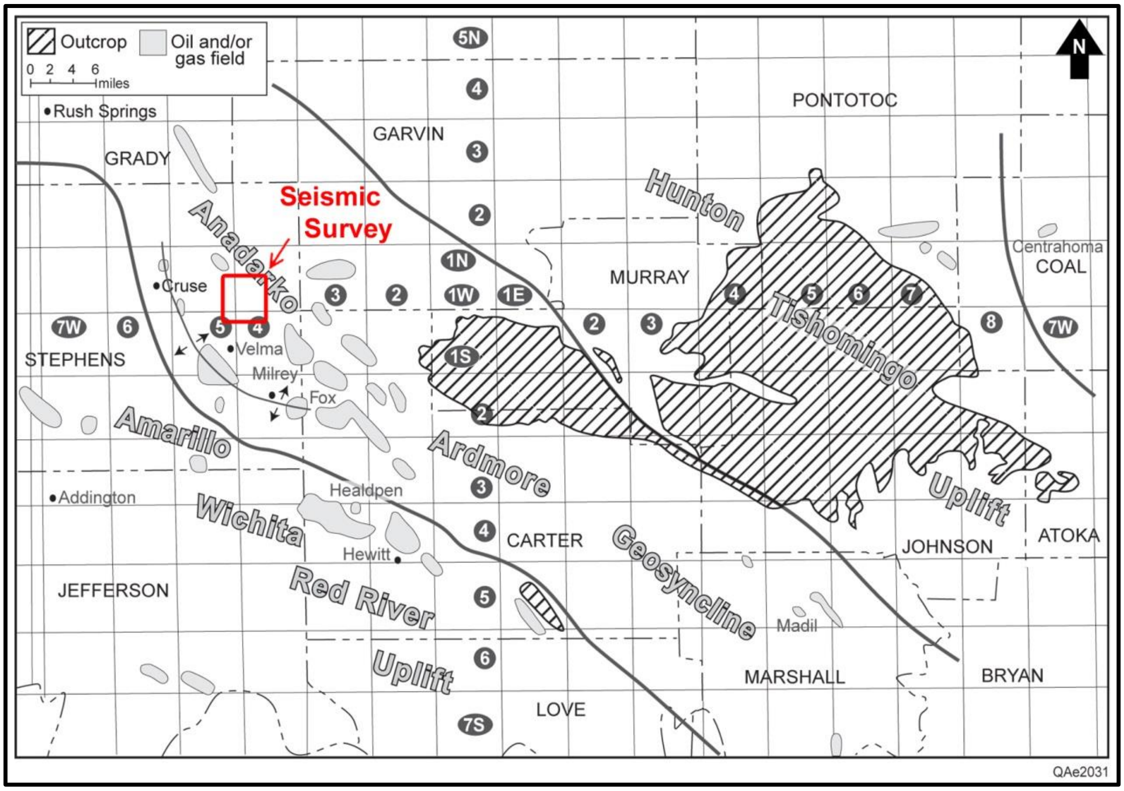

Figure 10. Boundaries of the tectonic provinces in the Arbuckle area (modified from Paschal, 1941).
A closer look at tectonic province boundaries indicates how the regional geologic structure might have formed. This would help in understanding fault orientation and intensity. The compressive regime that created the Anadarko-Ardmore Basin is assumed to have also caused major folding and reverse faulting.

Even though sandstone truncations and pinchouts are important, stratigraphic factors, structural anticlines and faults traps are more dominant. Early exploration focused on basin margins and uplifts to locate structural traps. These areas have been studied and analyzed extensively, limiting the chance of finding new reserves in the shallow parts of the area. The deeper geologic section is to some extent unexplored. Due to their structural complexity, deep rocks create major exploration and drilling challenges. For example, close-spaced wells penetrate different parts of the stratigraphic column because of the steep beds, faults, and unconformities that are penetrated. A good understanding of the structural and stratigraphic complexity in the deeper sections of the basins (below 6 km) will be crucial to justify further exploration. Most of the geological studies were done in the 1950s and 1960s. Seismic techniques used to this point have been inadequate to clearly define structures in these deep complex areas (Hicks 1956; Kleen 1994; Paschal 1941; Rutledge 1956).

STRATIGRAPHY OF SHO-VEL-TUM

The name Sho-Vel-Tum came from three oilfield names: Sholem Alechem, Velma, and Tatum. Due to the complexity and compartmentalization of the oilfields, the part of the field covered by my seismic survey and its vicinity does not belong to one specific field. In addition to the Sho-Vel-Tum oilfield, the seismic survey covers the southeastern part of Doyle oilfield.

Formerly known as the County Line field, the Sholem Alechem field is located close to the Anadarko-Ardmore geosyncline axis. Billingsley (1956) performed an extensive structural and stratigraphic study of this field. The stratigraphic analysis in this report is based on his findings. Sholem Alechem field is located in the northeastern part of Stephens County and the western part of Carter County. The field is about 9 mi long and 3 mi wide, trending northeast-southwest. Sholem Alechem field is a sharp anticlinal fold with 1,500 ft of closure and was formed as a result of the post-Springer Wichita orogeny and the post-Hoxbar Arbuckle orogeny.

The variability in stratigraphy of Sholem Alechem field makes it difficult to correlate its beds with nearby fields. The geologic column in southern Oklahoma ranges from Pre-Cambrian to Permian (Figure 11). Whatever the field size, reservoirs are distributed stratigraphically as well as geographically in Oklahoma. Oil is found in reservoirs with age of Cambrian to Permian, though most of the giant reservoirs are in the Pennsylvanian strata (Boyd, 2005). Detailed stratigraphic analysis and nomenclature have to be confined to local areas because only a few horizons are recognizable regionally. Oil production from this field is mainly from the sandstones of Pennsylvanian age within Hoxbar, Deese, and Springer groups. The Upper and Lower Fusulinid sand zones, within the Deese group, are among the first producing zones located in the Carter County part of Sholem Alechem. These zones are composed of fine-grained, white, porous, thin sandstone beds. After further development, these beds became of minor significance and deeper formations were targeted in later drilling projects. The Tussy sandstone zone lies below the Fusulinid, with 200-300 ft of gray shale in between. These fine-grained, calcareous, porous sandstones are oil-productive for the most part. This bed correlates approximately with the Tussy field in Carter County. The last producing zone within the Deese group is the Pickens sandstone zone. The Pickens sand is an oil-bearing fine-grained calcareous porous sandstone. The Springer sands are the main producing intervals and have been extensively targeted in recent field development. The Markham sandstone zone is an oil-producing fine-grained porous sandstone in the Springer group. The Markham structural trap was formed in a truncated up-dip edge of the sandstone at the post-Springer unconformity. The Aldridge sandstone zone is 200 ft stratigraphically below the Markham zone and is an oil- producing zone similar to the Markham zone in every aspect, even in its structural termination against the post-Springer unconformity.

The Aldridge and Markham zones both are brine-bearing in the southeast part of Sholem Alechem, but oil-bearing in the northwestern flank of the structure. The Humphreys sandstone zone is porous, white, and fine-grained. It is an oil-bearing zone but lies in the southeast portion Sholem Alechem field, which is outside our area of interest. The First Sims sandstone and Second Sims sandstone zones are fine- to medium-grained porous sandstones. They have structural closure of about 1,500 ft and have accounted for most of the oil production in the Sholem Alechem field. The Springer group is composed of the Markham zone through the Second Sims zone within the Sholem Alechem field (Billingsley, 1949).

The Sycamore formation, which lies directly on the Woodford shale over a great portion of the Anadarko basin, is located in the Meramecian series (Braun, 1961; Bennison, 1956; Branson, 1956). The Sycamore limestone is about 70 to 300 feet of slate blue, silty to fine sandy limestone with calcareous shale beds of variable thicknesses (Braun, 1961). Figure 12 shows a type log for Sho-Vel-Tum oil field based on four wells. Specifically, the compiled type log shows the gamma ray and bulk density logs of four intervals corresponding to Pollard 1, Wade 1, Sea Properties 1, and Gant 1-19. I matched the geologic times for each formation to the well data using available formation tops.

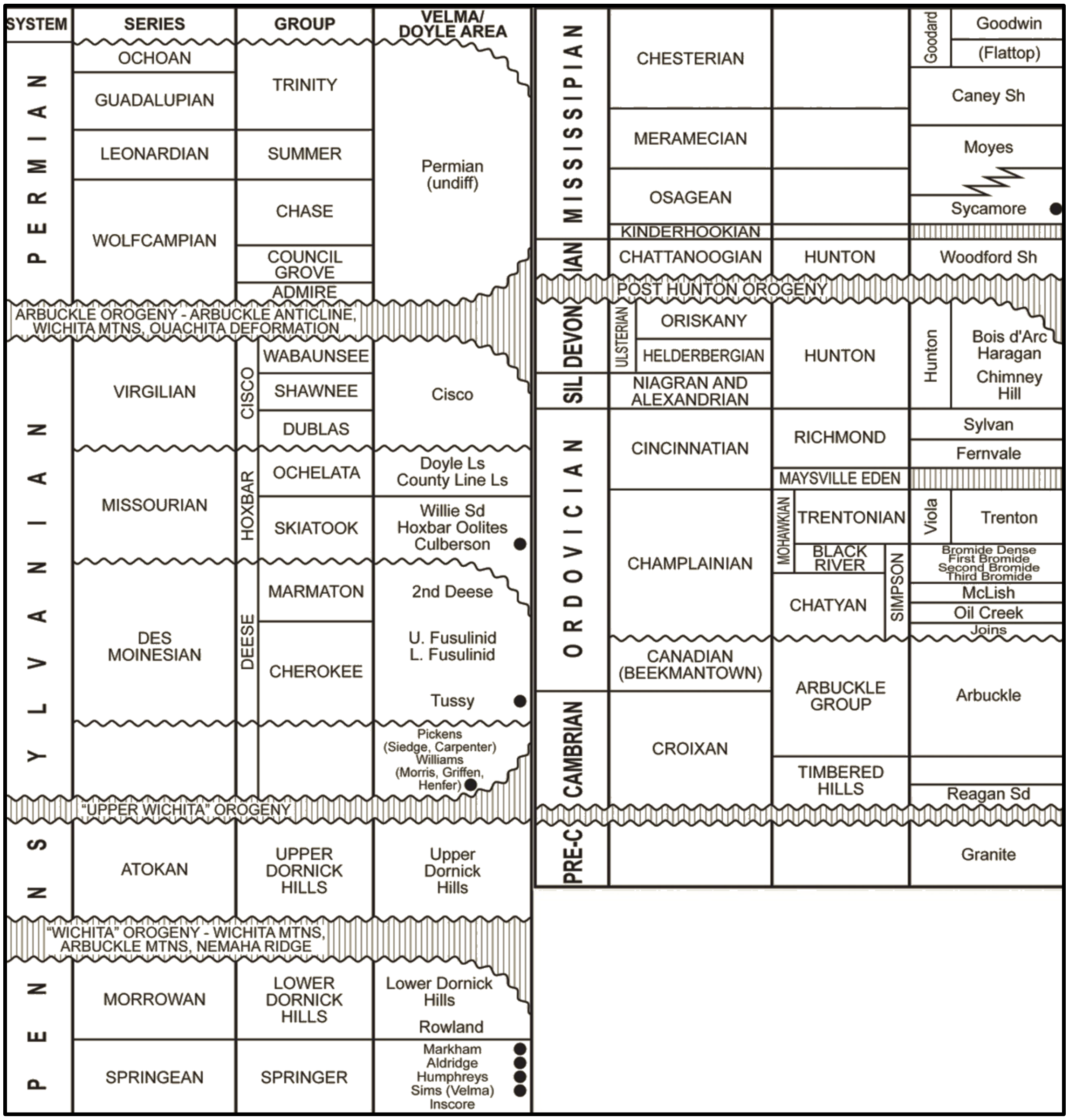

Figure 11. Stratigraphic column of Sho-Vel-Tum area (after Cipriani, 1963).
Wichita and Arbuckle orogenies caused the complex structure of Sho-Vel-Tum formations. The primary target of the 9C/3D seismic data is the Sycamore limestone. Black dots mark the oil and gas producing formations within the Sho-Vel-Tum field.

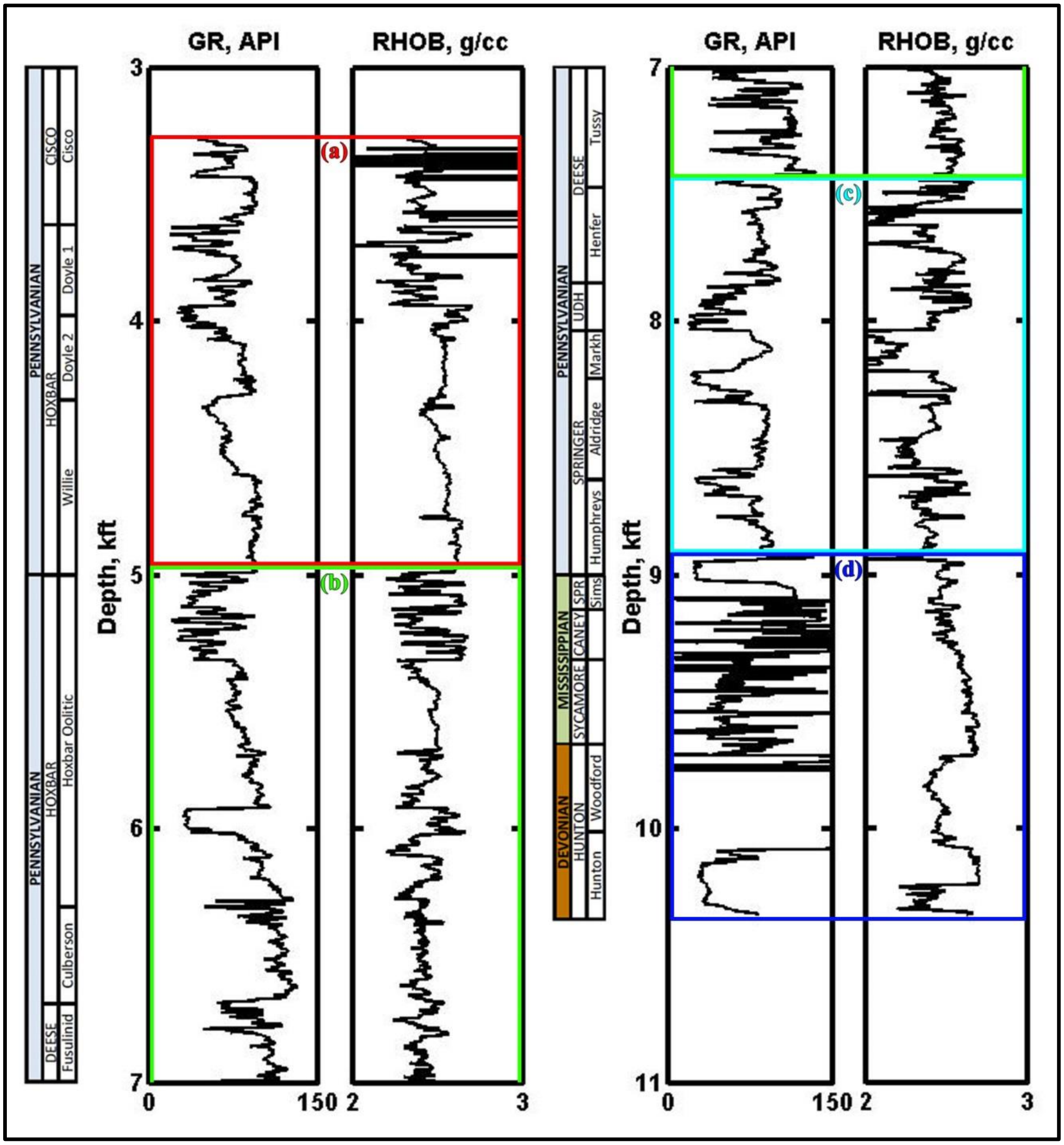

Figure 12. Type well log for Sho-Vel-Tum oil field.

The gamma-ray and density logs are compiled from four wells: (a) Pollard 1 (3,280 – 4,988 ft), (b) Wade 1 (4,988 – 7,427 ft), (c) Sea Properties 1 (7,427 – 8,941 ft), and (d) Gant 1-19 (8,941 – 10,339 ft). Formation depths do not represent true depths. Log depths are cumulative to create a comprehensive stratigraphic column.

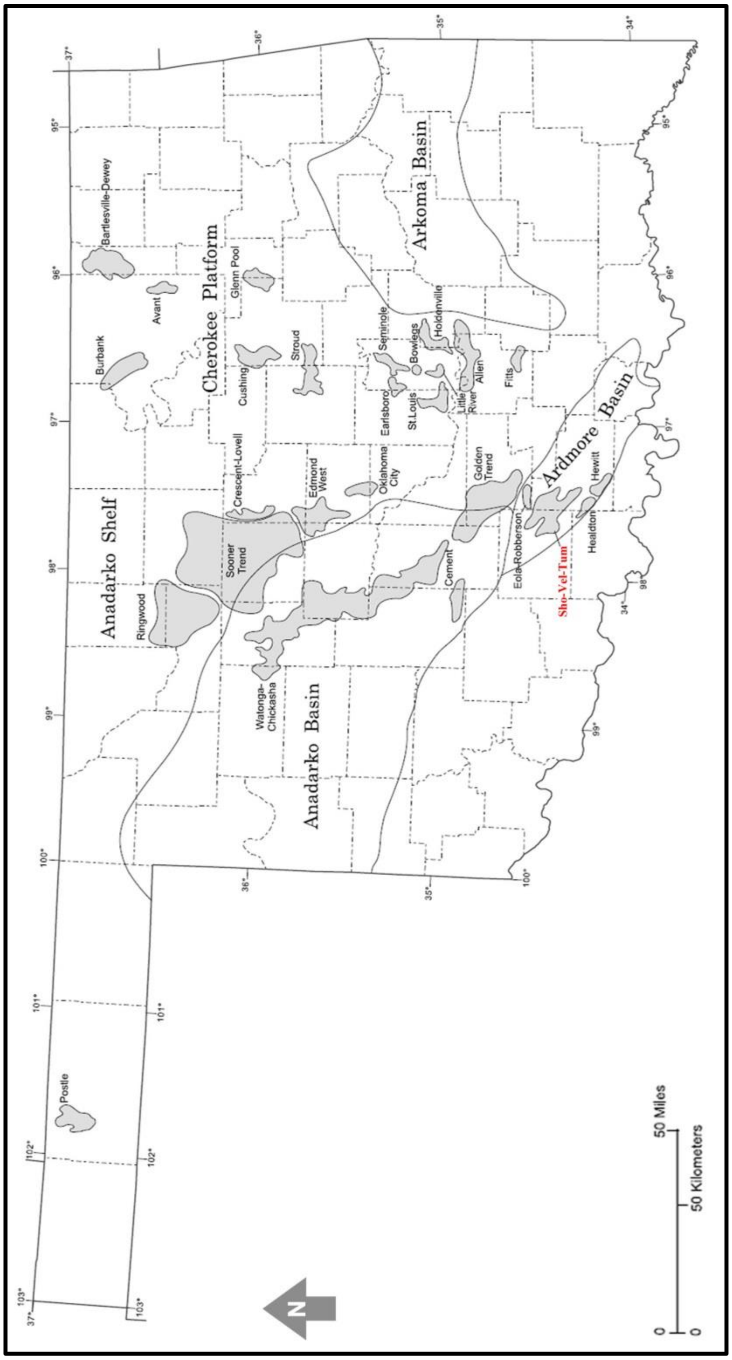

Figure 13. Petroleum provinces and major oil fields, recovery > 100 million barrels (after Boyd, 2005).

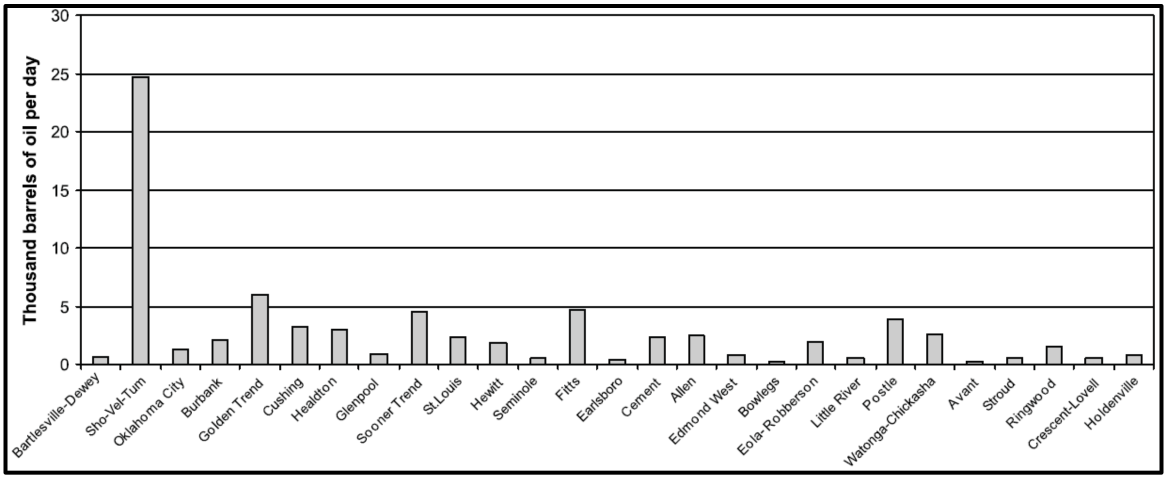

Figure 14. Daily oil production from Oklahoma fields with recovery > 100 million barrels (IHS Energy, 2004).

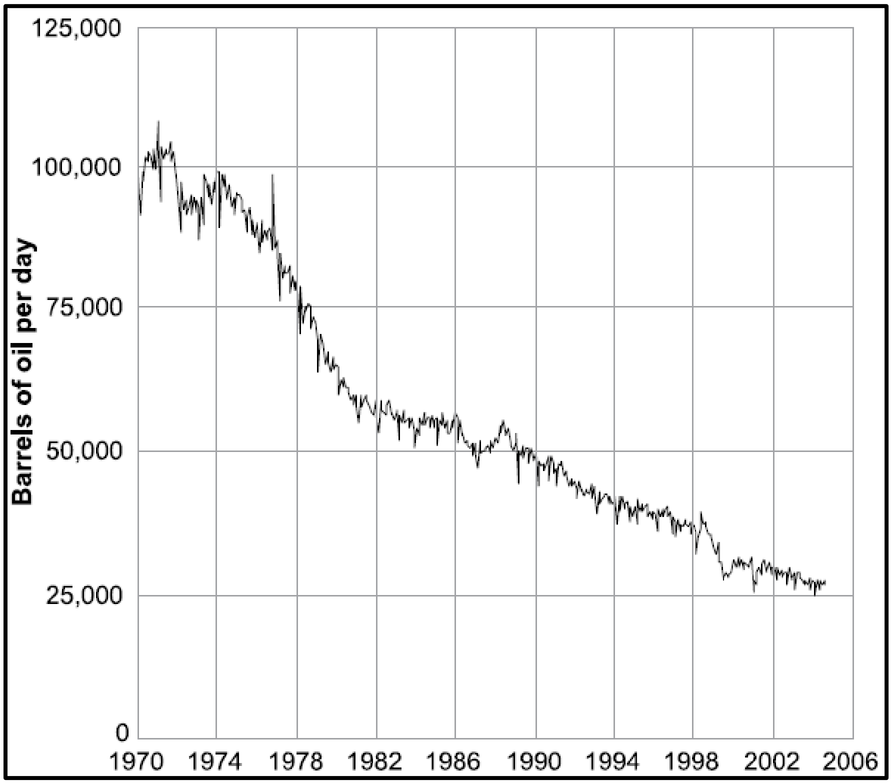

Figure 15. History of oil production in Sho-Vel-Tum (IHS Energy, 2004).

Most of Oklahoma’s oil comes from its major oil fields shown in Figure 13. Sho-Vel-Tum is the largest producing field in Oklahoma and has the most number of active wells as shown in Figure 14, with a daily oil production rate of 25,000 barrel of oil per day as of 2004 (Boyd, 2005). Extensive production from Sho-Vel-Tum has led to a noticeable daily production rates as shown in Figure 15. This decline in production rates, besides the complex structural nature of the field, had lead researchers to examine available data in more depth. The 3D seismic survey used in this work is an example of available data that can be used to map and characterize by-pass hydrocarbon accumulations.

DEPTH-REGISTRATION TECHNIQUES

Several researchers have published techniques and methods to increase the confidence in event-registration in areas with limited data. A number of these methods have been published by Bureau of Economic Geology, University of Texas at Austin. Authors would use interpretive, computational, or a combination of those methods to identify depth-equivalent events depending on data availability.

Structural “Tie Points”

DeAngelo et al. (2003) and Murray et al. (2003) suggested scanning the time slices of P-wave and S-wave discontinuity volumes looking for lithological indicators to locate “nail” points. These points represent, with good confidence, the same event on the P-wave and converted-wave seismic data. Their example dataset was a 4C/3D ocean-bottom cable (OBC) seismic data in shallow water, offshore Louisiana. Their converted P-SV seismic data, as compared to our 9C/3D seismic survey, was of high quality. Shear-wave seismic data processing is simpler offshore than onshore. The low-velocity near-

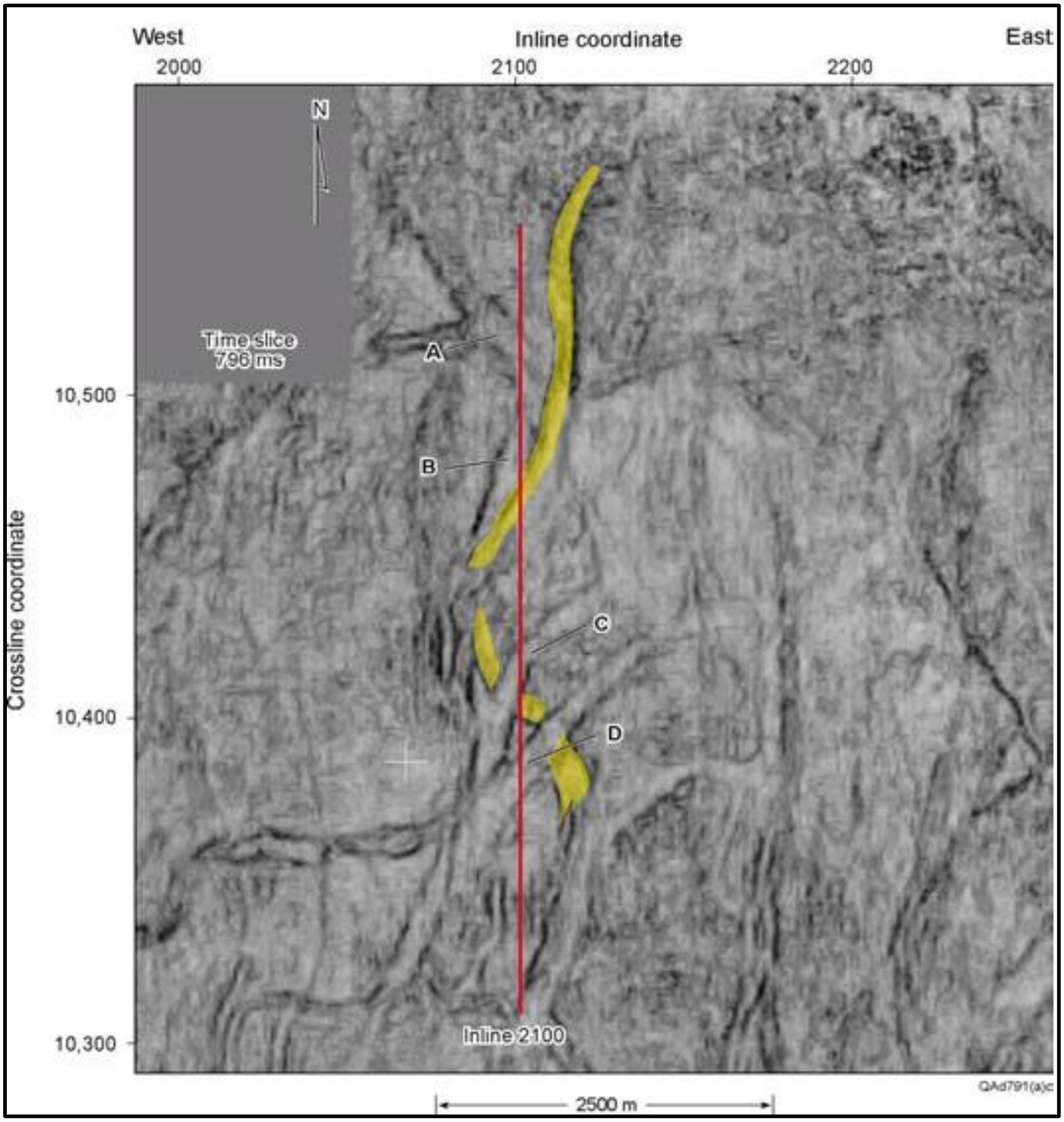

Figure 16. Time slice at 796 ms of P-P coherency volume of 4C/3D OBC seismic data offshore Louisiana (after DeAngelo et al., 2003).

Stratigraphic features such as meandering channels can be used as well as structural features as starting points for depth-registration of compressional and shear wave data. For example, the shaded channel is also imaged by P-SV data (Figure 17).

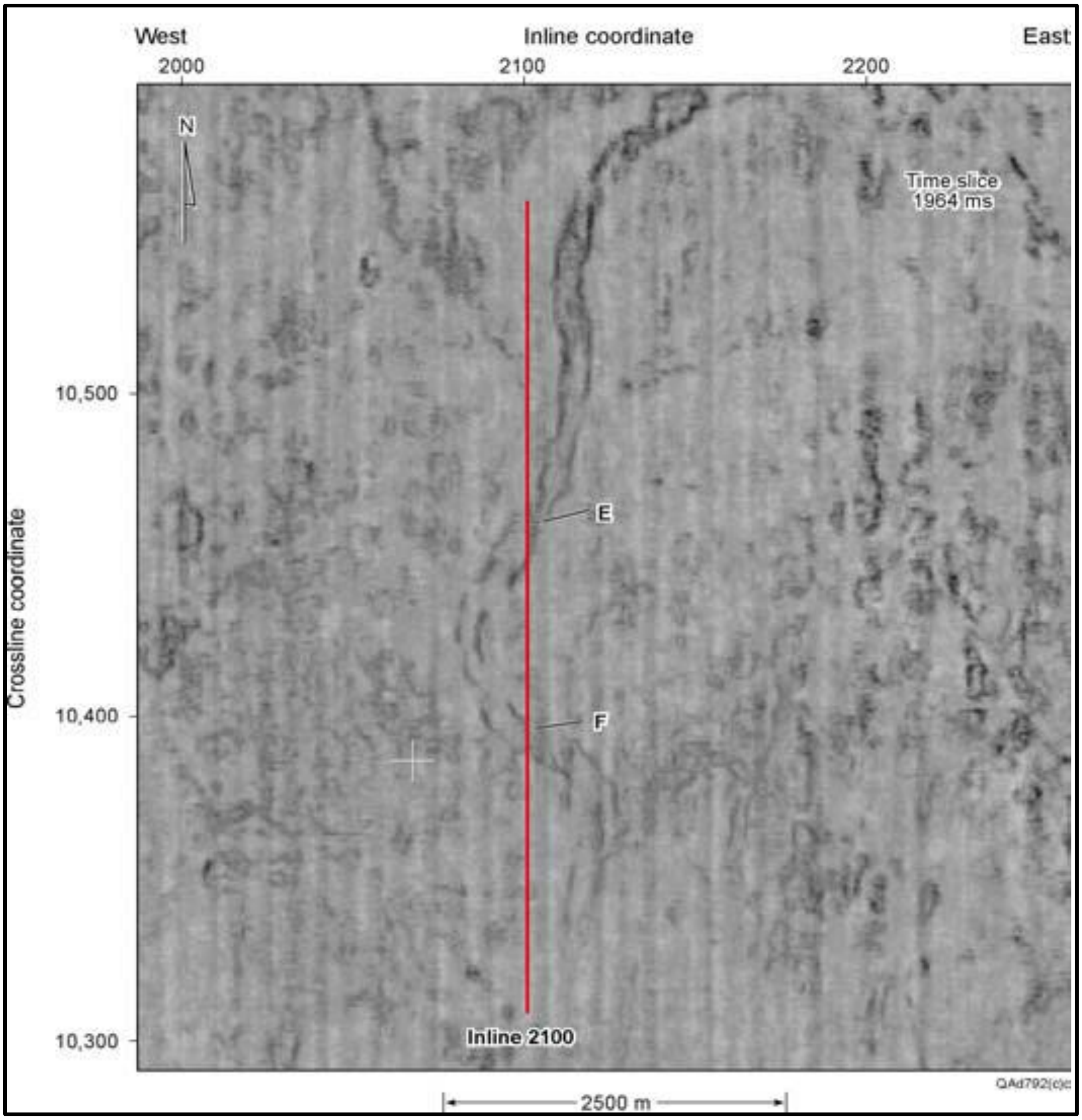

Figure 17. Time slice at 1,964 ms of P-S coherency volume of 4C/3D OBC seismic data offshore Louisiana (after DeAngelo et al., 2003).
Stratigraphic features such as meandering channels can be used as well as structural features as starting points for depth-registration of compressional and shear wave data.

surface layer found onshore creates data processing challenges, particularly issues involving source-receiver statics. Survey parameters, like source-spacing and receiver-spacing, are usually optimized for acquiring P-wave data. Even so, offshore shear data processing tends to yield high quality converted-SV seismic volumes. However, because of the absence of sonic logs and velocity information in shallow near-seafloor sediments, DeAngelo et al. (2003) concluded a simultaneous interpretation of both P-P and P-SV volumes was necessary to create preliminary depth-registered events. Seismic attribute maps, like V_p/V_s and Poisson's ratios, were useful for double checking the horizon picks.

Figures 16 and 17 show the effectiveness of this technique. These figures are presented by DeAngelo et al. (2003) to highlight a stratigraphic feature that was imaged by their seismic survey by both P-P and P-SV data. The figures are time slices across P-P and P-SV discontinuity volumes marking the edges of a channelized feature. Hardage et al. (2011a) explained that if thin-bed stratigraphy is imaged by P and S data, then adjusting the P and S images to equivalent thin-bed features results in depth-registration with accuracy sufficient enough for many applications. The coherency cube is a volume of discontinuity coefficients generated from input 3D seismic data that detect faults and stratigraphic anomalies on time or horizon slices (Chopra, 2002). With the lack of velocity data, these stratigraphic ties are a starting point for a depth-registration workflow.

The t_s/t_p Technique

Pardus et al. (1990) reported a technique for characterizing dolomitic reservoirs based on t_s/t_p values of different stratigraphic intervals. The parameter t_s refers the TWT of horizons on the SH-SH data, and t_p refers to the TWT of horizons on the P-P data.

They applied their t_s/t_p analysis to the Scipio Field in Michigan to discriminate dolomite reservoirs in a massive limestone matrix. A seismic line, P-wave and SH-wave data, traversed the Scipio Field and served as calibration for their proposed t_s/t_p technique. They mapped reflections on the P-wave and SH-wave data using visual correlation of reflection behavior and structural similarity. Then correlations were refined after calculating t_s/t_p values. Laboratory data show that V_p/V_s have an average value for limestone of approximately 1.90 and for dolomite the ratio is near 1.80 as in Table 3 (Domenico, 1984; Pardus et al., 1990). Their interpretations showed a good match between interval V_p/V_s and dolomite percentage calculated from well logs. The t_s/t_p curves were stable even for narrow time intervals, which validates their picks on the P-wave and SH-wave data.

Table 3. Range of V_p/V_s in typical consolidated sedimentary rocks (after Domenico, 1984)

Rocks	V_p/V_s
Sandstone	1.59 – 1.76
Calcareous sandstone	1.67 – 1.76
Dolomite	1.78 – 1.84
Limestone	1.84 – 1.99
Shale	1.70 – 3.00

Analysis of redundant intervals can identify bad picks (mis-picks). The analysis explained that if a miscorrelation was picked on P-wave or SH-wave data and lead to a t_s/t_p anomaly, a similar opposite sign anomaly should appear on the interval immediately above or below the mis-picks. Their proposed t_s/t_p technique will be used to refine the P-wave and SH-wave horizon correlations in this work. Figure 18 shows t_s/t_p profiles of five stratigraphic intervals over the Scipio field (Pardus et al., 1990). The t_s/t_p (equivalent

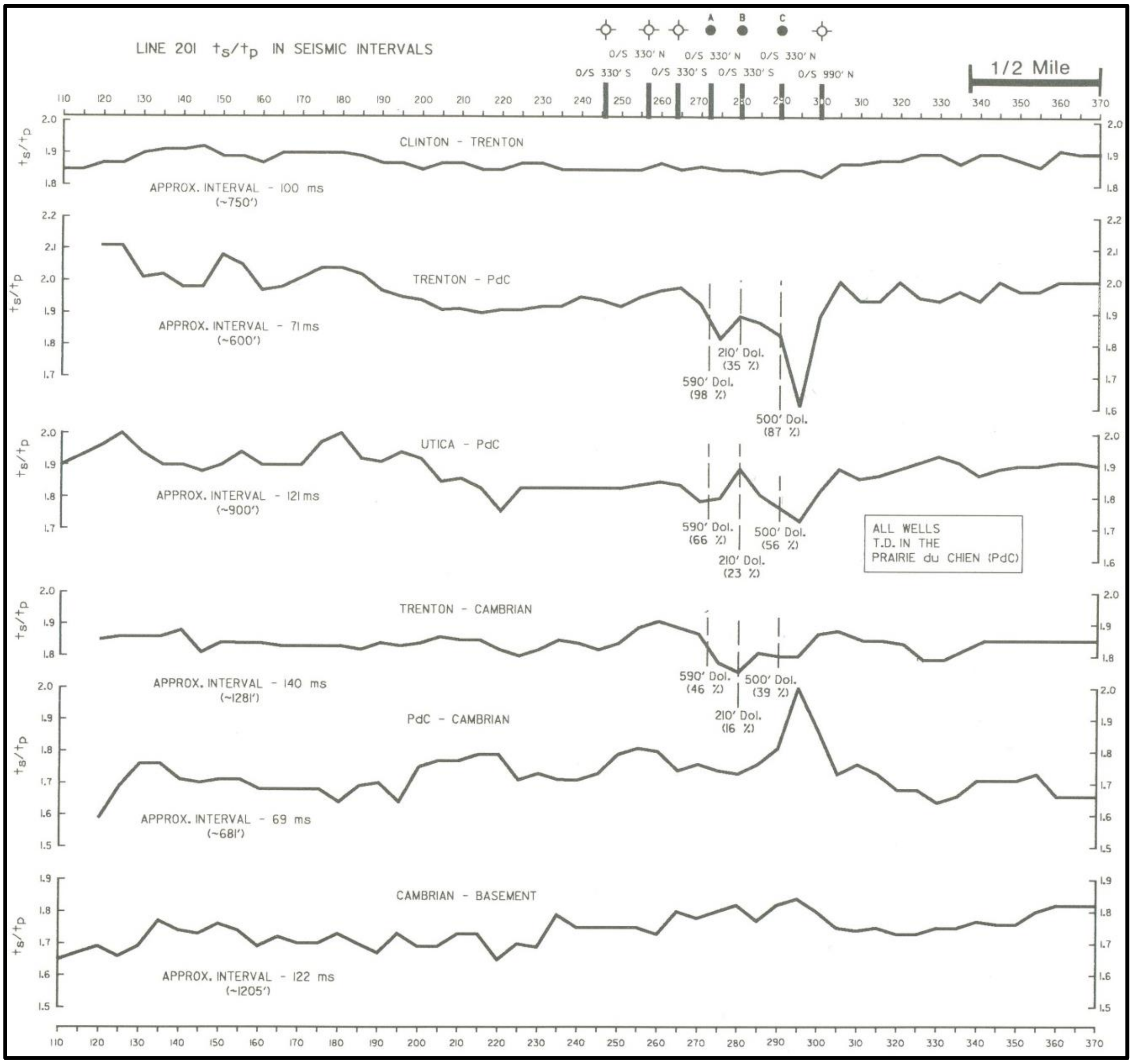

Figure 18. Profiles of t_s/t_p for five stratigraphic intervals on line 201 over the Scipio field (after Pardus et al., 1990).

A decline of about 0.4 in t_s/t_p noticed at crossline 295 on Trenton-PdC interval is “mirrored” on PdC-Cambrian interval, which suggests this variation could be a mis-pick in the PdC horizon. The dolomite response from well data and t_s/t_p was matched successfully at wells A, B, and C. Mis-picks can be distinguished from actual stratigraphic variations by examining consecutive intervals of interest and the remaining redundant intervals.

to the interval V_p/V_s) is sensitive to P-P and P-SV horizon picks. For example, let us examine the PdC depth-registered horizon (Figure 18). At line 201-crossline 295, there is approximately a 0.3 change in t_s/t_p when examining the t_s/t_p curve for the interval Trenton-PdC. If we consider only this curve, we cannot say whether this is a mis-pick on Trenton, or on PdC, or an actual stratigraphic signature. So, we need to examine adjacent intervals, PdC-Cambrian. A "mirrored" mis-pick can be seen at the same location. Similarly, the UTICA-PdC interval shows the mis-pick on PdC horizon. Moreover, other redundant intervals – those who do not have PdC included in this analysis – do not show mis-picks at that location. This analysis strongly suggests the t_s/t_p-spike analyzed is due to a mis-pick rather than a stratigraphic variation. Also, a mis-pick appears more extreme on a thick interval as compared to a thinner interval. This effect can be noticed at the PdC mis-pick through the UTICA-PdC 121 ms, as compared to its mirror mis-pick on the 69 ms interval of PdC-Cambrian.

Other Methods

There are many qualitative and quantitative approaches published for registering depth-equivalent events. Depth-registration effectiveness depends on multicomponent seismic data quality and velocity data availability.

Fomel and Backus (2003) proposed an automatic registration warping algorithm to map compressional and converted-shear migrated images. They applied the method to a 4C/3D OCS data offshore Louisiana and achieved good results. They proposed two main products of their technique, which are improving the multicomponent seismic image registration and directly extracting interval velocity ratios from the warping function with good resolution.

Fomel et al. (2005) then proposed a multistep approach to multicomponent seismic image registration and applied it to a West Texas carbonate reservoir study. Their methodology involves initial interpretation, amplitude and frequency balancing, registration scan, and least-square optimization.

Van Dok and Kristiansen (2003) discussed how they can include depth-registration in a processing sequence to improve imaging as well as the quality of V_p/V_s function. They applied their methodology to a 4C seismic survey in the North Sea and achieved good results.

Murray et al. (2003) suggested a simple warping algorithm for event-registration. They applied their technique on the 4C/3D OBC seismic survey offshore Louisiana acquired in 1999. They suggest applying a data warping function to multiple 2-D sections selected from the 3-D volume to create converted-wave sections which are time-equivalent to the P-P sections. The function applied in their study is one-dimensional that compresses the P-S data without any lateral movement, which means they assume the migration algorithms account for lateral velocity variations.

Nickel and Sonneland (2004) presented a new method of seismic event registration that generates P-S volumes stretched to P-P time which allows multi-attribute inversion. Another outcome of their work is a high-resolution V_p/V_s volume which can be used as a new seismic attribute for reservoir characterization. This method was applied successfully to synthetic data as well as real data from the North Sea.

Chapter 3: Methods

This chapter highlights the methods used for the depth-registration workflow. First, it discusses the seismic survey design parameters. Then, it analyzes the geophysical techniques used including: well synthetic seismograms, effective displays, depth-registration using structural tie-points, depth-registration validation with t_s/t_p technique, and seismic attribute analysis.

SEISMIC SURVEY ANALYSIS

The Black Bear project was designed to image the Sycamore formation. The survey had 2,160 receiver stations spaced 165 ft apart within receiver lines, divided over 15 north-south receiver lines spaced 1,320 ft apart, with an average of 144 receivers per line. There were 1,176 source stations spaced 330 ft apart in the source lines, divided over 21 east-west shot-lines spaced 1,155 ft apart. The full-fold (21) area imaged was 9.38 square miles within the total 15.84 square miles covered by the survey. The recording swath consisted of three receiver-line intervals (a total of 3,886 ft in the crossline direction) and seven shot-line intervals (a total of 8,027 ft in the inline direction), with a maximum offset of 8,865 ft (Figure 4 and Table 4).

3D seismic surveys are designed to image shallow reflectors, a deeper prospect or a target interval, and other geologic features. Thus, information about the geology of the prospect is essential for optimizing onshore 3D seismic survey design (Hardage, 1997).

The depth of a primary target interval is a major input in creating source-receiver geometry. A common practice is to make the maximum source-receiver spacing of the recording swath, the area of active receivers in the recording grid, equal to the target depth. Hardage (1997) explains this method in his *Principles of Onshore 3D Design*.

Table 4. List of seismic survey design parameters.

	Aperture Design (March 9th, 1998)	Conducted Survey (June 16th, 1998)
Receiver lines	15	15
Total receivers	2,220	2,160
Average receivers per line	148	144
Live receivers	2,220	2,160
Receiver spacing, ft	165	165
Receiver-line spacing, ft	1,320	1,320
Receivers per square mile	-	136
Shot lines	21	21
Total shots/fired	1,197/1,197	1,176/1,176
Shots per square mile	-	74
Shot spacing, ft	330	330
Shot-line spacing, ft	1,155	1,155
Minimum/maximum channels	0/672	200/588
Areal extent, square mile	16.42	15.84
Total traces	602,280	528,528
Traces per square mile	-	33,376
Traces per CDP mile	-	1,043
Total bins	33,630	32,431
Populated bins	-	31,808
Bin width, ft	165	82.5
Bin height, ft	82.5	165
Inline bins	114	287
Crossline bins	295	113
Maximum fold	24	21
Nominal Fold	-	21
Full-fold (21) area, square mile	-	9.38
Maximum offset, ft	9,912	8,865
Minimum offset, ft	-	184
Maximum inline offset, ft	-	8,027
Maximum crossline offset, ft	-	3,886

The optimal configuration would be to have active receivers in all directions from the active source station extending to at least a distance equivalent to the target depth. Moreover, Hardage (1997) suggests that a square geometry of active receiver stations, with sides of twice the target interval, having the active source station in the center is a good approximation for recording wide-aperture swath design. However, due to the limited number of active recording channels available, a rectangular recording swath can be designed having one side with a distance equivalent to twice the target interval, and the other side spanning what the remaining active channels allow.

The desired shallow-reflector depth is another input for 3D seismic survey design. It does not have to be a reservoir. It is mapped as an interface that is used to aid data processing decisions regarding optimal stacking velocities and static estimations and to serve as a depth-registration point in data interpretation. If the dip of this shallow interface is known, it can help determine statics corrections and assist in velocity analysis. In practice, source-line and receiver-line spacing are approximately equal, or less than, the shallowest-target depth. However, a good choice would set those spacing parameters to half the depth of the shallowest target.

The 9C/3D seismic survey recorded 3 seconds of P-wave data, and 6 seconds of S-wave data. To estimate the depth where we can assume there will be a reliable image, we have to review the survey geometry and recording swath. Figure 4 shows the Black Bear project final geometry. There were 588 3-component active channels in the recording swath. The maximum inline offset was 8,027 ft (approximately 7 source-line intervals), whereas the maximum crossline offset was 3,886 ft (approximately 3 receiver-line intervals). The maximum offset was 8,865 ft. The maximum offset, the diagonal distance, indicates the deepest target that should be illuminated with good seismic quality. Image quality should start to gradually deteriorate beneath that depth.

Moreover, the shallowest "bright" reflector that can be mapped easily across the seismic volumes is approximately 500 ms in P-wave TWT. This reflector represents the Hoxbar Oolitic formation, which is at a depth of 3,200 ft to 3,500 ft. The Black Bear project final acquisition geometry set the receiver-line spacing to 1,320 ft and the source-line spacing to 1,155 ft. These spacings ensure the reliability of this bright reflector, because the spacing parameters are less than half of the depth to the Hoxbar Oolitic interface.

The seismic survey was not optimally designed to image the Sycamore formation because of two factors: lack of accurate formation top from well data, and the relatively small number of 3C geophones limiting the recording swath size. Figure 19 illustrates how to design the survey to image the primary target. The two key factors here are the shallowest-reflector depth, and the primary-target depth. As stated above, the spacing parameters (receiver-line and shot-line spacing of 1,320 ft and 1,155 ft, respectively) are less than half the depth of the shallowest laterally-recognized bright reflector, the Hoxbar Oolites. This reflector is approximately 3,200 ft to 3,500 ft in depth and about 500 ms in P-wave TWT. The shallowest-imaged reflector is important for procedures such as statics correction and velocity analysis. In synthetic seismogram analysis, this reflector will also be a good well-seismic tie. To properly image the Sycamore formation – the primary target – its depth needs to be less than or equal to the maximum dimension of the recording swath. The calculated primary-target depth from the survey parameters is about 8,865 ft. Unfortunately, well logs – acquired by Schlumberger in 2000 for Gant 1-19 –

show that the depth of the Sycamore formation is about 10,300 ft. This inadequacy in the survey geometry would reduce data quality at the primary-target depth and deeper interfaces.

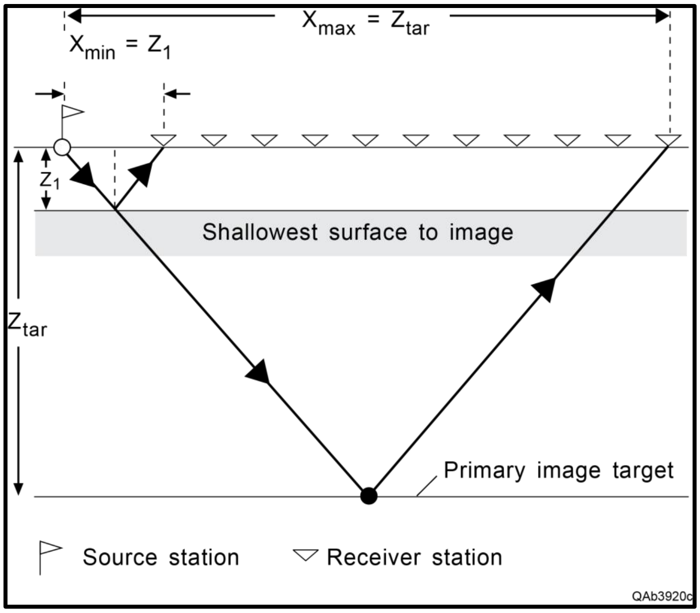

Figure 19. Recording swath analysis (after Hardage, 1997).

This figure shows a sketch of a recording array dimensions as compared to depths of shallowest (Hoxbar Oolites at about 3,200 ft) and primary (Sycamore at about 10,300 ft) targets. The depth to the Hoxbar Oolites is more than twice the receiver-line spacing and the source-line spacing, which fits the design techniques proposed by Hardage (1997). The number of active channels limited the recording swath size, and thus the depth of primary image target. The optimum depth to be imaged is approximately 8,865 ft based on the survey dimensions and recording swath size. This fact will affect the seismic data quality of deeper interfaces.

CDP stacking fold is the number of field traces that are summed together to form a single stacked trace during data processing. One way to define stacking fold is that it is the number of reflection points within a stacking bin when data are acquired with a particular receiver/source grid (Hardage, 1997). 3D stacking fold, *F*, is the product of inline and crossline stacking folds. The stacking fold for the Black Bear survey can be estimated using the following geometrical dimensions of the survey:

- Source-line spacing = 1,155 ft
- Receiver-line spacing = 1,320 ft
- Source-station spacing = 330 ft
- Receiver-station spacing = 165 ft
- Number of receiver lines in swath = 4
- Number of receiver stations per receiver line = 49.

Inline fold F_{IN}, crossline fold F_{XL}, and 3D fold F are then given by:

$$F_{IN} = \frac{1}{2}(Number\ of\ receiver\ channels) \times \left[\frac{Receiver\text{-}station\ interval}{Source\text{-}station\ interval}\right], \tag{1}$$

$$F_{IN} = \frac{1}{2}(49) \times \left[\frac{165}{330}\right] = 12, \tag{2}$$

$$F_{XL} = \frac{1}{2}(Number\ of\ receiver\ lines\ in\ recording\ swath) = \frac{1}{2}(4) = 2, \tag{3}$$

$$F = F_{IN} \times F_{XL} = 12 \times 2 = 24. \tag{4}$$

The planned 3D stacking fold was 24. However, after the survey design was implemented in June 1998, the stacking fold calculated during data processing was 21.

I will show in the next section that the Sycamore formation is positioned at approximately 1,600 ms in P-P TWT. The seismic data analysis will be limited to 2,000 ms in P-P data, and 4,000 ms in SH-SH data. This decision was made for two reasons. First, no deep well control is available because deeper formations were not penetrated by any local well. The absence of deep calibration data does not allow an interpreter to decide if the bright reflectors at approximately 2,500 ms P-P TWT (Figure 5) are related to actual formations or are multiples. Second, SH-SH data do not show reflectors below 4,000 ms which could be used as depth-equivalent events for P-P reflections below 2,000 ms (Figure 6). Because the purpose of this work is to demonstrate P-wave and SH-wave depth-registration, data interpretation was constrained to shallow data where log calibration was available.

WELL SYNTHETIC SEISMOGRAMS

Different methods were used to interpret and validate picked reflecting horizons. Synthetic seismograms computed from borehole log measurements offer a direct tie between the geologic and geophysical data (Figure 20). Due to lack of any type of sonic logs, Gardner's equation (Gardner et al., 1974) was used to relate lithological bulk density to seismic compressional wave velocity for computation of synthetic seismograms. This method has some uncertainty but provides an estimate of the velocity variations encountered in a layered-rock medium for a given lithology. Gardner's equation could be optimized if both sonic and density logs were available for this field; however, as has been stated, no sonic logs were available. Thus generalized Gardner constants were used and assumed to be a good approximation for this project. These methods have been suggested by other researchers and published literature, but to my knowledge, no one has tried the method with 9C/3D seismic data.

The main goal is to create a synthetic trace that best matches the seismic data at the well location in the zone of interest (SynTool^{TM} Software User Guide, 2010). Well synthetic seismograms were created from six well log suites within the Black Bear project area. Those wells are: Gant 1-19, Vera 1-18, Wade 1, Wade 2, Wade 3, and Wade 4 (Table 2 and Figure 7). Bulk density logs were applied to create "pseudo"-sonic logs for these wells. Formation tops are available for the shallow and deep formations penetrated. Gant 1-19 density log extends from 3,250 ft to 11,400 ft, penetrating down to the Hunton Group. However, the other wells penetrate the shallow formations only and extend down to the Deese Group (Figure 12 and Appendix Table 10).

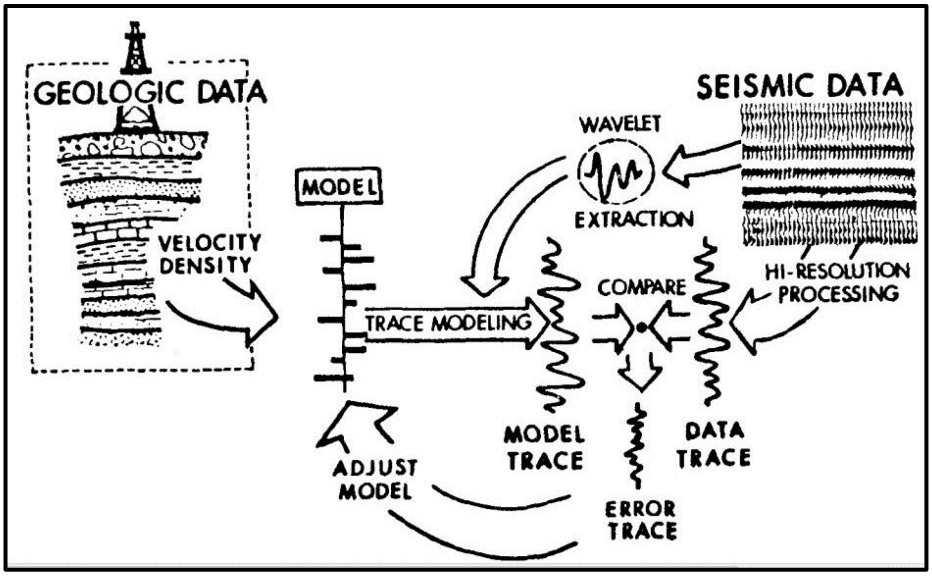

Figure 20. A flow chart for creating a synthetic seismogram (Stommel and Graul, 1978). The synthetic seismogram modeling involves convolving a reflectivity series with a wavelet extracted from a seismic data to be matched. Pseudo-sonic logs, computed from the density logs, were used in this project to create synthetic seismograms due to the lack of velocity data.

To create synthetic reflection traces, density and velocity curves are used to simulate acoustic impedance and reflectivity changes in the earth at the well location, and this reflectivity sequence is convolved with a representative extracted wavelet (SynTool^{TM} Software User Guide, 2010). First, the acoustic impedance log (*Ip*) is derived from the density (ρ) and velocity (V_p) logs. Then the reflectivity series (*RC*) is calculated from these acoustic impedances as follows:

$$I_P = \rho \times V_P, \tag{5}$$

$$RC = \frac{I_{P2} - I_{P1}}{I_{P2} + I_{P1}}. \tag{6}$$

The velocity log, V_p, is estimated from the bulk density log, ρ, using Gardner's relation. The general Gardner constants were used as follows:

$$\rho = 0.23V_P^{0.25}, \tag{7}$$

$$V_P = \left(\frac{\rho}{0.23}\right)^4. \tag{8}$$

Once the reflectivity series is extracted (Equation 6), that series is convolved with a wavelet to produce a 1D synthetic trace. There are several methods of estimating approximate seismic wavelets, and the usefulness of a synthetic trace depends on the accuracy of the well log and the type of wavelet used. In this work, a wavelet from the P-P data was extracted statistically after comparing the reflectivity trace to a portion of the seismic data. This technique should ensure the extraction of a best-match wavelet.

Because the velocity curve does not extend to the surface, a replacement velocity of 10,000 ft/s was assumed for the layer from the time datum to the log starting point. This assumption can be fine-tuned to create a better match. A correlation coefficient is a quantitative estimation of the similarity between a synthetic trace to one or more seismic traces near the well location. This similarity can be improved by time- and phase-shifting of the synthetic trace relative to the seismic data. The synthetic trace is autocorrelated with the seismic data over the time range of the velocity curve. This procedure affects only the amplitudes of the synthetic trace and leaves the data at zero-phase. The synthetic trace is then shifted up or down to get a higher correlation coefficient. This time-shift can be anywhere from a few milliseconds to several tens of milliseconds. Any applied time-shift will modify the replacement velocity of the first layer. A good constraint for the velocity in this shallower layer is to ensure that the value is between 5,000 ft/s and 12,000 ft/s. Mixed-phase wavelets account for phase rotation that takes place through wave propagation in the subsurface. However, a mixed-phase wavelet should not be extracted from the seismic data until an attractive zero-lag time is achieved between the seismic data and a synthetic seismogram.

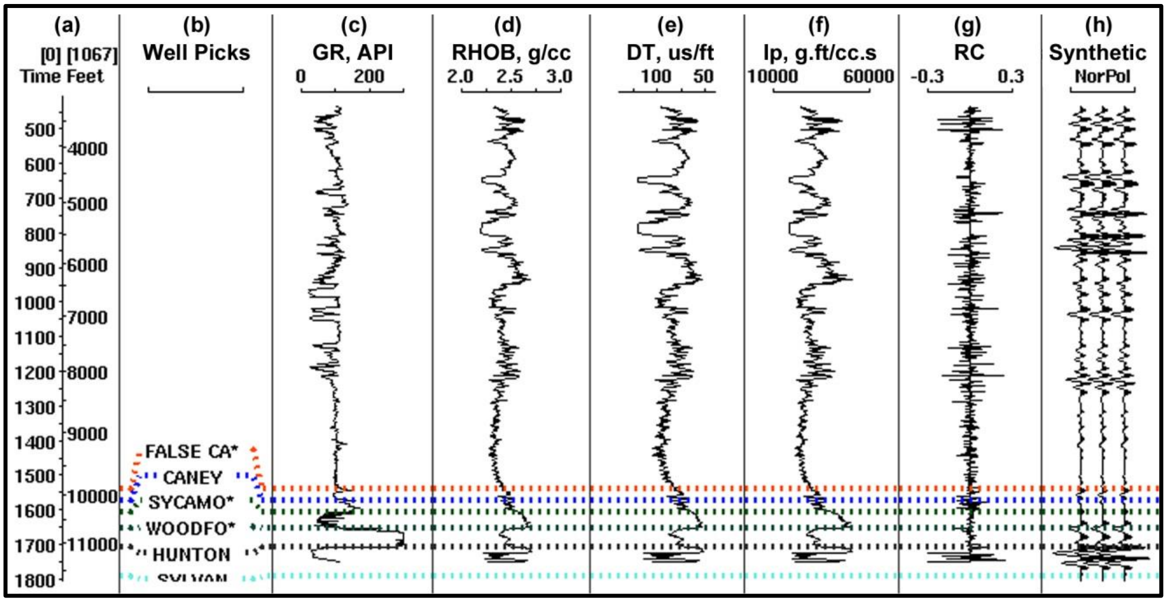

Figure 21. Well Gant 1-19 synthetics from logs.
The impedance curve (f) is the product of bulk density (d) and pseudo-sonic logs (e). The reflectivity series (g) is calculated using Equation (6), which leads to a synthetic trace (h) using a convolution operator.

In this work, a Wiener-Levinson mixed-phase wavelet was extracted at each well after achieving zero-lag time. Several synthetic traces were extracted for each well, using different correlation windows and AGC values. Then, for each well, a time-depth table was created and implemented. At the Gant 1-19 well location there are two sets of bright reflectors, which is why that well has three correlation windows and corresponding time-depth tables. AGC was applied at different window lengths to enhance the amplitude and S/N. However, for the most part, these varying AGC windows did not help the well-to-seismic correlation.

Figures 21 and 22 show the data used to create a synthetic seismogram for Gant 1-19 and Wade 1, respectively. The time-depth tables (a) were estimated from density-derived pseudo-velocity data. Formation tops (b) for Gant 1-19 were available for the deeper formations only which added more challenges in correlating the upper section with Wade 1 and other wells. Gamma-ray (c) data were used to double-check the synthetic correlation with other wells for the shallow section of Gant 1-19. Bulk density (d) and pseudo-sonic (e) logs were used to create the impedance (f) and reflectivity series (g) logs.

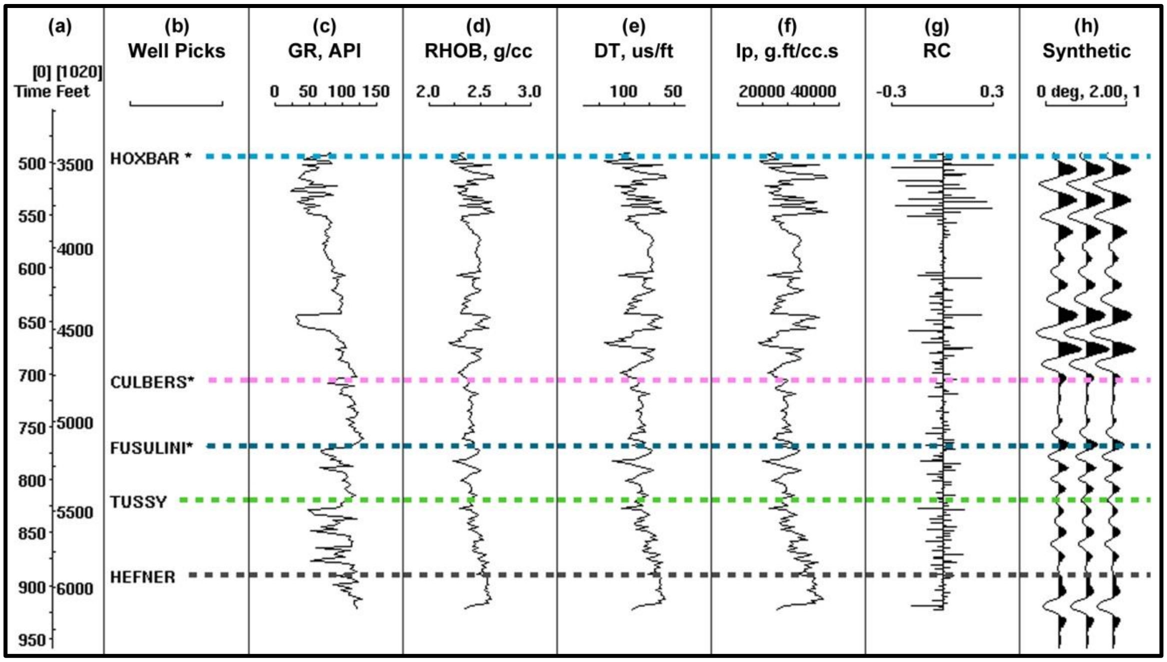

Figure 22. Well Wade 1 synthetics from logs.
The impedance curve (f) is the product of bulk density (d) and pseudo-sonic logs (e). The reflectivity series (g) is calculated using Equation (6), which leads to a synthetic trace (h) using a convolution operator.

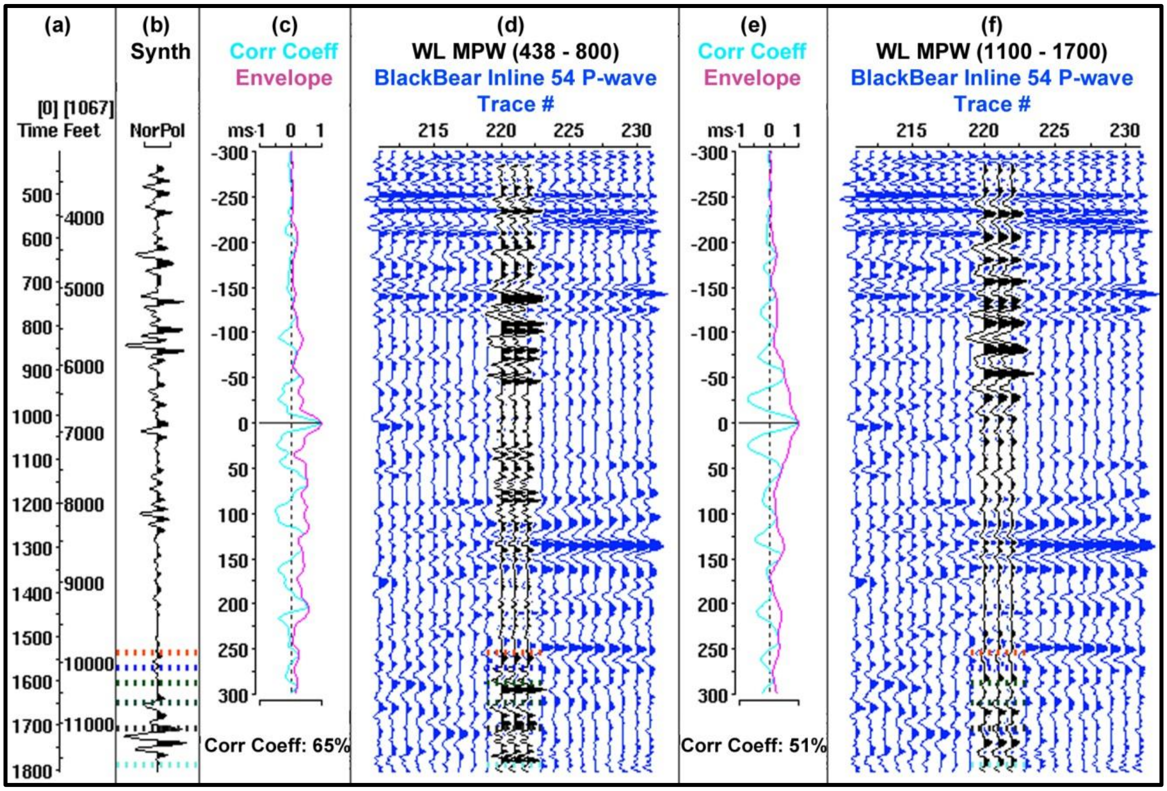

Figure 23. Gant 1-19 well-to-seismic tie using Wiener-Levinson mixed-phase wavelet (WL MPW) with no AGC applied.
This figure shows synthetic seismograms (WL MPW) over the window 438 – 800 ms (d) and a window 1,100 – 1,700 ms (f) overlaying corresponding seismic data. The WL MPW generates several wavelets and then matches the synthetic trace with the seismic data (after trace shifting to achieve zero-lag). The correlation coefficient (c) for the seismogram (d) is 65% which corresponds to the shallow reflectors. The correlation coefficient (e) for the seismogram (f) is 51% which corresponds to the deeper reflectors.

Figures 23 and 25 show the synthetic seismogram correlation for well Gant 1-19 with the P-P seismic data. A Wiener-Levinson mixed-phase wavelet (Figures 24 and 26) was used to create the seismogram over P-P window 438 – 800 ms (d), and P-P window 1,100 – 1,700 ms (f). The synthetics created in Figure 23 do not have an AGC operator applied, while the synthetics in Figure 25 have an AGC operator over a window of 500 ms. The AGC operator enhanced the signal of the deeper reflectors on Gant 1-19, and improved the correlation coefficients. Before applying the AGC operator, the correlation coefficients were 65% (c) and 51% (e) for the shallow and deep windows, respectively. After applying a 500 ms AGC window, those coefficients were increased to 66% and 59%, respectively.

Figure 27 shows the synthetic seismogram correlation for well Wade 1 with the seismic data. A Wiener-Levinson mixed-phase wavelet (Figure 28) was used to create the

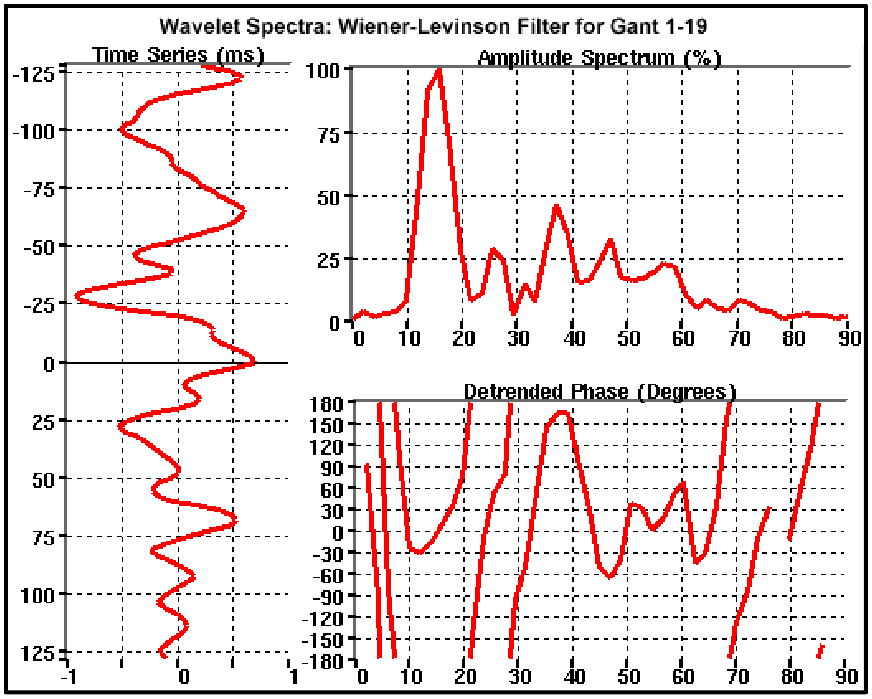

Figure 24. The wavelet spectra extracted for well Gant 1-19 synthetic seismogram (1,100 – 1,700 ms).
The wavelet was extracted from the P-P seismic data (over the window 1,100 – 1,700 ms) using Wiener-Levinson mixed-phase wavelet method to create well Gant 1-19 synthetic seismogram.

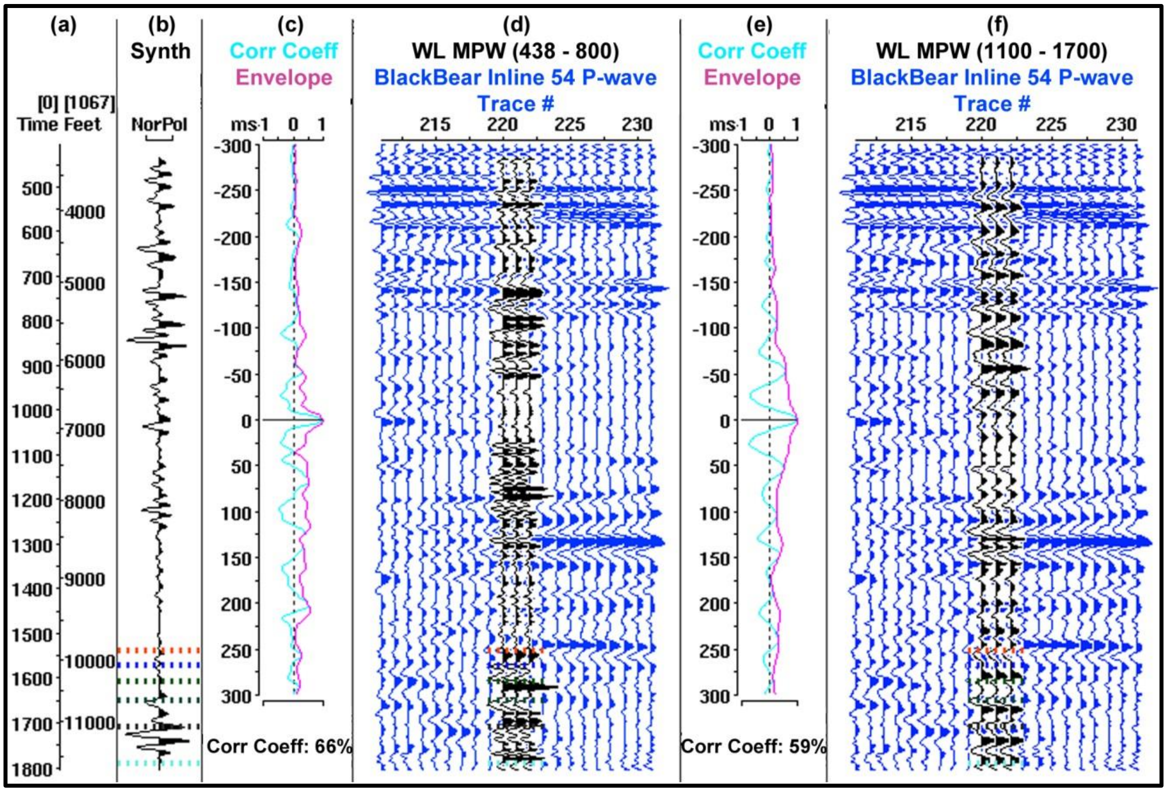

Figure 25. Gant 1-19 well-to-seismic tie using WL MPW with AGC applied.
This figure shows synthetic seismograms (WL MPW) over the window 438 – 800 ms (d) and a window 1,100 – 1,700 ms (f) overlaying corresponding seismic data. The correlation coefficient (c) for the seismogram (d) is 66% which corresponds to the shallow reflectors. The correlation coefficient (e) for the seismogram (f) is 59% which corresponds to the deeper reflectors. AGC operator enhanced the amplitude of the deeper reflectors, and increased the correlation coefficient across both windows.

seismogram over the window 492 – 916 ms. The seismogram (d) does not have an AGC operator applied, while the seismogram (f) has an AGC operator over a window of 500 ms. The AGC operator increases the amplitude of the deeper reflectors. However, the correlation coefficient without applying the AGC operator (75%) was higher than when an AGC window of 500 ms was applied (71%).

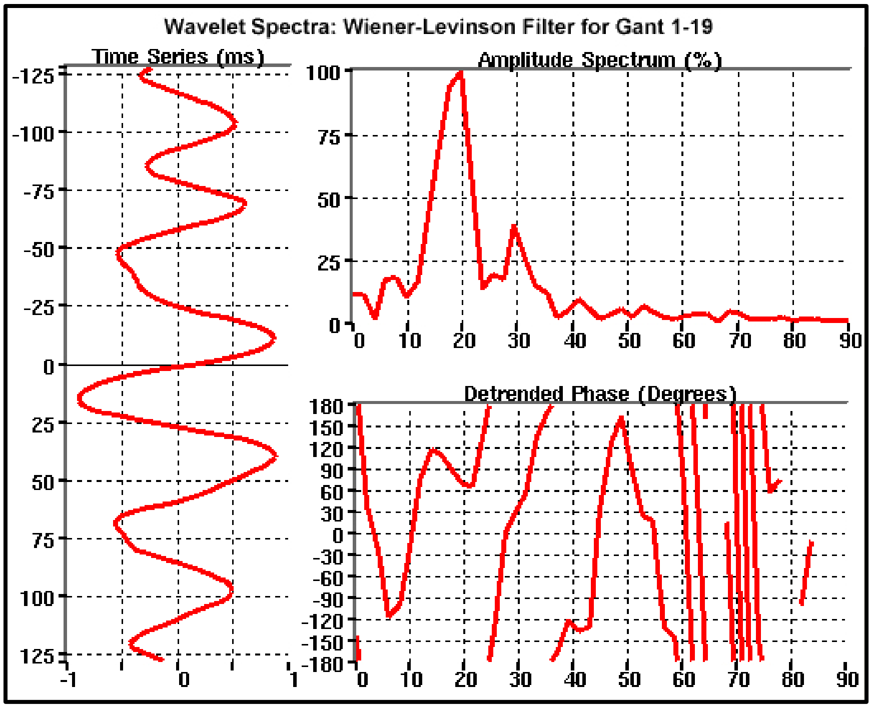

Figure 26. The wavelet spectra extracted for well Gant 1-19 synthetic seismogram (438 – 800 ms).
The wavelet was extracted from the P-P seismic data (over the window 438 – 800 ms) using Wiener-Levinson mixed-phase wavelet method to create well Gant 1-19 synthetic seismogram.

EFFECTIVE DISPLAY

There are numerous ways to display seismic data. I will describe how these data display options affect seismic data analysis.

Color Scales

New 3D visualization technology allows seismic interpreters to analyze huge data sets (Sheffield et al., 1999). The purpose of this section is to understand the use of color in seismic interpretations.

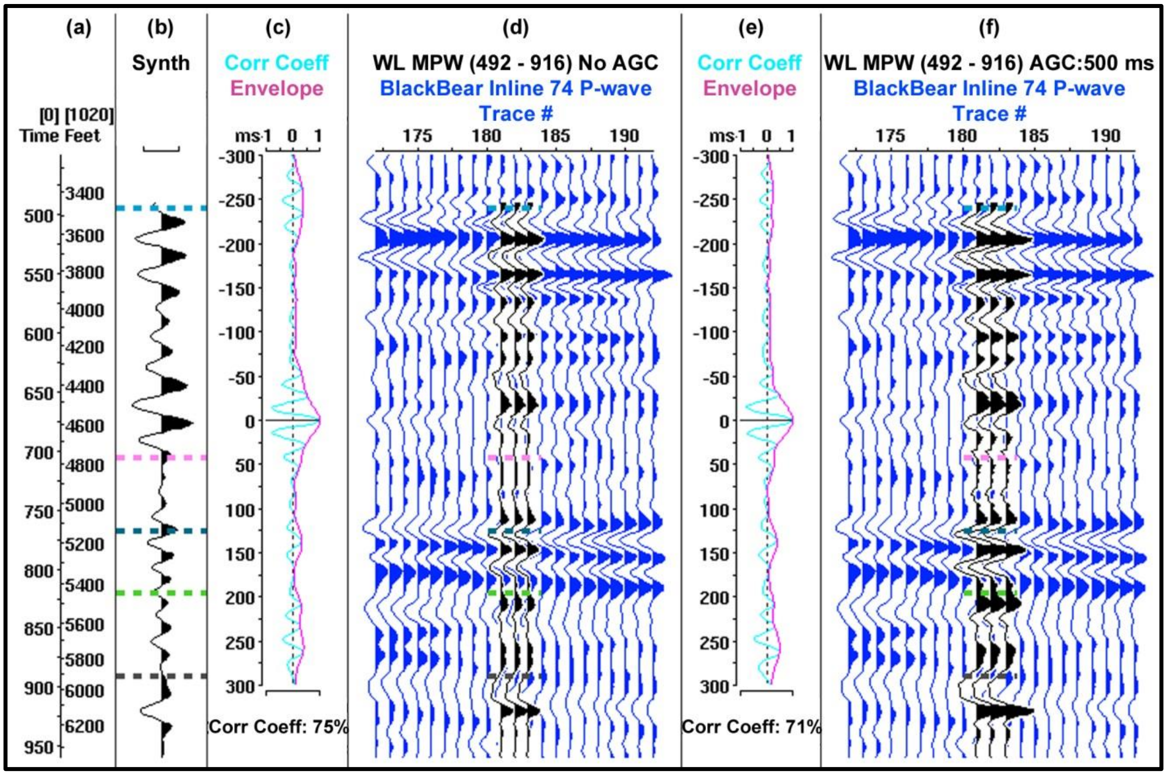

Figure 27. Wade 1 well-to-seismic tie using WL MPW.

This figure shows synthetic seismograms (WL MPW) without AGC (d) and with a 500 ms window of AGC (f) overlaying corresponding seismic data. The correlation coefficient (c) for the seismogram (d) is 75% over the window 492 – 916 ms. The correlation coefficient (e) for the seismogram (f) is 71% over the same window.

Figure 29 shows crossline profile 190 with different color scales. The left panel shows the color scale that was used in picking horizons and interpretation in this project. The right panel shows the same section with a grayscale color scale. Although this view is good for structural interpretation, it is not effective in horizon mapping. The gradual variation of color from a black peak to a white trough makes it difficult to trace the continuity of a horizon. Moreover, for an effective display, the use of black as a screen background is recommended.

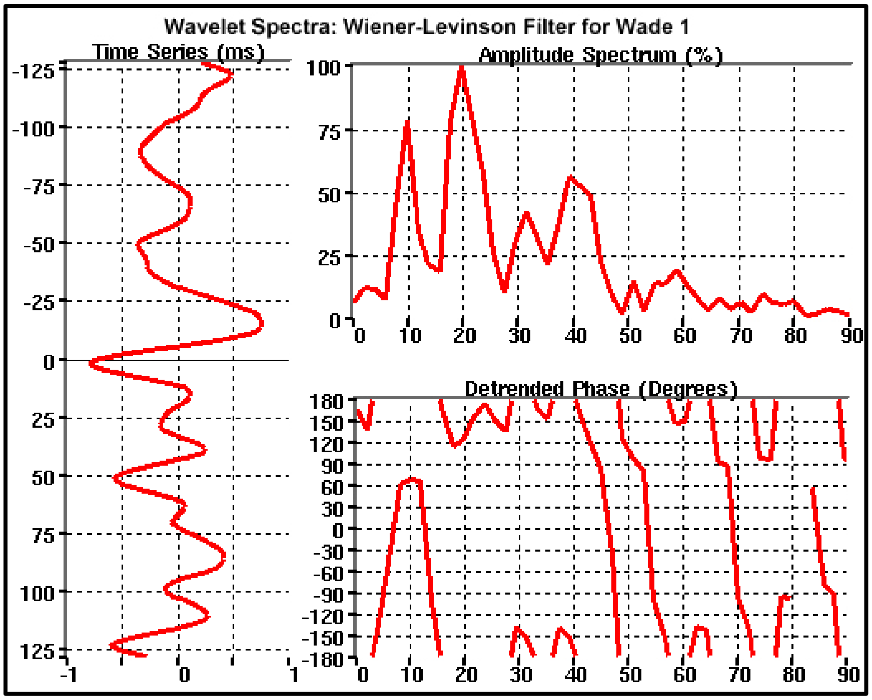

Figure 28. The wavelet spectra extracted for well Wade 1 synthetic seismogram (492 – 916 ms).
The wavelet was extracted from the P-P seismic data (over the window 492 – 916 ms) using Wiener-Levinson mixed-phase wavelet method to create well Wade 1 synthetic seismogram.

Squash Plots

Squash plotting is a technique of analyzing vertical exaggeration to enhance structural interpretation. Figure 30 shows two panels of a vertical seismic profile along the dip of the Sho-Vel-Tum field. The squash plot (b) shows a vertically-exaggerated version of profile (a). Grayscale was chosen as the effective color scale to enhance fault interpretation. It is clearly noticed that faults and gently dipping structures are better perceived on (b). This technique was used to enhance structural interpretation by viewing multiple squash-plot panels simultaneously to allow a field-wide sense of fault patterns.

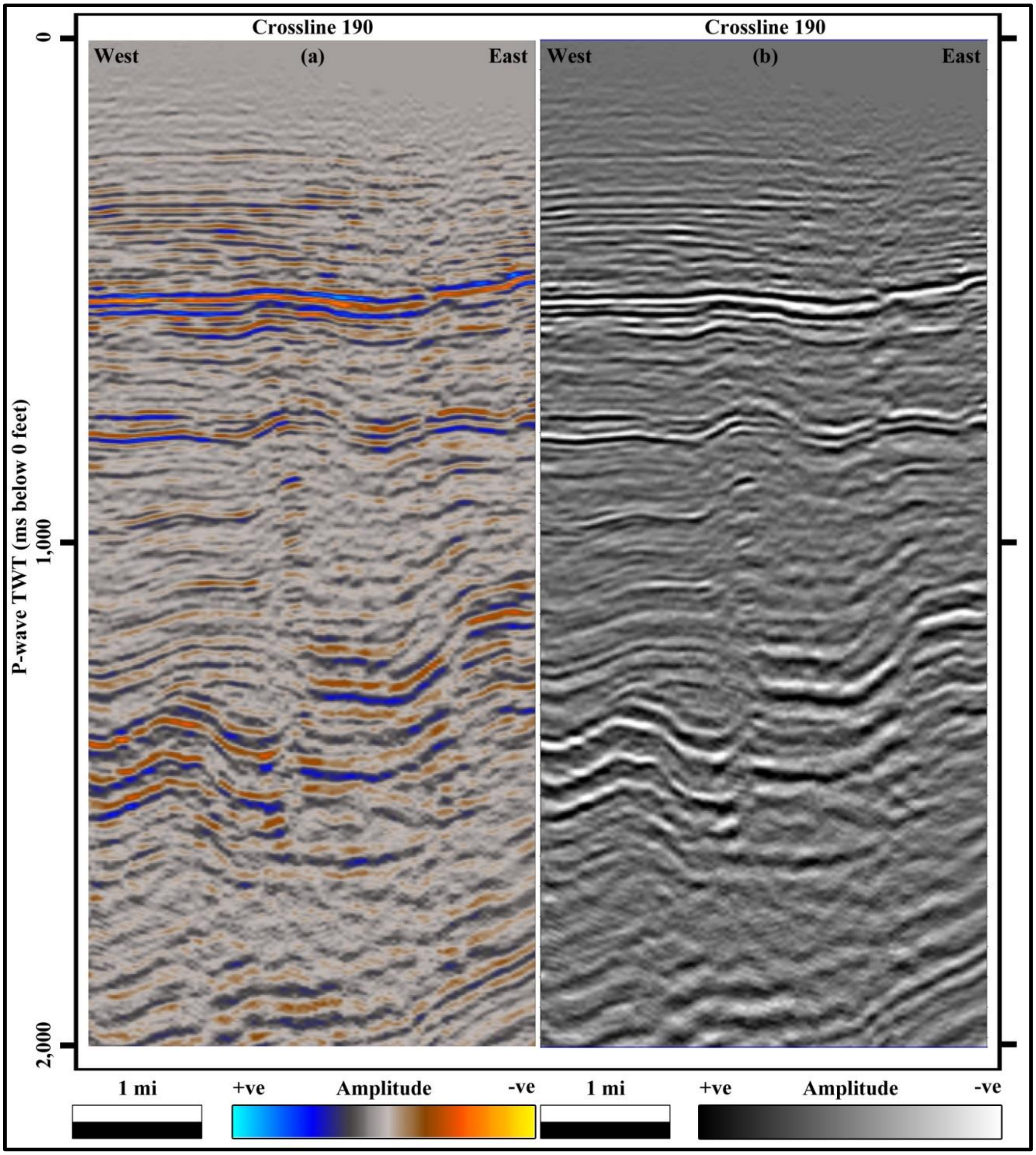

Figure 29. Color scale significance in horizon picking (crossline 190).
The variable colors (a) show more horizon continuity. The grayscale image (b) provides a better structural image and enhances discontinuities.

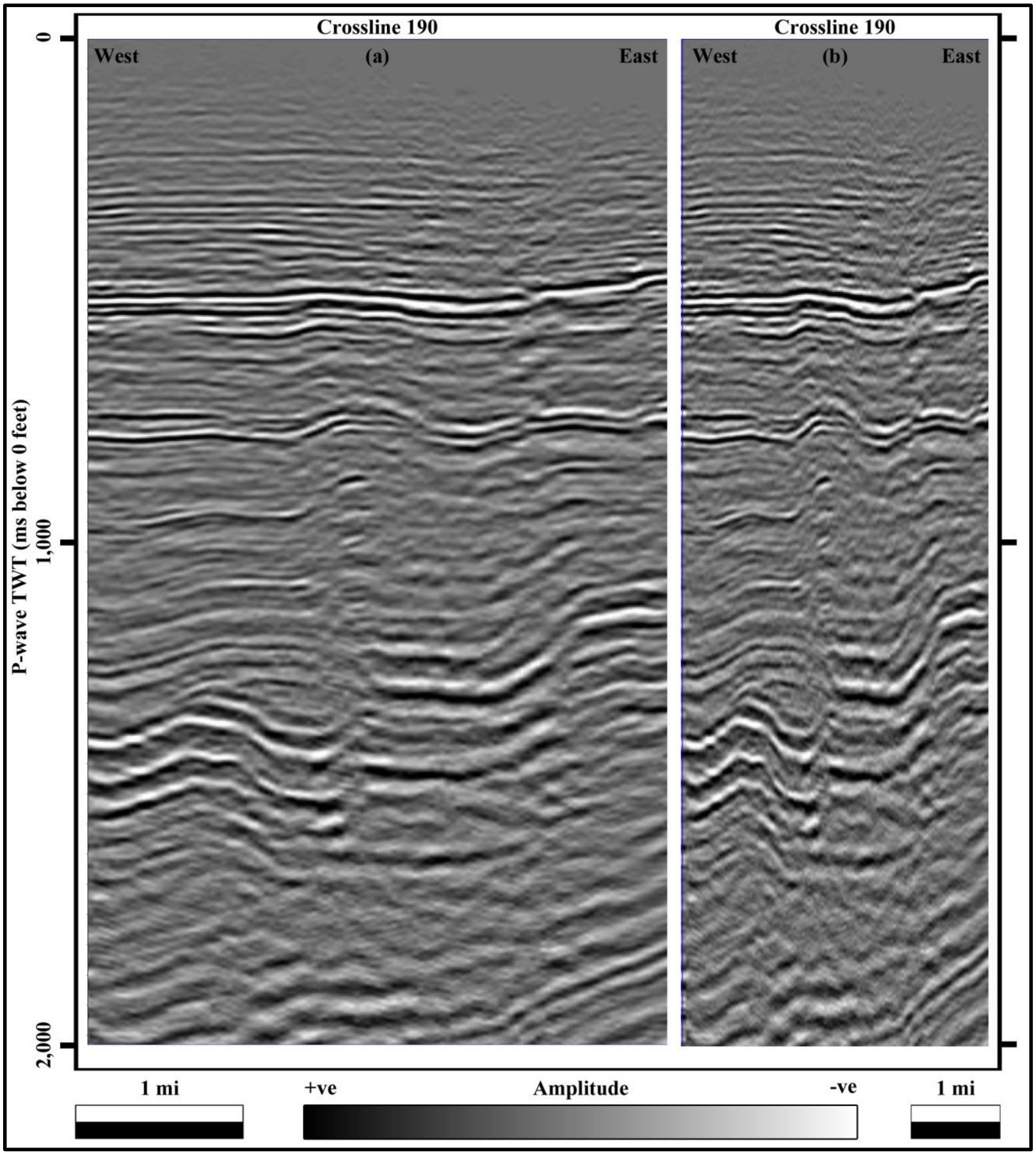

Figure 30. Squash plot technique for structural interpretation (crossline 190).

Squash (vertically exaggerated) plots (b) amplify apparent structural dip visualization and make faults discontinuities stand out and line up. Fault planes can be followed more easily on (b) rather than on (a).

Squash plots were printed out for P-wave and SH-wave seismic data showing vertical profiles of multiple crossline sections evenly spaced across the seismic survey. A sample is shown in Figure 31. Color, saturation, brightness, and contrast are perceived differently by the human eye looking at a monitor compared to looking at printouts. There are several benefits to each method, so using both techniques gives a better perspective of the structure. Using old-fashioned printouts of several panels, preferably with wiggle overlays, gives an interpreter a closer look at the data. However, it is inefficient and time-consuming to print every inline and crossline of a 3D volumetric survey. In contrast, the dynamic environment of a computer gives interpreters more freedom to flip through panels. In particular, the possibility of viewing multiple windows in 2D and 3D views simultaneously increases the confidence of interpretation.

Therefore, I decided to start my interpretation on paper, starting with structural fault mapping and ending with depth-registration on the P-wave and SH-wave panels. Then, I transferred those interpretations to the computer and extrapolated my paper-based interpretations across all inline and crossline sections.

STRUCTURAL ANALYSIS

Well synthetic seismograms relate geophysical data with geological data. The synthetics gave a clue about which reflectors belonged to what group of formations. Faults and terminations against unconformities were used as structural tie points between the P-wave and the SH-wave volumes. These techniques were invaluable when interpreting the seismic data.

Fault interpretation can be accomplished if fault locations and throws are discernible. Minor faults, however, have a minute reflector offset that make it difficult to detect on seismic data. Although seismic acquisition is designed to record wide-azimuth data, the CDP stacking process destroys the azimuthal information contained in the data (Chopra, 2002). Coherence time slices – calculated for a constant time – were used as initial step in structural interpretation because this method delineates faults and fractures without bias of previous interpretations. Coherence values range from +1 to -1. A value of +1 suggests a perfect match between adjacent traces, while a value of -1 indicates perfect trace similarity of the trace waveform was inverted. Any value close to zero, positive or negative, indicates no correlation in seismic character between adjacent traces, which can be caused by faults. Therefore, seismic coherency can be a measure of lateral variations cause by changes in structure, stratigraphy, lithology, porosity and the presence of hydrocarbons (DeAngelo and Wood, 2001; Bahorich and Farmer, 1995; Marfurt et al., 1998). Interpreters choose what fault to map in conventional fault mapping; the resultant number and intensity of faults are thus highly variable. The benefit of structural volume visualization is the effectiveness of showing subtle and complex fault patterns. The time and effort allocated for fault mapping should match the project objectives. At the prospect level, small faults become significant as they may compartmentalize reservoirs (Kidd, 1999).

To interpret the structure and simultaneously look at different slices of the field, printouts of squash plots were created along crossline sections spaced approximately every 200 meters (similar to Figure 31). Grayscale theme was chosen to enhance discontinuities and to amplify the structural variations, especially for gently dipping reflectors.

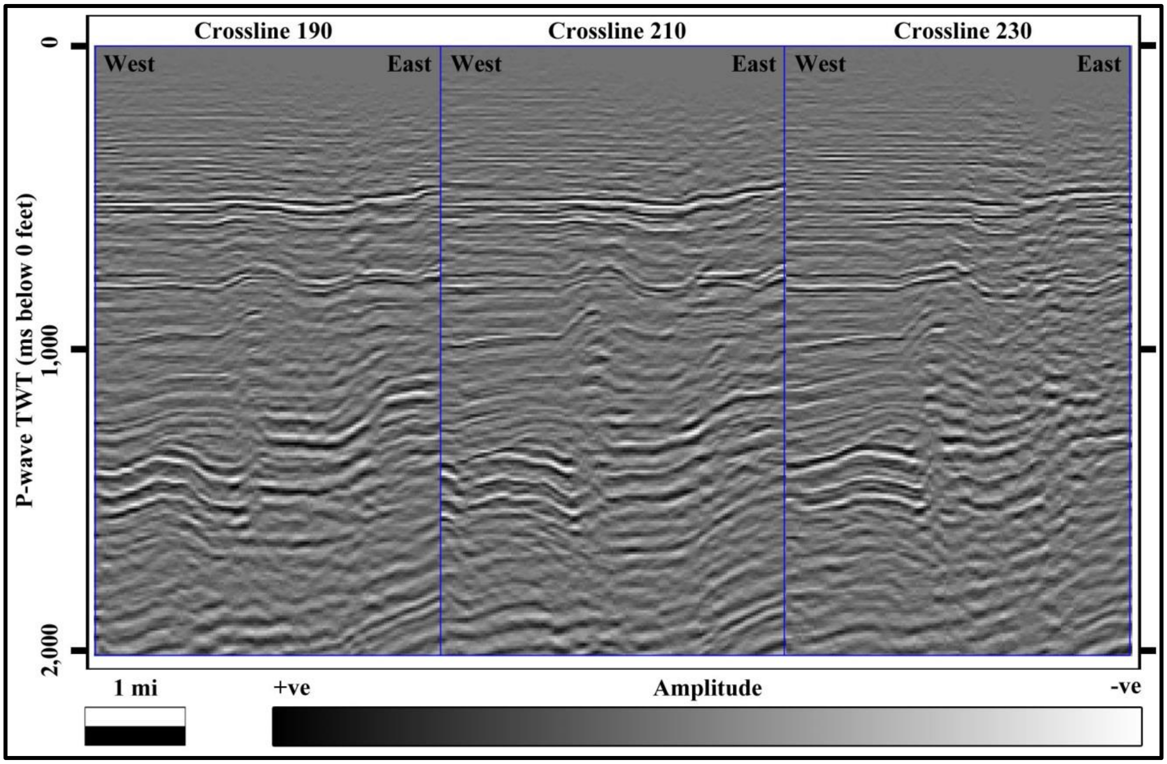

Figure 31. A sample setup used for structural analysis of P-wave data.
A grayscale theme enhances discontinuities and highlight structural packages. Squash plots give the interpreter a simultaneous field-wide look at the structure.

Seismic attributes, like coherence, were used to visualize faults. Discontinuity time slices (Figures 32 and 33) revealed fault trends and orientations. This approach allowed me to map separate faults without mistakenly mapping several faults as one continuous fault. Interpretation software packages allow stacking discontinuity time slices to create discontinuity volumes. I created a discontinuity volume, made the discontinuous points opaque, and hid the continuous points. The result is a set of floating fault planes. There are some issues regarding the definition of “discontinuous” by some interpretation software packages. The original attribute checks reflector discontinuity by looking at surrounding traces that have the same time sample. Given that definition, the

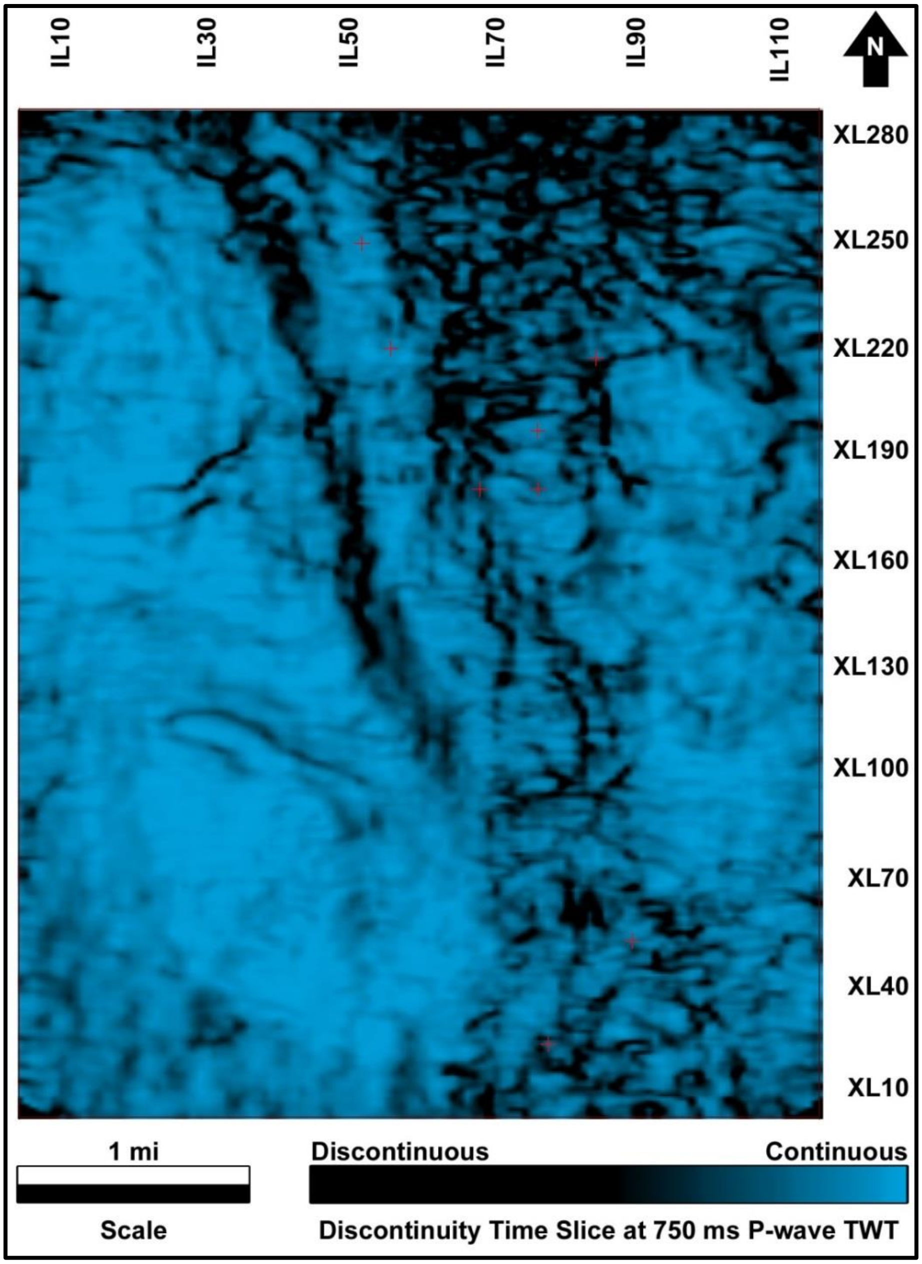

Figure 32. Discontinuity time slice at 750 ms in P-wave TWT.

A possible system of faults trends NNW to SSE. Disturbed source-receiver geometry, caused by surface obstacles during acquisition, may be the cause of the low-quality seismic data in the NE part of the seismic survey.

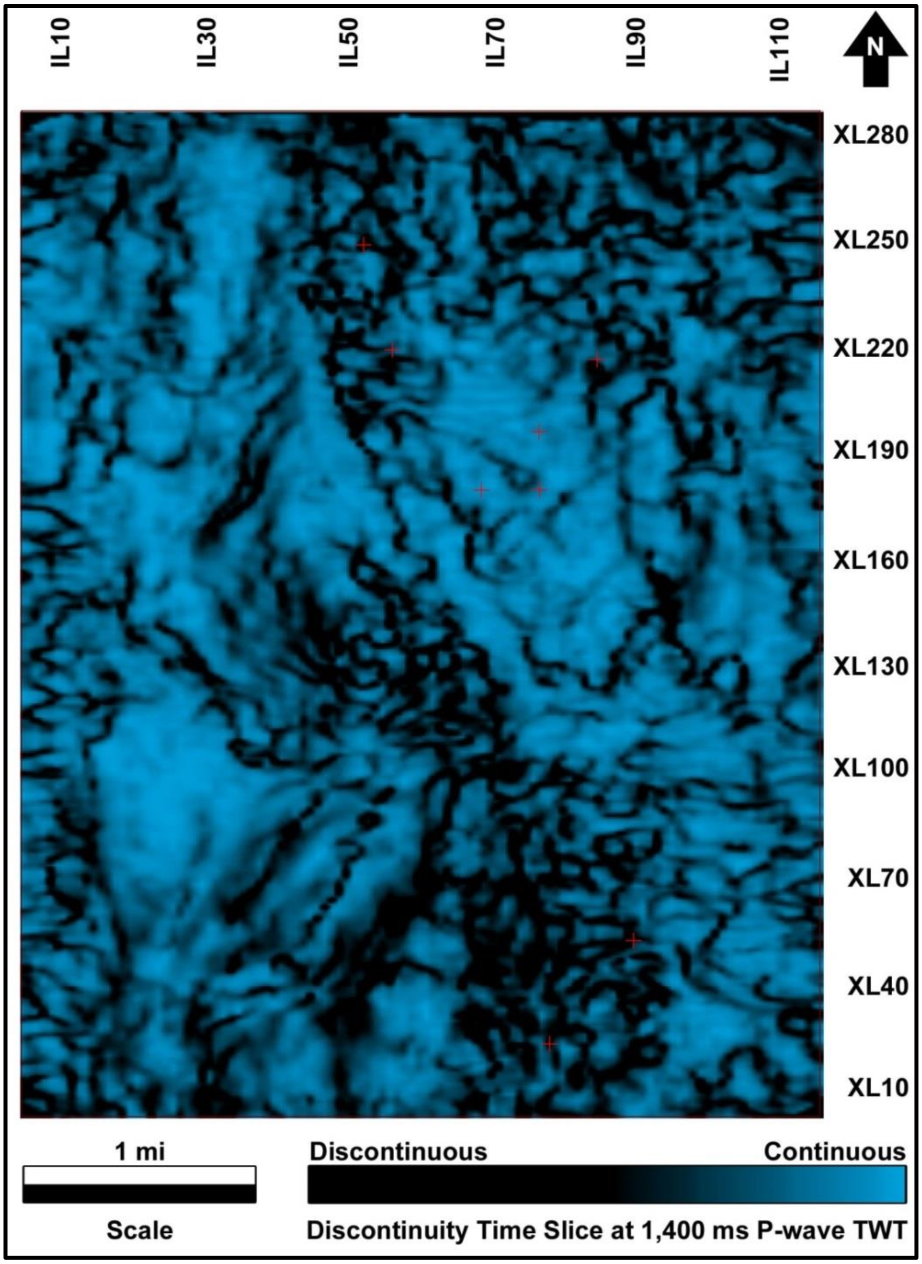

Figure 33. Discontinuity time slice at 1,400 ms in P-wave TWT.

A more complex structure with additional, less-intense, fault trends is shown. This discontinuity slice shows, besides faults, intensively fractured regions in the north and south parts of the survey.

intersection of a time slice with a dipping formation will look like a fault along the strike of the formation. A more recent version of this attribute accounts for the dip of the reflector when checking for discontinuities.

DEPTH-REGISTRATION

Three panels along the dip of the structure (crosslines 190, 210, and 230 as in Figure 31) were chosen to act as starting points for the registration for two reasons. First, the pseudo-synthetic from well Gant 1-19, located nearby, is valuable as well control. Second, these profiles have relatively good data quality and possible use of structural "tie" points. The importance of structural interpretation imposes itself in the depth-registration workflow. If the survey coordinates system is *XY* in map view and Z in TWT, a fault's *XY* location should be in the same in both the P-P and SH-SH data. Even though reflectors have different P-wave and SH-wave time signatures, they should have the same structural architecture. These three panels were printed out on large displays using an Amplitude Pk (Yellow-Red-Brown-Gray-Black-Blue-Cyan) color scale and right-filled wiggle overlay data. 10 in/s and 10 trace/in were used for the P-wave section, and 5 in/s and 10 trace/in were used for the SH-wave section. A band pass filter was applied to the P-wave data to simulate the SH-wave data frequency content. These printouts were used to visually interpret reflectors, unconformities, faults, and amplitude changes to decide which reflectors were depth equivalent. S-wave data are usually set at half the vertical scale when viewed against their corresponding P-wave data to compensate for the S-wave and P-wave velocity differences (Sheriff and Geldart, 1995). A practical assumption is to begin by setting the V_p/V_s to 2.0.

Interpretation times were then transferred to DecisionSpace Desktop (DSD). The P-wave horizons were mapped first because they had better continuity and structural signature. Four simultaneous views were used to speed up and enhance horizon picking. The first data window showed dip-oriented sets of panels at 15-crossline steps. The second window had strike-oriented sets of panels at 5 or 10-inline steps. The third window showed a map view of the seed horizon color-coded to emphasize structural variations. The fourth window showed a perspective visualization of the seed horizon and a 3D floating cube. The 3D cube acted as a quality-control display to make sure there were no bad picks on a loop around the cube.

The next step was to transfer the SH-wave time horizons that were mapped on the printouts. Even though the view was set to V_p/V_s of 2.0, shallow formations have much higher V_p/V_s. Thus, as a starting point, depth-equivalent horizons on the SH-wave data were expected to be a few tens of milliseconds below twice their P-wave TWT.

The pseudo-P-wave horizons were created (Table 5) to guide SH-wave horizon mapping. The TWT for the P-wave horizons were multiplied by a factor of 2 and c milliseconds were added to the product (last column, Table 5). Because the structure is the same whether it is imaged by P or SH data, it is helpful to overlay P-wave information on the SH-wave displays for mapping depth-equivalent horizons.

The pseudo-P-wave horizons were viewed on the SH-wave data to estimate where the depth-equivalent SH-wave horizon would be. The SH-wave horizons will not necessarily look the same as their depth-equivalent P-wave horizons due to lateral velocity variations between the P-wave and SH-wave velocities. However, the general structural signature of the P-wave horizons guided the SH-wave horizon mapping.

Table 5. Pseudo-P-horizons on crossline 230, trace 2.

Horizon number	TWT (ms)			
	SH-wave pick	P-wave pick * 2	*c*	Pseudo-P-wave pick
1	1,168	1,033	135	1,168
2	1,746	1,572	174	1,746
3	2,100	1,962	138	2,100
4	2,491	2,379	112	2,491
5	2,746	2,696	50	2,746
6	2,820	2,792	28	2,820
7	3,004	2,914	90	3,004

T_S/T_P ANALYSIS

This method tests the stability of the picked reflection times on horizons and validates or disproves any lateral variations in interval V_p/V_s. This analysis was applied by Pardus et al. (1990). More details about this work are available in Tatham and McCormack (1991b, 216–225).

This type of analysis validates the accuracy and consistency of both the horizon mapping and computed V_p/V_s values. The analyzed time intervals range from 130 ms to 1,100 ms P-wave reflection time in all possible combinations of intervals between horizons H1 through H4. The analysis was performed on 3 inline sections and 4 crossline sections distributed evenly throughout the seismic survey; results then were extrapolated to the remaining sections.

The time intervals were too large to interpret variability in V_p/V_s in very small interval that might result from lateral lithology and velocity changes. Intervals identified by Pardus et al. (1990) were used to interpret lateral variations in dolomite percentage within limestone beds, which are confirmed by existing well data. However, due to the lack of accurate well ties and the thick mapped intervals in the Black Bear dataset, such detailed analysis was difficult here.

Horizons H1 through H4 were used to estimate t_s/t_p values in 10 overlapping intervals, including four consecutive intervals (Surface to H1; H1 to H2; H2 to H3; and H3 to H4) and six redundant intervals (Surface to H2; Surface to H3; Surface to H4; H1 to H3; H1 to H4; and H2 to H4). Analysis of consecutive intervals reveals mis-picks in either or both of P-wave and SH-wave horizon picks. To evaluate the accuracy of H_n, both the H_nP and H_nSH horizon picks need to be examined. Assuming H_{n-1} and H_{n+1} are stable horizons, a mis-pick in H_n would show as a mirrored spike between the t_s/t_p curve of H_{n-1} to H_n interval and the t_s/t_p curve of H_n to H_{n+1} interval. Moreover, this mis-pick would not show on the t_s/t_p curve of H_{n-1} to H_{n+1} interval, which emphasizes the importance of analyzing redundant t_s/t_p intervals. A mis-pick with high t_s/t_p (equivalent to a high V_p/V_s) would suggest overestimating the S-wave TWT or underestimating the P-wave TWT for the analyzed horizon. Results of this analysis are included in Chapter 4.

Chapter 4: Results and Discussions

This chapter summarizes the results of this project, starting from well synthetic seismograms based on subsurface well logs, structural analysis, and t_s/t_p-editing to achieve depth-registered horizons.

WELL SYNTHETIC SEISMOGRAMS

The P-P wave synthetic seismograms tied reflectors and geologic formations. Synthetics from six well log suites were created using density logs and the Wiener-Levinson mixed-phase wavelet method. These traces were produced with and without AGC. The AGC operator did not always improve the correlation coefficient between the synthetic P-wave seismic trace and a near-by stacked trace. In fact, as expected, an AGC operator reduced correlation in some cases (Table 6). However, deeper reflectors were visually enhanced after applying an AGC operator.

Table 6. Wells with synthetic seismograms and their corresponding correlation coefficients between the synthetic seismogram and actual seismic reflection traces.

Well name	Correlation window (ms) used for the extraction of Wiener-Levinson mixed-phase wavelet	Correlation coefficient	
		No AGC	AGC: 500 ms
Gant 1-19	438 – 1,752	32%	36%
	438 – 800	66%	65%
	1,100 – 1,700	59%	51%
Vera 1-18	510 – 858	73%	73%
Wade 1	492 – 916	75%	72%
Wade 2	494 – 926	85%	83%
Wade 3	396 – 864	73%	71%
Wade 4	480 – 998	64%	59%

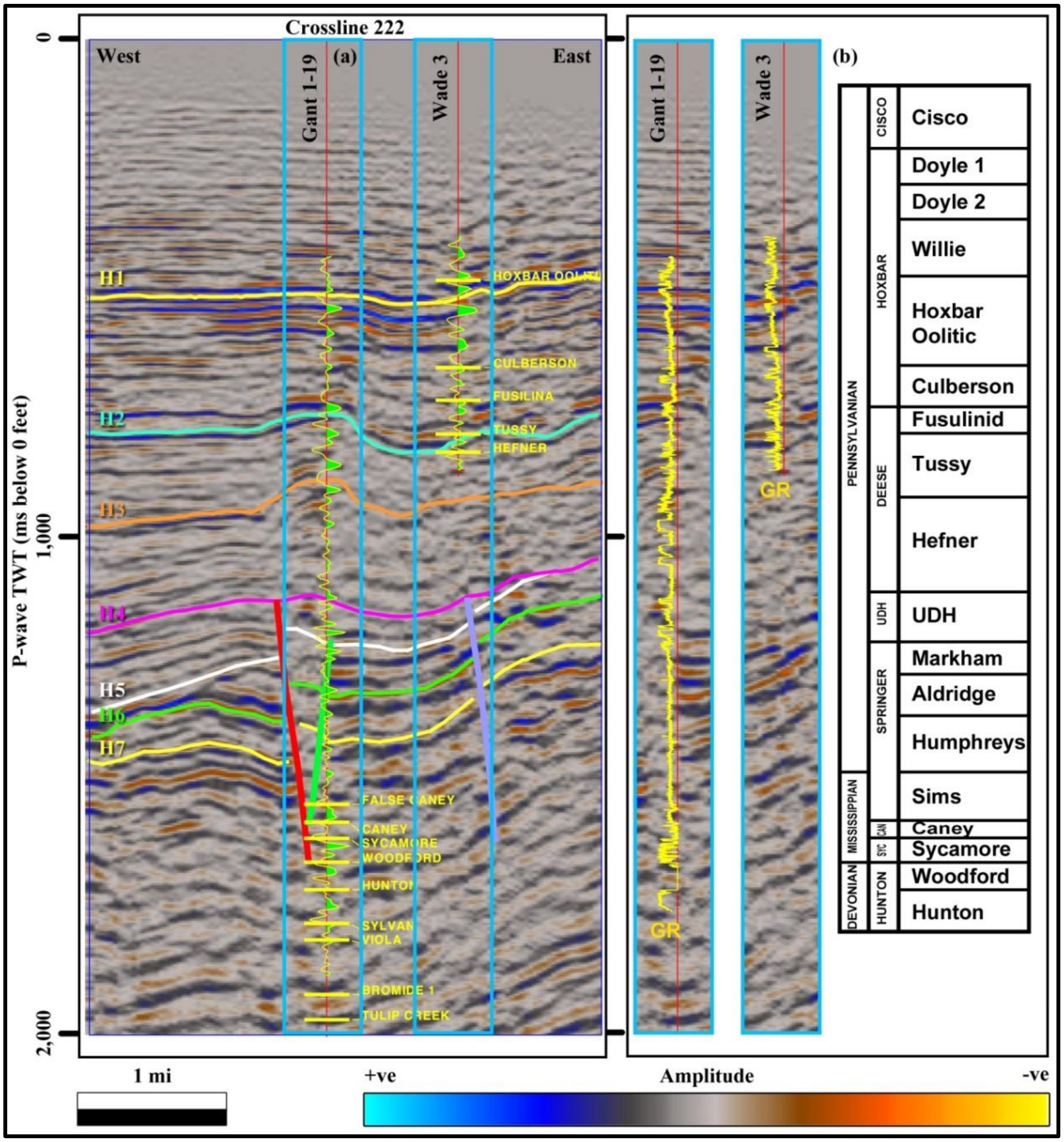

Figure 34. Identification of seismic reflections at the Gant 1-19 and Wade 3 well locations.

(a) The Wade 3 showed a correlation coefficient between the synthetic seismogram constructed from the density log and the nearest seismic reflection of 73%. Gant 1-19 showed correlation coefficients of 66% over the shallow reflectors window and 59% over the deeper reflector window. A detailed stratigraphic column (b) relates the reflections to the geologic section.

Figure 34 shows two synthetic seismograms calculated from density logs in the boreholes, Gant 1-19 and Wade 3, using the Wiener-Levinson mixed-phase wavelet method to extract an appropriate wavelet. An AGC amplitude adjustment with a 500 ms window was applied. Formation tops are shown on the vertical projection of the two wells. Gant 1-19 is the only well that penetrates the deeper reservoirs. This synthetic seismogram has a correlation coefficient of 66% with the observed seismograms for shallow reflectors and 59% for deeper ones. Wade 3 and the other wells penetrate only the shallow reservoirs, and show a correlation coefficient of 73% (Table 6) with the observed seismic data at the depth in question. These correlation coefficients are considered relatively low. However, the major limitation is the absence of velocity data. This interpretation approach was forced to assume that the Gardner et al. (1974) density-velocity correlation was valid. The results should improve significantly if sonic logs, monopole or dipole, become available.

STRUCTURAL ANALYSIS

The link between the seismic data and the regional geology was the well synthetic seismograms at well locations. These seismograms tied the unconformities and structural features observed in the seismic data to the stratigraphic column.

First, the seismic data did not have constant quality across the survey area. Data in sections 17 and 20 (Figure 4) had lower fold due to surface obstacles that did not allow sources and receivers to be placed in their planned locations. The low-fold effect is evident from the low S/N in the corresponding seismic data around that area on both the compressional and shear volumes. In general, the S/N is higher for the P-wave volumes than for the SH-wave volume. This difference between P and SH image quality is why the main structural interpretation and fault analysis was first performed on the compressional wave data.

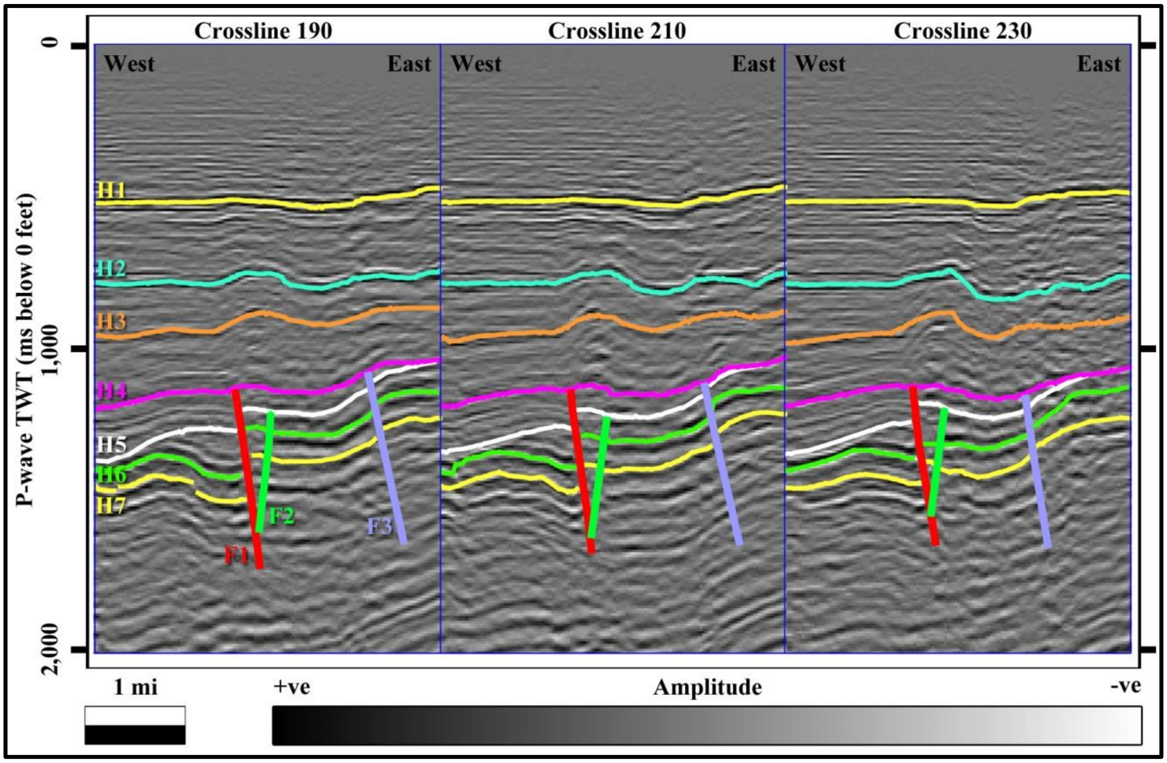

Figure 35. Structural seismic analysis of Sho-Vel-Tum field.

F1, F2, and F3 are major reverse faults that compartmentalize the field and make it structurally complex. H1 through H7 are horizons that were clear and continuous reflections throughout the survey. Producing intervals in Gant 1-19 are below H7 which have gone through diastrophic structural movements. H5 is an unconformity because it changes the depositional signature above it and terminates horizon H6 and other reflectors in the southern part of the survey. F1 reactivated to give H5 a smaller effect than deeper horizons. H4 is another unconformity that had been less affected by the faults, with only slight folding occurring in some cases. H4 does truncate the east end of the profile.

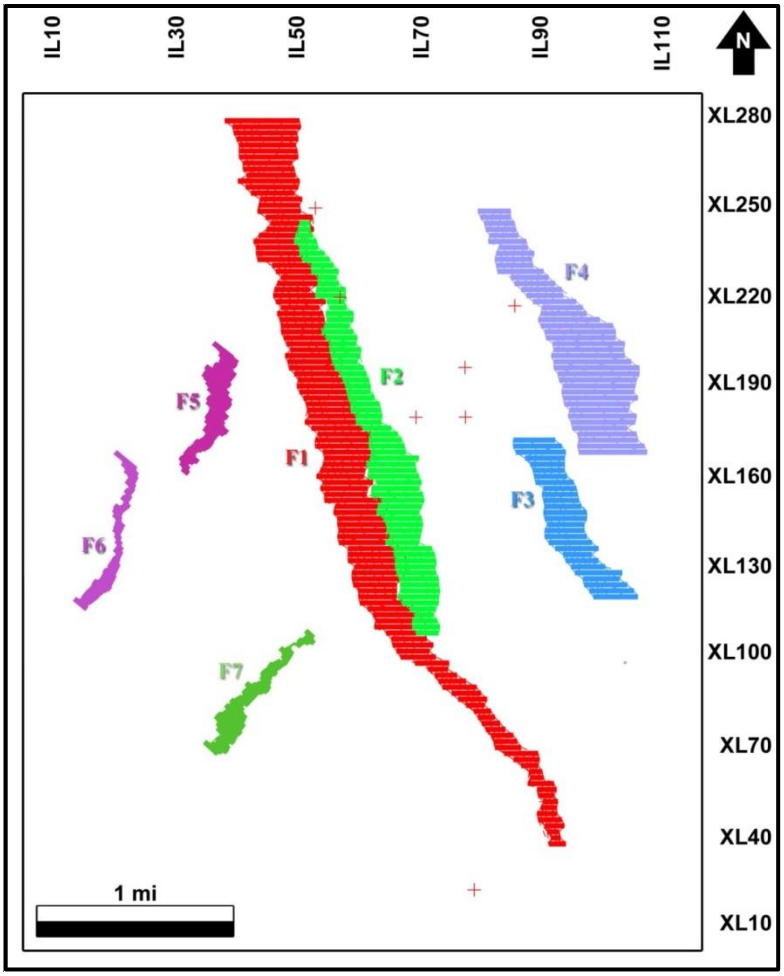

Figure 36. Fault contours in map view across the Sho-Vel-Tum field.
F1 through F7 represent faults picked on the P-P data. Due to the lower quality of the SH-SH data, F1 was the only fault to be clearly picked on both datasets.

Diastrophic tectonic movements formed the local structure and can be related to the Post-Springer Wichita Orogeny and Post-Hoxbar Arbuckle Orogeny. A major thrust fault trending NNW-SSE with a large offset can be recognized on both the P-P and SH-SH seismic volumes. This fault is believed to be caused by the post-Springer Wichita Orogeny, which was a period of extreme block faulting and folding.

Figures 35 and 36 show the interpreted reflectivity horizons and faults that compartmentalize the Sho-Vel-Tum field. Faults F1, F2, and F3 represent major reverse faults mapped through the survey. The producing formations from well Gant 1-19 are located below horizon H7. The reverse fault, F1, has the largest throw at the H6 and H7 levels. Horizon H5 represents an unconformity because of two reasons: it terminates horizon H6 and other reflectors across the southern part of the seismic survey, and a change in depositional signature can be noticed above the horizon. Horizon H5 may correlate with the Wichita Orogeny unconformity eroding parts of the Springer sands. Fault F1 seems to have reactivated and created a smaller throw on horizon H5 than the other reflectors. Later, a regional unconformity, horizon H4 erodes the upper part of the subsurface structure, which may correlate with the regional Upper Wichita Orogeny. The faults slightly affect that unconformity and create only subtle changes in structure in the shallower sections. Slight folding and faulting came later during the Arbuckle Orogeny.

DEPTH-REGISTRATION

Finally, seven depth-registered horizons were mapped across the seismic survey (Figures 37 and 38). Horizons H1 through H7 in the P-P and SH-SH seismic sections, even though they have different reflection times, were interpreted as depth-equivalent reflectors. The depth-equivalent horizons should have similar structural signatures because they represent the same subsurface reflector. However, the structural character for each reflector may not be identical in P and S image space because of lateral variations in P and S velocity profiles. Important to note in a depth-registration workflow are faults and discontinuities. These features, whether in the P-wave or the SH-wave domain, should occur at the same spatial locations assuming any lateral velocity variations are accounted for properly. Structural terminations against an unconformity, for example, were particularly valuable as tie points that enhance depth-registration accuracy.

T_S/T_P ANALYSIS

This section shows the results of the t_s/t_p analysis performed on combinations of intervals defined by horizons H1 through H4. Horizon editing was done based on a careful analysis of consecutive and redundant intervals. Three profiles in the inline direction and four profiles in the crossline direction were chosen for detailed mis-pick and horizon-stability analyses in the estimation of t_s/t_p. Then, the modifications were extrapolated to the neighboring seismic sections in the 3D volume. Figures 39 through 42 show the t_s/t_p analysis of intervals defined by horizons H1 through H4 for two of the seismic sections mentioned above. These figures are divided into two groups: pre- and post-t_s/t_p editing. P-wave time thicknesses of the analyzed intervals range from about 130 to 1,100 ms, and correspond to depth intervals of 195 to 1,650 meters with an interval velocity of 3,000 m/s. Smaller interval t_s/t_p curves are more sensitive to fine variations in P-wave and SH-wave horizon picks. Manual picking was mostly used for interpretation due to data quality issues, which is often accompanied by mis-picks in horizon mapping. The seed grid for a horizon is forced upon the horizon interpolation algorithm, which may create spikes of one or more time samples. This problem does not arise with automatic picking because an auto-pick tool follows a peak/trough/zero-crossing and will force that time sample to be chosen whether mapping from the crossline or the inline directions.

Figure 39 shows the t_s/t_p analysis over inline 14 for H1 through H4. The purpose of this analysis is to examine the lateral variations of t_s/t_p and find reliable anomalies in t_s/t_p values. All the possible interval combinations between those four intervals are plotted. Horizon "0" represents the surface of the survey. First, horizon H1 was analyzed by looking at all the intervals that include this horizon. Looking at 0 – H1 interval between crosslines 50 and 70, a decline of about 0.1 in t_s/t_p can be noticed. This exact change is mirrored in intervals H1 – H2, H1 – H3, and H1 – H4. This change is mostly noticeable in H1 – H2 because it is the smallest interval, thus more sensitive to horizon-pick variations. Moreover, it cannot be seen in the 0 – H2 interval, which strongly suggests a mis-pick in H1 horizon. Also, in the interval between crosslines 200 and 220 in interval 0 – H2, there is a gradual increase in t_s/t_p. That change might be caused by lateral variations in stratigraphy. However, a mirrored image is imposed on the other intervals that share the H2 horizon. A similar mirror effect in t_s/t_p is observed between crosslines 40 and 80 for intervals H2 – H3 and H3 – H4. In addition to these mirrored anomalies, a decrease in t_s/t_p for interval H2 – H3 is observed between crosslines 100 and 180. There appears to be no mirror effect in adjacent intervals of similar thickness – increasing my confidence in the stability of this anomaly. More fine adjustments were noted and fixed using the same approach with other horizons. The noise-like spikes in the curves correspond to the manual-picking mis-picks. The results of this analysis for crossline 14 after re-interpretation are shown in Figure 40. Anomalies in t_s/t_p interpreted on this profile should be given increased confidence over those in Figure 39. Similar interpretations and corrections are illustrated in Figures 41 and 42.

Figures 43 through 46 and Appendix Figures 50 through 59 show time structure maps of the depth-registered P-wave and SH-wave horizons. Note that the quality of horizon picking is limited by the low S/N of the eastern half (Figure 7) of the survey – the hanging wall block of the major reverse fault, F1. Appendix Figure 50 shows H1 in P-wave TWT over the seismic survey. This horizon is relatively flat, even though it appears structurally complex from the color variation. It should be noticed that the time window for that figure is small, which exaggerates the small time changes. Figure 51 represents the same horizon in SH-wave TWT. The similarity in structural signature is noticed by the depth-registered horizons. Any variations in apparent structure between those figures are thus a result of lateral variation in P-wave and SH-wave velocities (V_p/V_s). H2 and H3 time structure maps (Figures 43, 44, and Appendix Figures 52 and 53) have similar structural variation that is caused by the regional compressional regime forming the structure of Sho-Vel-Tum explained in Chapter 2. Horizon H4 (Figures 54 and 55) may correlate to the regional Upper Wichita Orogeny unconformity (as shown in Figure 34), terminating the northeastern flank of horizon H5 (Appendix Figures 56 and 57). A closer look at the seismic section would reveal a difference in structural dip of the depositional packages below and above horizon H4. Horizon H5 may correspond to the Wichita Orogeny unconformity eroding the Springer sands. It is clear that this reflector terminates the southern part of horizon H6 (Appendix Figures 58 and 59) and other reflectors. The reverse fault, F1, is clearly delineated on horizon H6 and horizon H7 (Figures 45, 46, and Appendix 58 and 59) by the sharp changes in time structure.

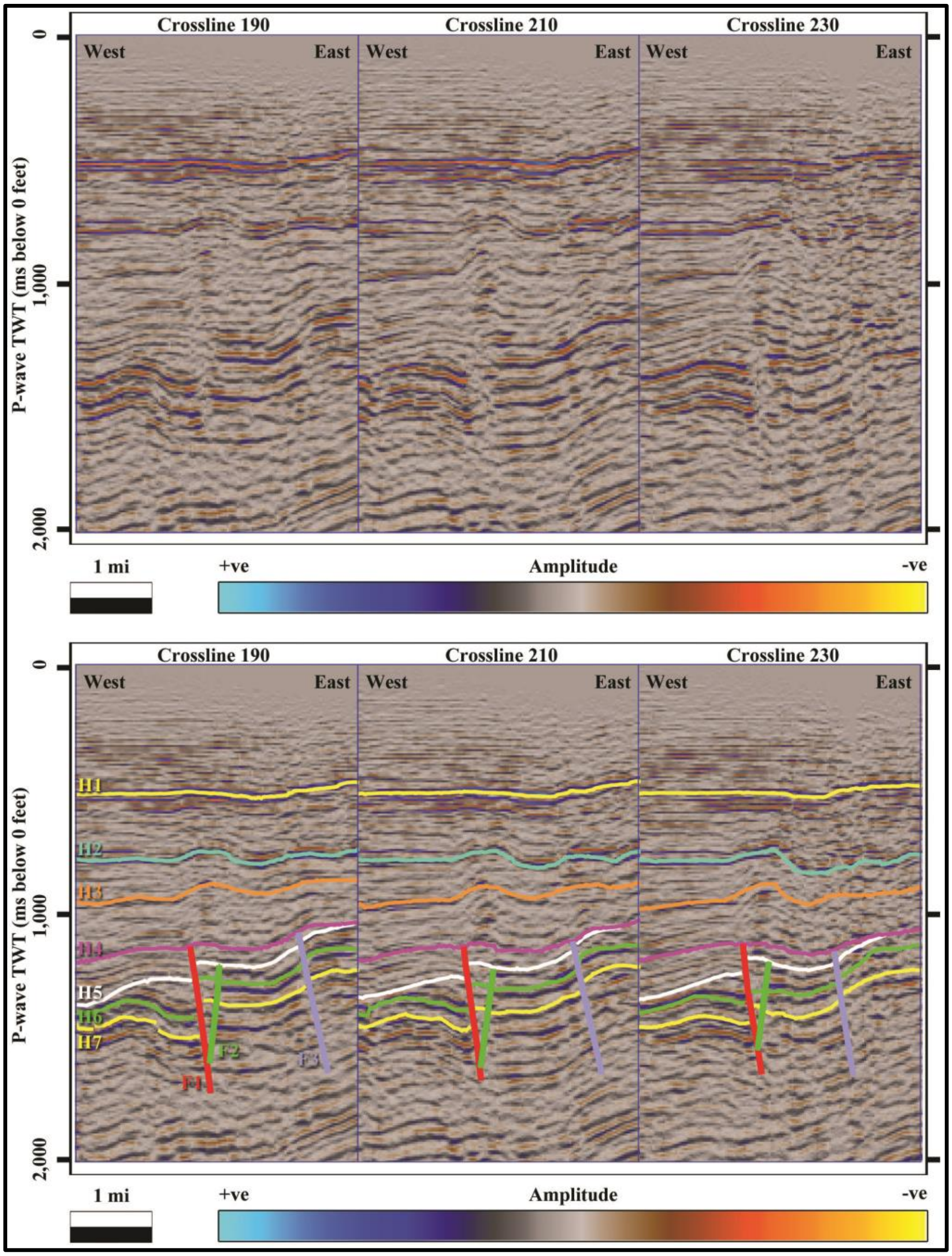

Figure 37. Interpreted horizons in the P-wave seismic data.

Fault F1 is clear on both the P-wave and SH-wave seismic sections. Horizon H5 terminates horizon H6 and other reflectors. This fork-like structure (horizons H5 and H6) on the P-P and SH-SH seismic volumes was considered a good tie-point for depth-registration.

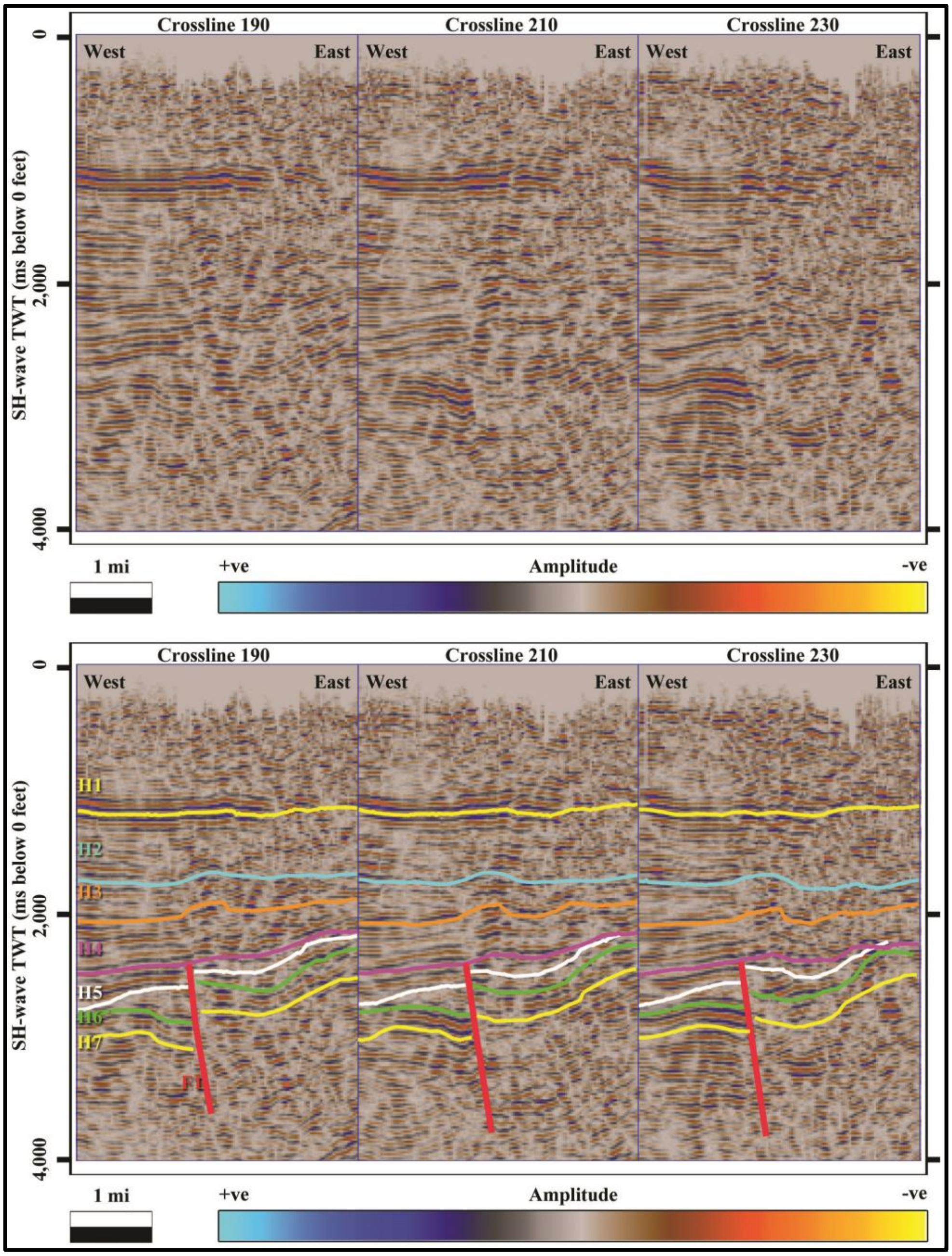

Figure 38. Interpretation of horizons on the SH-wave seismic data that are equivalent to reflections in the P-wave dataset (Figure 37).
SH-wave data quality issues on the eastern half of the seismic survey greatly affected horizon continuity, which made horizon mapping more challenging.

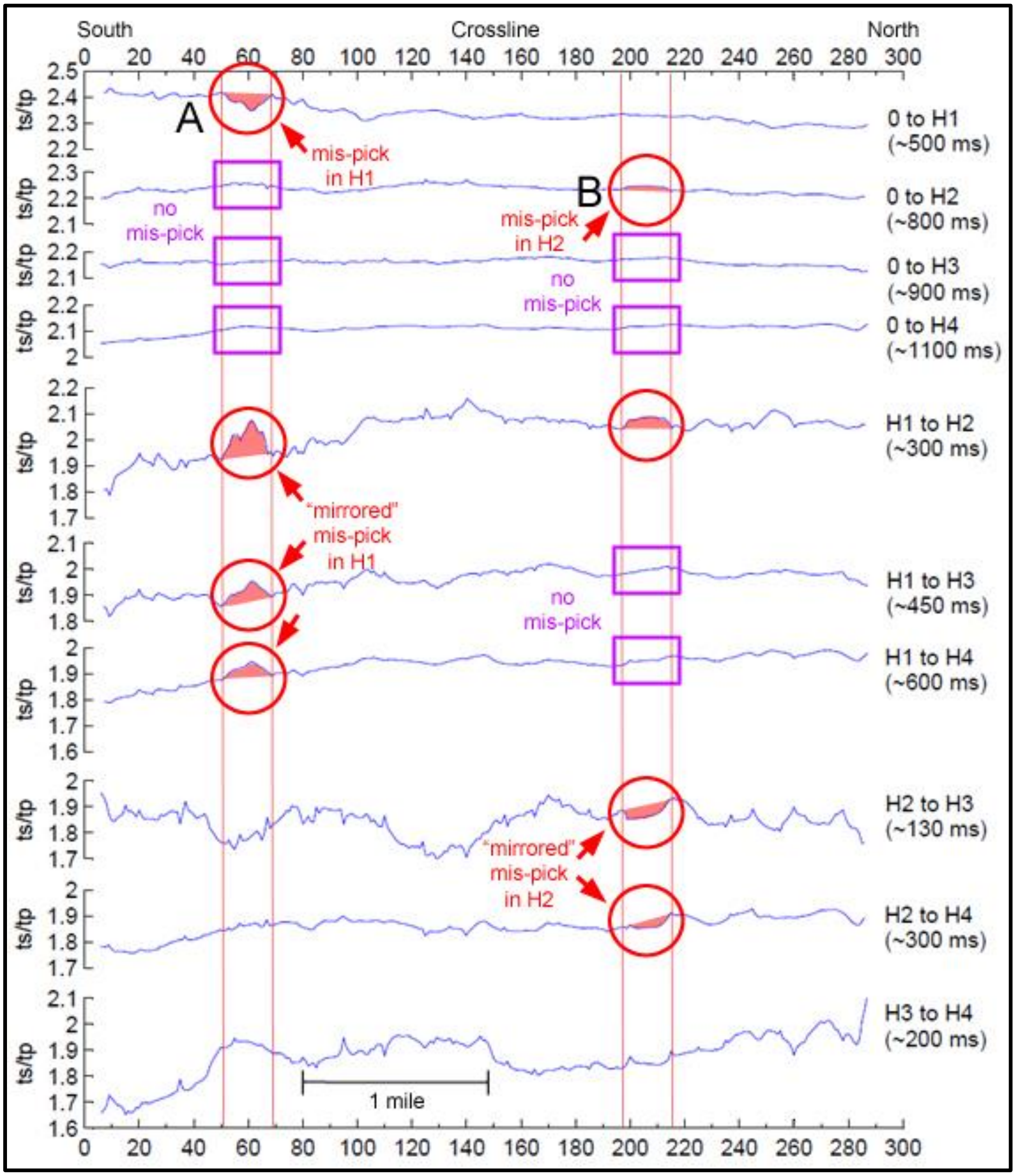

Figure 39. Inline 14 t_s/t_p in seismic intervals prior to editing based on consistency of interpreted values (H1 through H4).

A variation in t_s/t_p (A) is visible in interval 0 – H1 between crosslines 50 and 70, and it is mirrored in intervals H1 – H2, H1 – H3, and H1 – H4 (red circles). It does not show on other intervals (magenta boxes). These observations suggest the reason is a mis-pick in horizon H1.

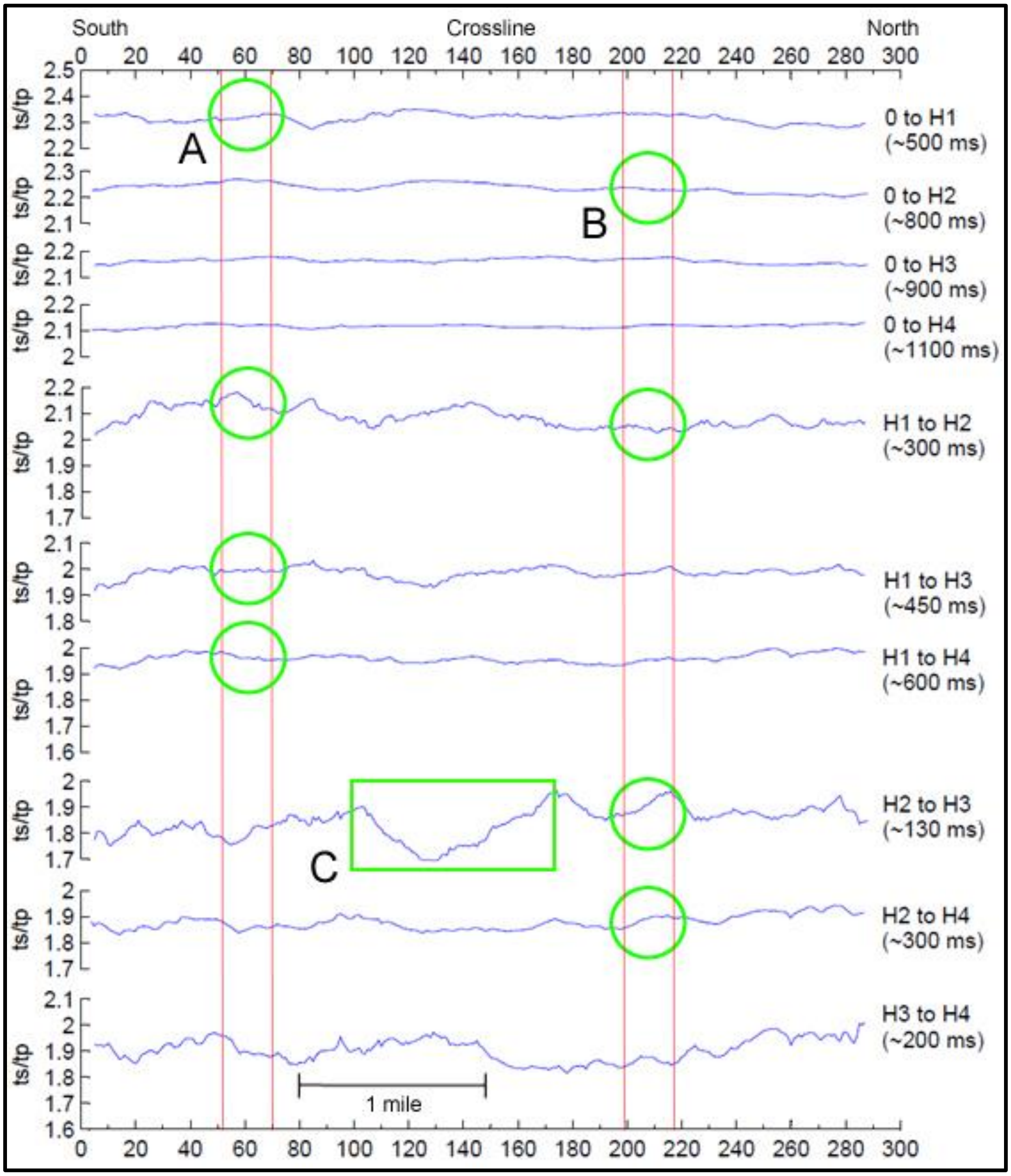

Figure 40. Inline 14 t_s/t_p in seismic intervals after editing mis-picks on a relatively fine scale (H1 through H4).

The locations of the two mis-picks A and B in Figure 39 are shown (green circles). A decrease in t_s/t_p for interval H2 – H3 (green box) does not show mirrored images on adjacent intervals. This increases my confidence in the stability of this anomaly.

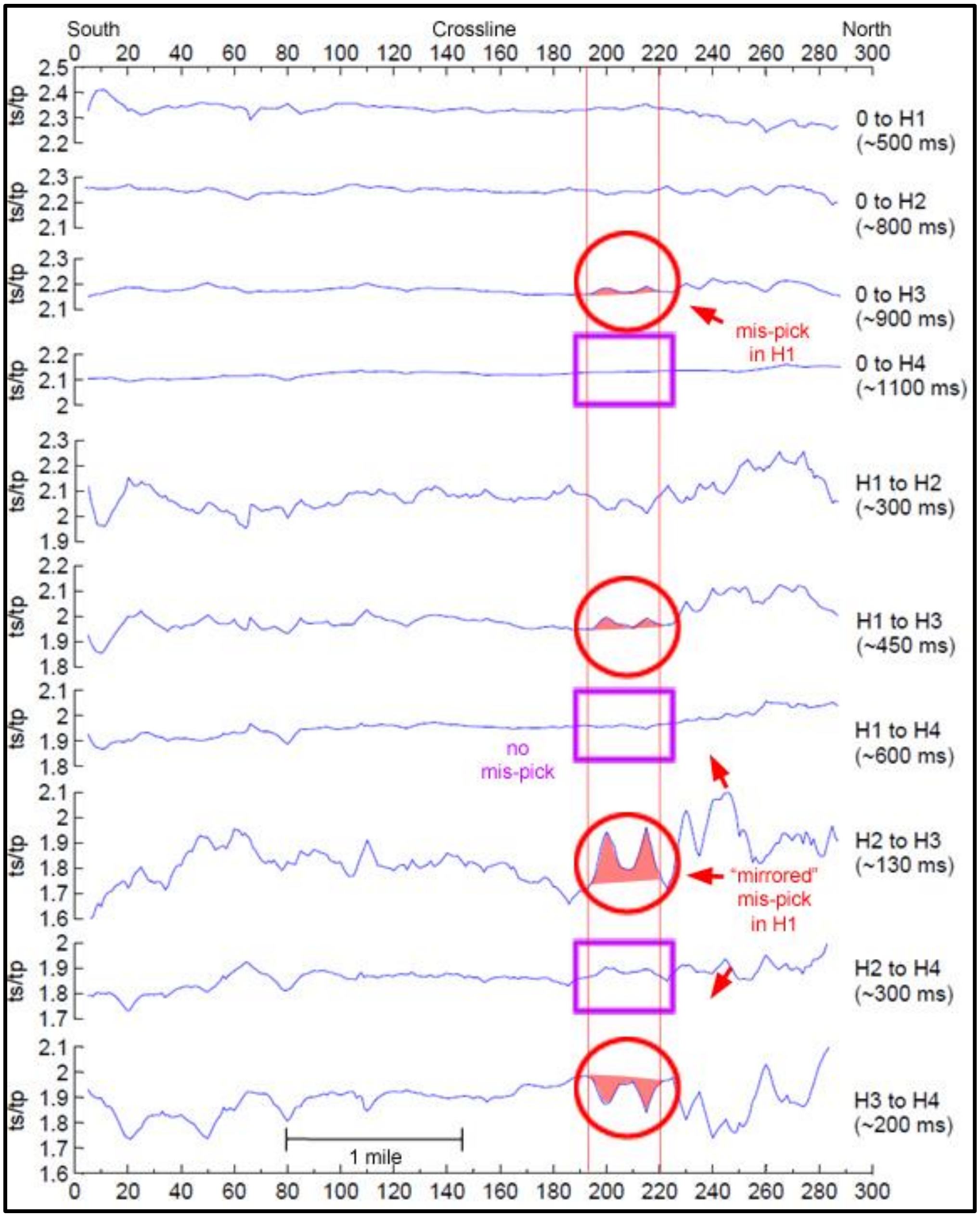

Figure 41. Inline 39 t_s/t_p in seismic intervals prior to editing based on consistency of interpreted values (H1 through H4).

A variation in t_s/t_p is visible in intervals 0 – H3, H1 – H3, H2 – H3, and it is mirrored in interval H3 – H4 (red circles). It does not show on other intervals (magenta boxes). These observations suggest the reason is a mis-pick in horizon H3.

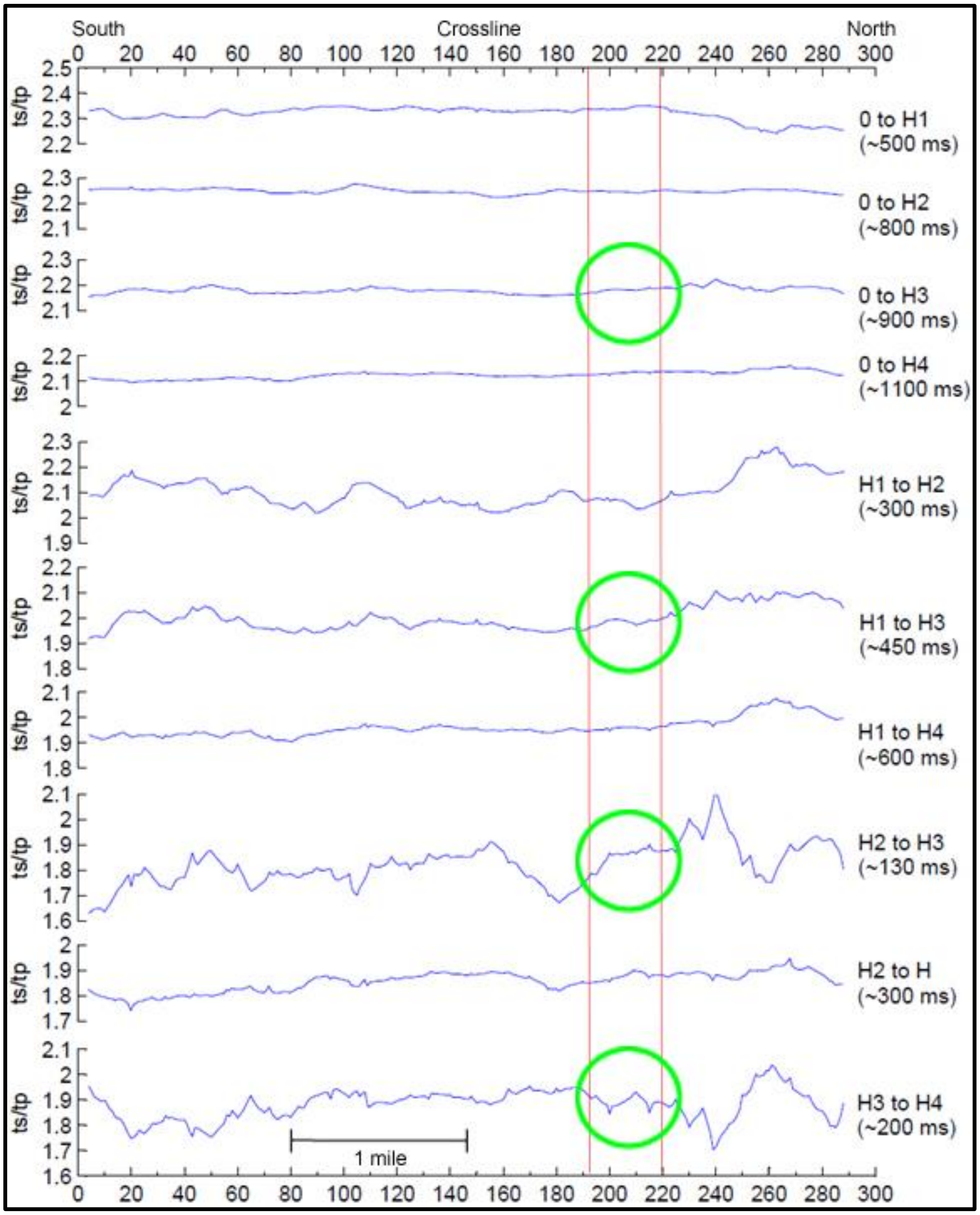

Figure 42. Inline 39 t_s/t_p in seismic intervals after editing mis-picks on a relatively fine scale (H1 through H4).
The location of the mis-pick highlighted in Figure 41 is shown (green circles). This variation was not an actual lateral stratigraphic anomaly.

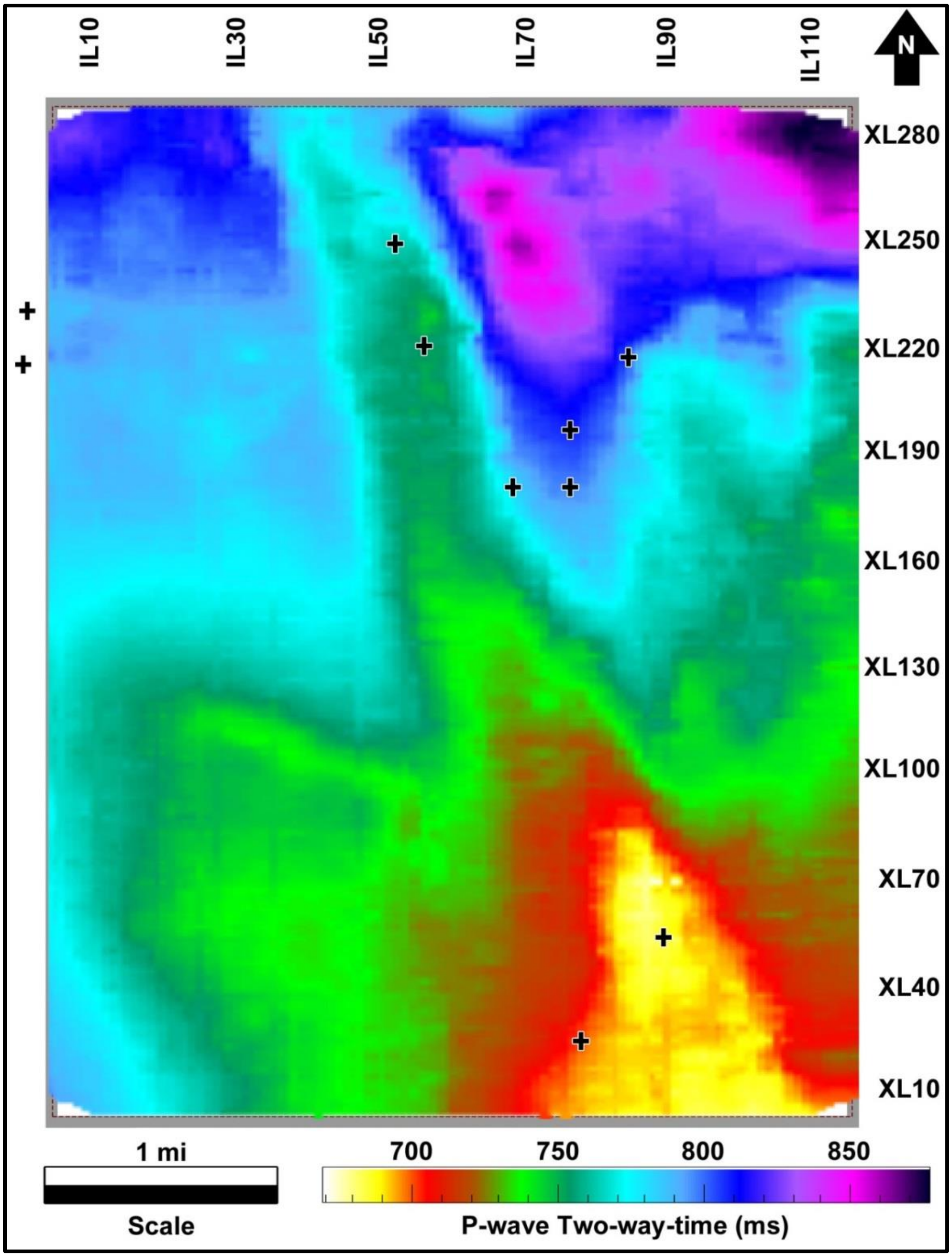

Figure 43. Time structure map for H2 in P-wave TWT.

Slight folding is due to the Arbuckle Orogeny. Structural variations are exaggerated because of the small time window.

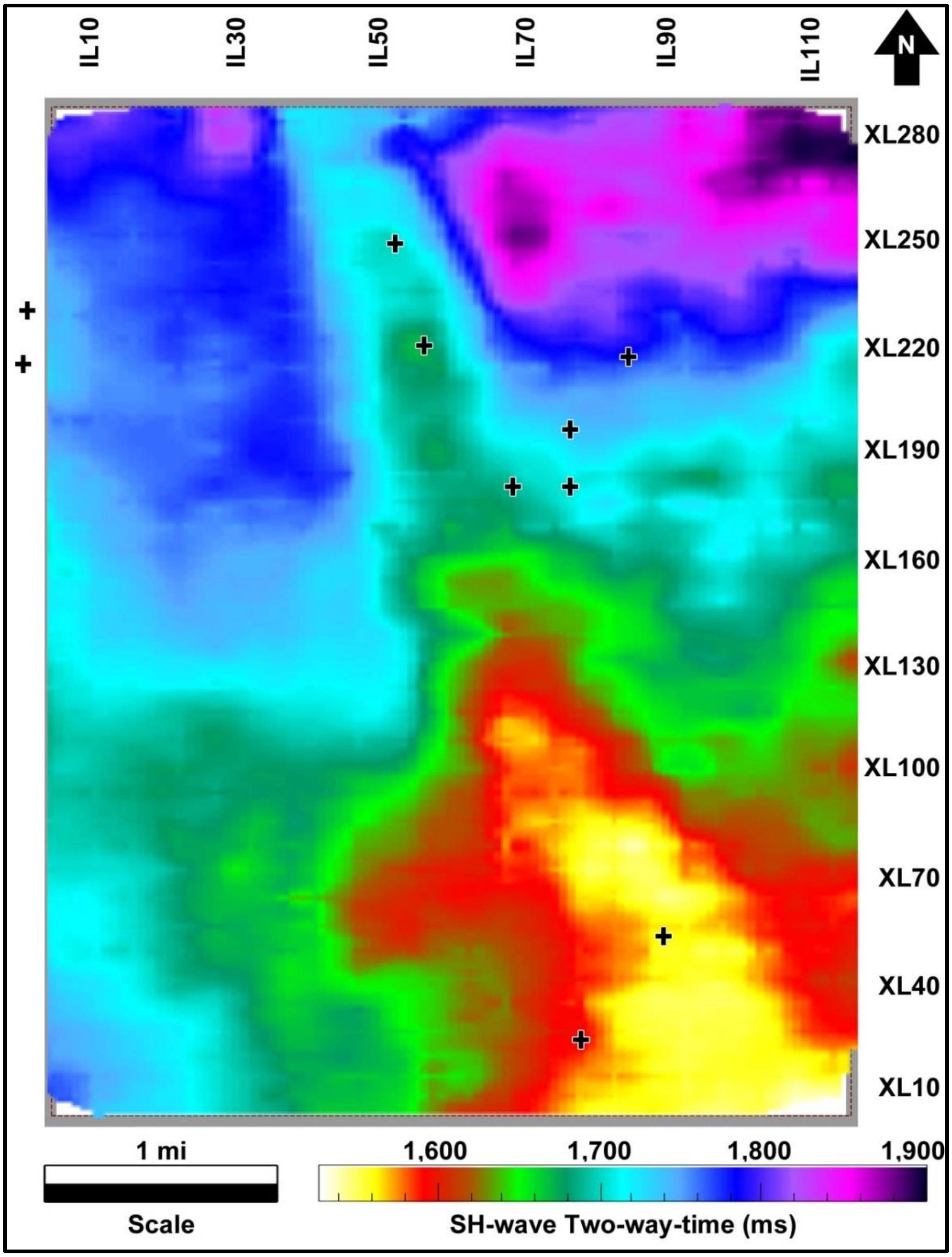

Figure 44. Time structure map for H2 in SH-wave TWT.
Note the structural similarity with the corresponding horizon (H2) in the P-wave TWT shown in Figure 43.

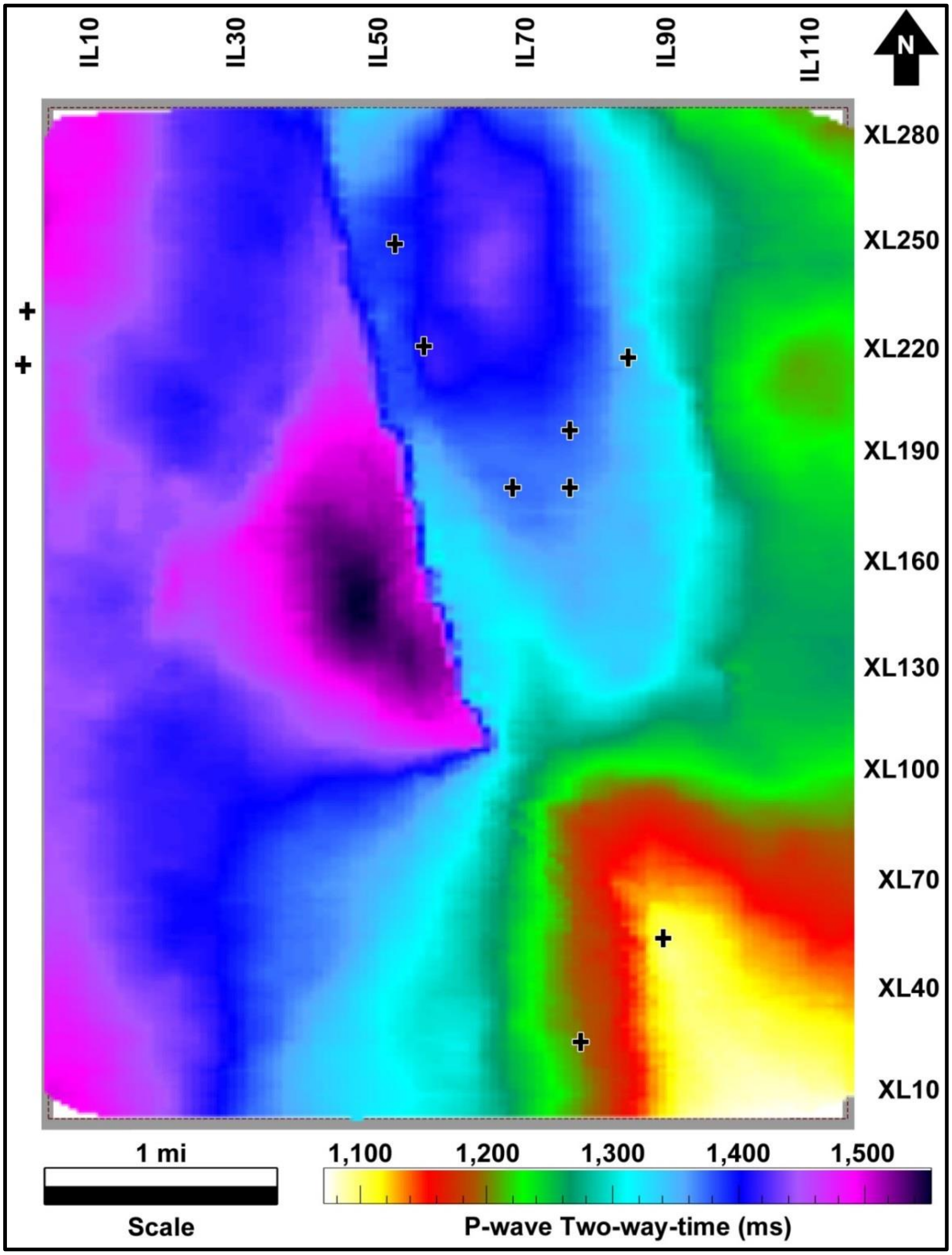

Figure 45. Time structure map for H7 in P-wave TWT.

The structure is affected by the Wichita and Arbuckle orogenies at this depth resulting in extensive folding and faulting.

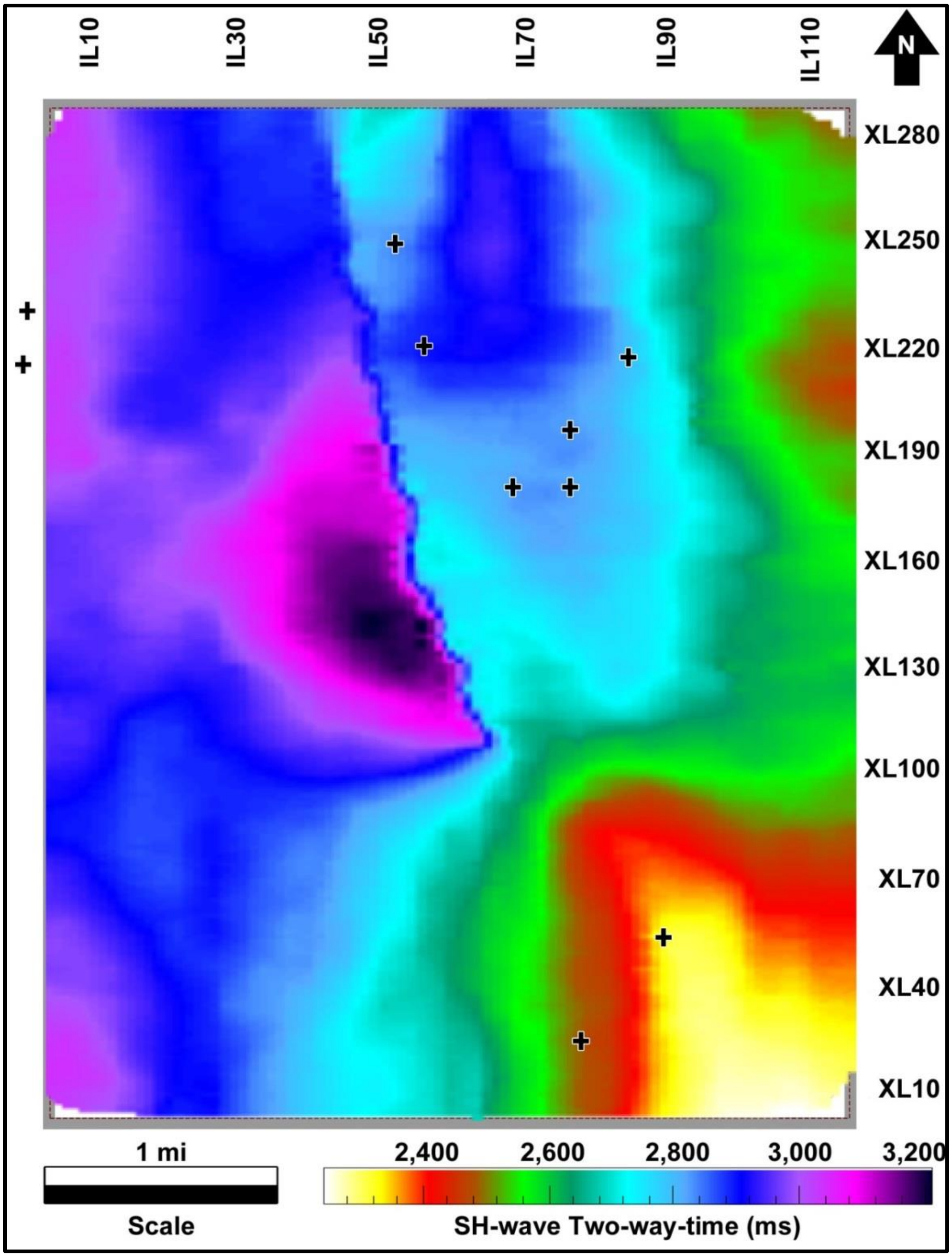

Figure 46. Time structure map for H7 in SH-wave TWT.
Note the structural similarity with the corresponding horizon (H2) in the P-wave TWT shown in Figure 45.

Figures 47, 48, and Appendix Figures 60 and 61 show the interval V_p/V_s maps (t_s/t_p) for the consecutive intervals of horizons H1 through H4. High V_p/V_s values (about 2.30) were observed for 0 – H1. That is because shallow sections have low shear-wave velocities, which causes high average V_p/V_s. Interval V_p/V_s of H2 – H3 shows a significant increase in value in one part of the survey. As shown Figure 34, this stratigraphic interval includes Hefner formation, which is an oil producing formation. There may be a correlation with the location of the oil-producing wells (marked by + signs). These wells produce from shallow formations which might be located in the deeper section within H1 – H2 or the shallow section of H2 – H3 as in Figure 34. However, without velocity data and accurate well-seismic ties, detailed reservoir characterization is only wishful thinking. Still, these figures can be significantly important given the limited amount of data available for this field. Final results with depth-equivalent horizons mapped on P-P and SH-SH seismic data are shown in Figure 49.

Time structure maps show similar structural signature from gentle to extreme folding and faulting. Deeper horizons were more difficult to pick, especially on the SH-wave data due to the horizon discontinuity. When tracing a horizon through a discontinuity in the SH-wave seismic section, the decision of whether to follow the shallower or deeper reflection is usually guided by its P-wave equivalent horizon. This may have introduced some bias in the SH-wave picks. These points where bias may be unintentionally imposed on the SH-picks were noticed and fixed during the t_s/t_p analysis.

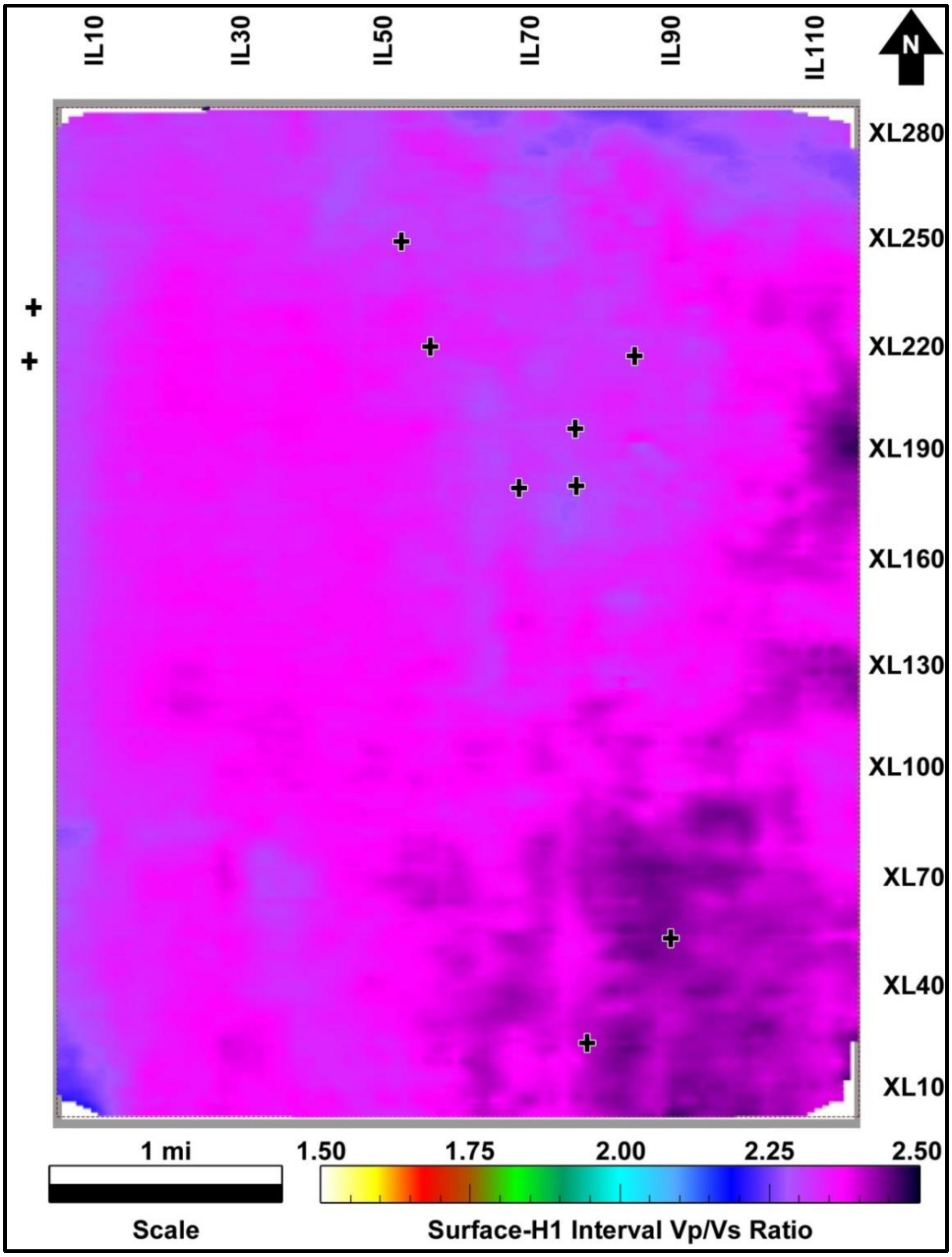

Figure 47. V_p/V_s in the interval between the surface and horizon H1.

The high average values in V_p/V_s correspond to the low-velocity near-surface layer. Near-surface rocks often have low S-wave velocity, resulting high V_p/V_s.

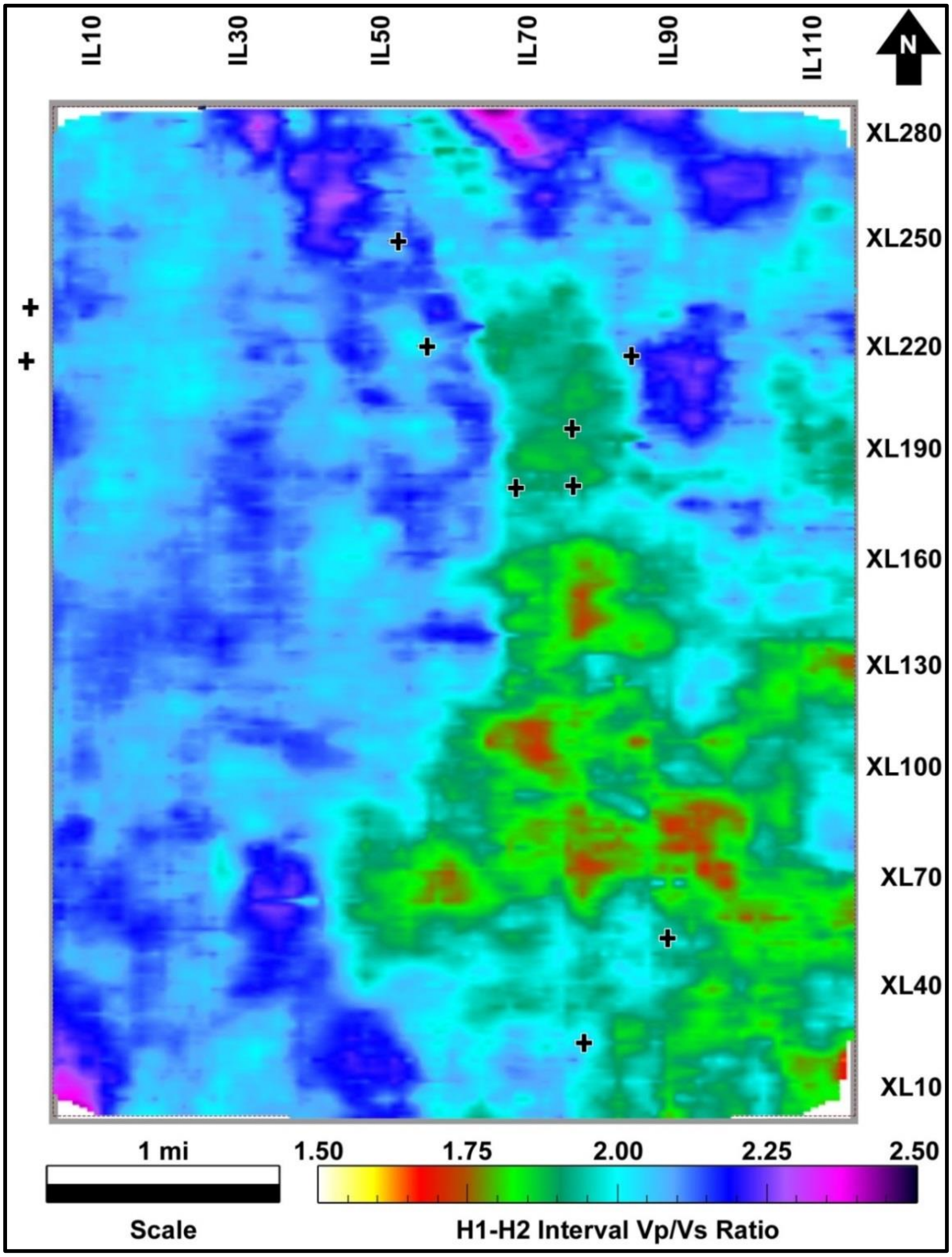

Figure 48. V_p/V_s in the interval between horizons H1 and H2.
The lower values of V_p/V_s close to the well locations on the eastern side may correspond to the producing limestone formations at the base of H1 – H2 interval.

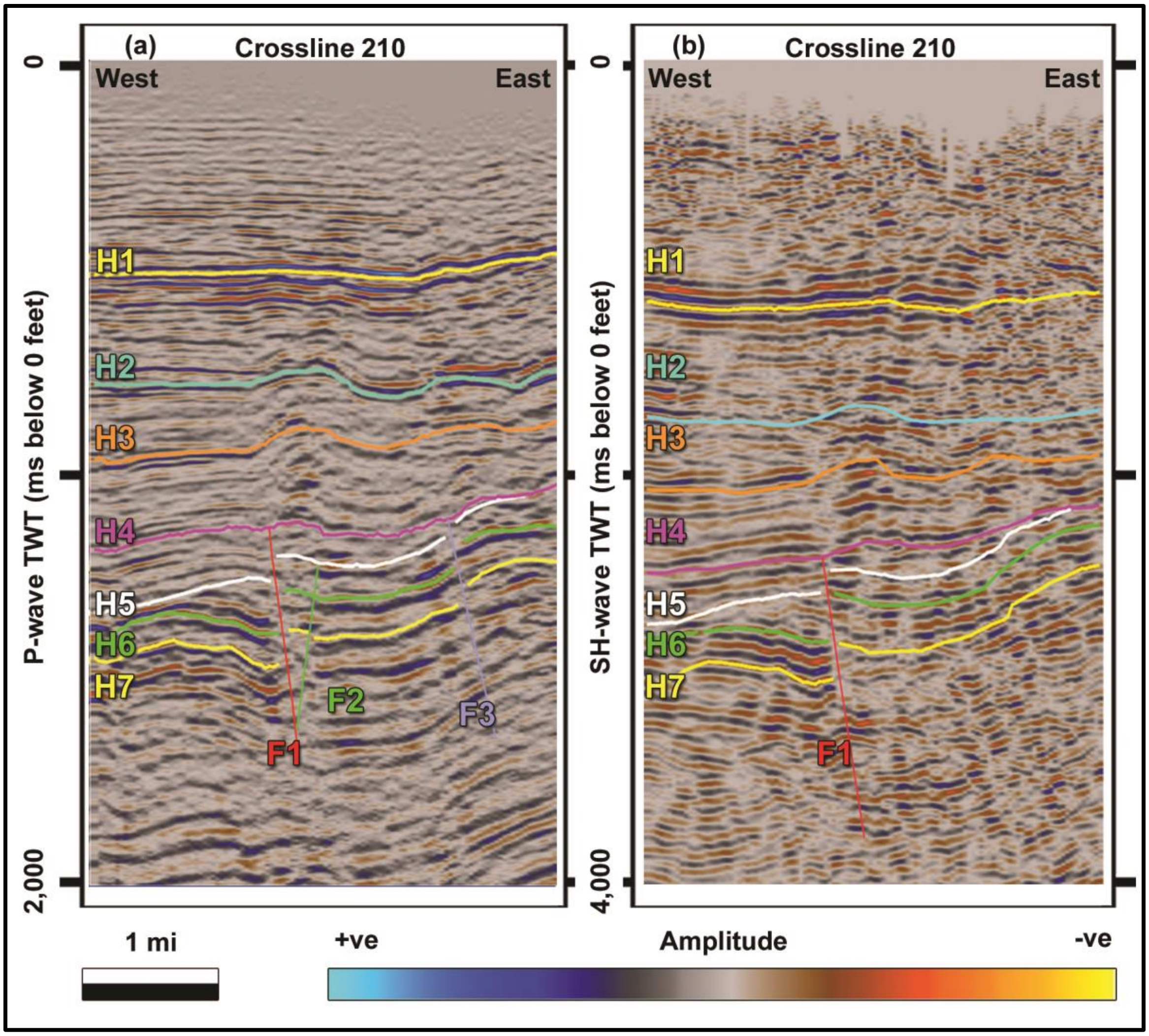

Figure 49. Depth-registered horizons on (a) the P-P and (b) SH-SH seismic data. The interpreted horizons on both seismic data volumes are shown. Faults F2 and F3 were not mapped on the SH-wave data due to data quality issues. Constraining the interpretations with V_p/V_s values increased the confidence in the quality of the registration workflow.

Chapter 5: Conclusions

Registration (correlation) of compressional-wave and shear-wave seismic data can be achieved based on interpreter's judgment even when velocity data are not available. Horizon interpretation and depth-registration of P-wave and S-wave data are interdependent, which means these analysis techniques may be iterated to optimize the results. The P-P wave synthetic seismograms tied reflectors and geologic formations. Synthetic seismograms were created using density logs and the Wiener-Levinson mixed-phase wavelet method, and were produced with and without AGC. The AGC operator did not always improve the correlation coefficient between the synthetic P-wave seismic trace and a near-by stacked trace.

The depth-equivalent horizons should have similar structural signatures because they represent the same subsurface reflector. However, the structural character for each reflector will not be identical in P and S image space because of lateral variations in P and S velocity profiles. Faults and discontinuities, whether in the P-wave or the SH-wave domain, should occur at the same spatial locations assuming any lateral velocity variations are accounted for properly. Structural terminations against an unconformity were particularly valuable as tie points that enhance depth-registration accuracy.

Several seismic profiles were chosen for detailed mis-pick and horizon-stability analyses in the estimation of t_s/t_p. Horizon editing was done based on a careful analysis of consecutive and redundant intervals. The adjustments were then extrapolated to the neighboring seismic sections in the 3D volume. Anomalies in t_s/t_p interpreted on the seismic profile after this analysis should be given increased confidence over those prior to editing based on consistency of interpreted values.

However, without velocity data and accurate well-seismic ties, detailed reservoir characterization is only wishful thinking. Still, these figures can be significantly important given the limited amount of data available for this field.

There is, of course, uncertainty in picking depth-equivalent horizons. But overall, such a seismic interpretation exercise is possible to translate sparse geological information into a plausible seismic interpretation.

LIMITATIONS

The major limitation of this work was the lack of velocity data, which created significant barriers when trying to directly tie geological information to geophysical data. Also, the lack of well control below 2,000 ms of P-wave TWT (and 4,000 ms of SH-wave TWT) made it difficult to work with seismic data below the depth corresponding to those image time coordinates.

FUTURE RESEARCH

This type of study is only the first step in utilizing the full potential of multicomponent seismic analysis. With more velocity data (mono- and dipole sonic logs, VSPs, and velocity surveys), multicomponent attribute analysis in depth-equivalent intervals can have a significant impact on reservoir characterization. A structurally-complex compartmentalized oil field usually has unexplored blocks containing bypassed hydrocarbons. The Sho-Vel-Tum field has been producing since the early 20th century. However, it is only recently that deeper reservoirs started producing. This fact should be enough motivation to acquire more velocity data to execute improved P and S data analyses.

Appendix

Table 7. Well codes and locations.

UWI	Lease Name	Well #	Location
35137084540000	Baker-B	3	1N 4W 19 E2SESWNE
35137084640000	Baker B	2	1N 4W 19 SW SW NE
35137088710000	Hitchcock-A	2	1N 4W 18 SW SW NE
35137089230000	Burns	3	1N 5W 13 NE NE NE
35137092200000	Baker \`A\`	1	1N 4W 18 NW SE NW
35137094450000	Chem-Doyle	1	1N 4W 19 NW NW NE
35137095030000	Burns Mattie Bell	4	1N 5W 13 NW
35137095810000	Burns Mattie	2	1N 5W 13 NW NE SE
35137134080000	Hitchcock \`A\`	1	1N 4W 18 NW SW NE
35137134130000	Harry \`A\`	1	1N 4W 18 NW NW NW
35137134770000	Baker \`B\`	1	1N 4W 19 NW SW NE
35137227130000	Wade	1	1N 4W 20 SE SE SW
35137229590000	Wade	2	1N 4W 20 SE NE SW
35137231280000	Wade	4	1N 4W 20 SE SW SW
35137231920000	Wade	3	1N 4W 20 NE
35137238380000	Mary Sands Unit	1A	1S 4W 5 NE SE NW
35137252720000	Ringer	1-32H	1N 4W 32 W2 SE SE
35137253230000	Pollard	1	1N 5W 24 NW
35137253460000	Sea Properties	1	1N 5W 24 SW NW NW
35137255190000	Gant	1-19	1N 4W 19 NW SE NE
35137256780000	Vera	1-18	1N 4W 18 SE SW SE

Table 8. Well info and status.

Lease Name	Well No.	Final Status	Driller Td	Hole Direction	Elev Code	Ref Elev
Baker-B	3	Oil	6,812	Vertical	KB	1,063
Baker B	2	Oil	8,210	Vertical	DF	1,079
Hitchcock-A	2	Oil	7,013	Vertical	DF	1,079
Burns	3	Oil	7,890	Vertical	DF	1,118
Baker \`A\`	1	Oil	8,165	Vertical	KB	1,085
Chem-Doyle	1	Oil	8,712	Vertical	KB	1,082
Burns Mattie Bell	4	Oil	6,698	Vertical	KB	1,133
Burns Mattie	2	Oil	8,325	Vertical	GR	1,140
Hitchcock \`A\`	1	Oil	8,530	Vertical	GR	1,062
Harry \`A\`	1	Oil	8,560	Vertical	KB	1,114
Baker \`B\`	1	Oil	8,513	Vertical	DF	1,072
Wade	1	Oil	6,150	Vertical	KB	1,020
Wade	2	Oil	6,250	Vertical	KB	1,034
Wade	4	Oil	6,421	Vertical	KB	1,044
Wade	3	Oil	6,086	Vertical	KB	1,010
Mary Sands Unit	1A	Oil	5,834	Vertical	DF	1,098
Ringer	1-32H	Oil	13,016	Horizontal	KB	1,047
Pollard	1	Oil	8,830	Vertical	KB	1,108
Sea Properties	1	Oil	9,045	Directional	KB	1,150
Gant	1-19	Oil	13,221	Directional	KB	1,067
Vera	1-18	Gas	6,300	Vertical	KB	1,071

Table 9. Well producing formations.

Lease Name	Well No.	Field Name *	Ip Prod Form Name	Form At TD Name
Baker-B	3	Doyle	Markham	Unknown
Baker B	2	Doyle	Markham	Sims
Hitchcock-A	2	Sho-Vel-Tum	Markham	Humphreys
Burns	3	Sho-Vel-Tum	Old Woman	Sims Lower
Baker `A`	1	Doyle East	Springer	Unknown
Chem-Doyle	1	Sho-Vel-Tum	Markham	Unknown
Burns Mattie Bell	4	Sho-Vel-Tum	Hefner	Unknown
Burns Mattie	2	Sho-Vel-Tum	Hefner	Unknown
Hitchcock `A`	1	Sho-Vel-Tum	Markham	Caney
Harry `A`	1	Sho-Vel-Tum	Aldridge Upper	Unknown
Baker `B`	1	Sho-Vel-Tum	Markham	Sims Lower
Wade	1	Sho-Vel-Tum	Tussy	Pennsylvanian
Wade	2	Sho-Vel-Tum	Tussy	Hefner
Wade	4	Sho-Vel-Tum	Tussy	Pennsylvanian
Wade	3	Sho-Vel-Tum	Tussy	Hefner
Mary Sands Unit	1A	Sho-Vel-Tum	Aldridge	Pennsylvanian
Ringer	1-32H	Sho-Vel-Tum	Sycamore	Mississippian
Pollard	1	Sho-Vel-Tum	Sims	Sims
Sea Properties	1	Sho-Vel-Tum	Humphreys	Sims
Gant	1-19	Sho-Vel-Tum	Sycamore	Ordovician
Vera	1-18	Sho-Vel-Tum	Culberson	Tussy Lower

Table 10. Formation tops for wells within the area of interest.

Well	Pick	Depth (ft)	Well	Pick	Depth (ft)
Wade 1	Pennsylvanian Upper	0	Pollard 1	Dornich Hills Upper	7,297
	Hoxbar Oolitic	3,472		Markham	7,378
	Culberson	4,775		Aldridge	7,570
	Fusulinid Lm	5,140		Humphreys	8,100
	Tussy	5,450		Sims	8,438
	Hefner	5,910	Sea Properties 1	Hoxbar	3,137
Wade 2	Permian Lm	0		Doyle /Des Moines	3,691
	Hoxbar Oolitic	3,573		Willie	4,358
	Culberson	4,887		Hoxbar	5,114
	Tussy	5,613		Deese	5,269
	Hefner	5,930		Culberson	5,606
Wade 4	Permian Lower	3,490		Fusulinid Desmoines	6,054
	Culberson	4,860		Tussy	6,434
	Fusulinid Desmoines	5,256		Hefner	7,038
	Tussy	5,600		Dornich Hills Upper	7,418
	Hefner	5,926		Markham	7,578
Wade 3	Hoxbar Oolitic	3,478		Aldridge	7,808
	Culberson	4,642		Humphreys	8,193
	Fusilina	5,076		Sims	8,552
	Tussy	5,540	Gant 1-19	False Caney	9,870
	Hefner	5,806		Caney	10,100
Ringer 1-32h	Springer	5,310		Sycamore	10,329
	Humphreys	5,488		Woodford	10,718
	Sims	5,844		Hunton	11,088
	Caney	8,030		Sylvan	11,575
	Caney	8,246		Viola	11,819
	Sycamore	8,448		Bromide 1	12,629
Pollard 1	Doyle 1	3,623		Tulip Creek	13,003
	Doyle 2	3,938	Vera 1-18	Doyle 1	2,227
	Willie	4,291		Doyle 2	2,667
	Hoxbar Oolitic	4,988		Willie	2,938
	Culberson	5,499		Hoxbar Oolitic	3,493
	Fusulinid Desmoines	5,958		Culberson	3,840
	Carpenter 1	6,823		Fusulinid Desmoines	4,110
	Hefner	6,879		Tussy Lower	4,755

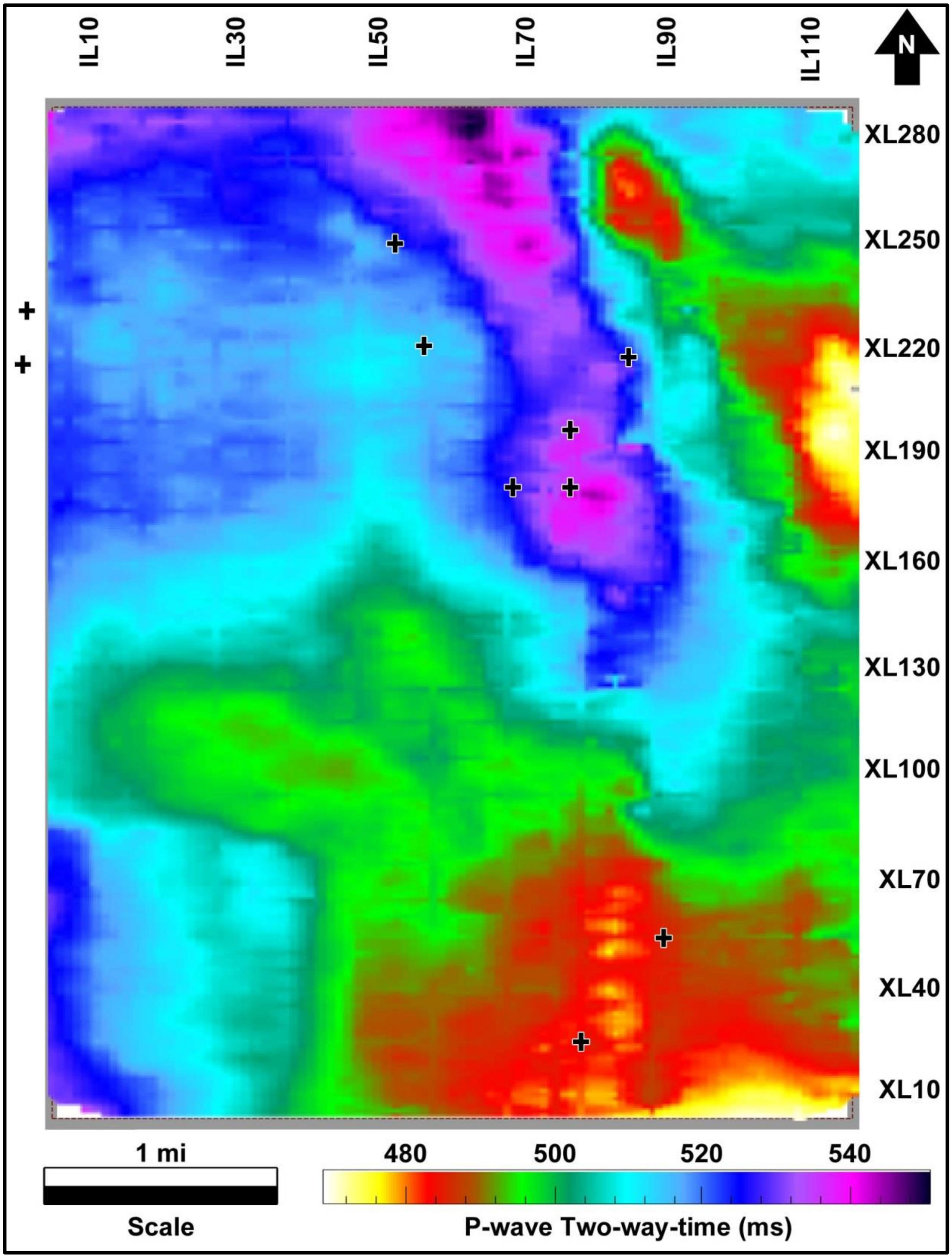

Figure 50. Time structure map for H1 in P-wave TWT.

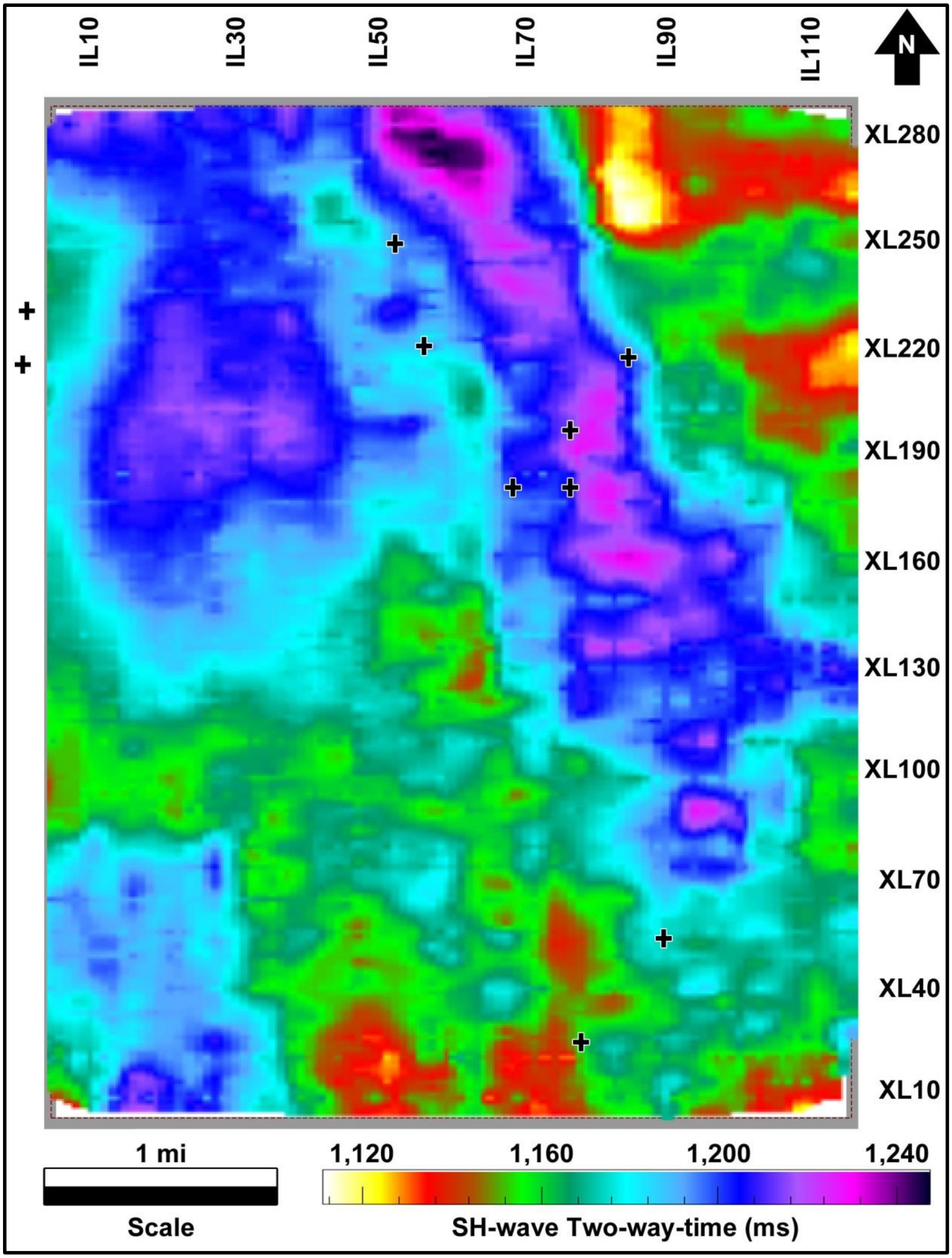

Figure 51. Time structure map for H1 in SH-wave TWT.

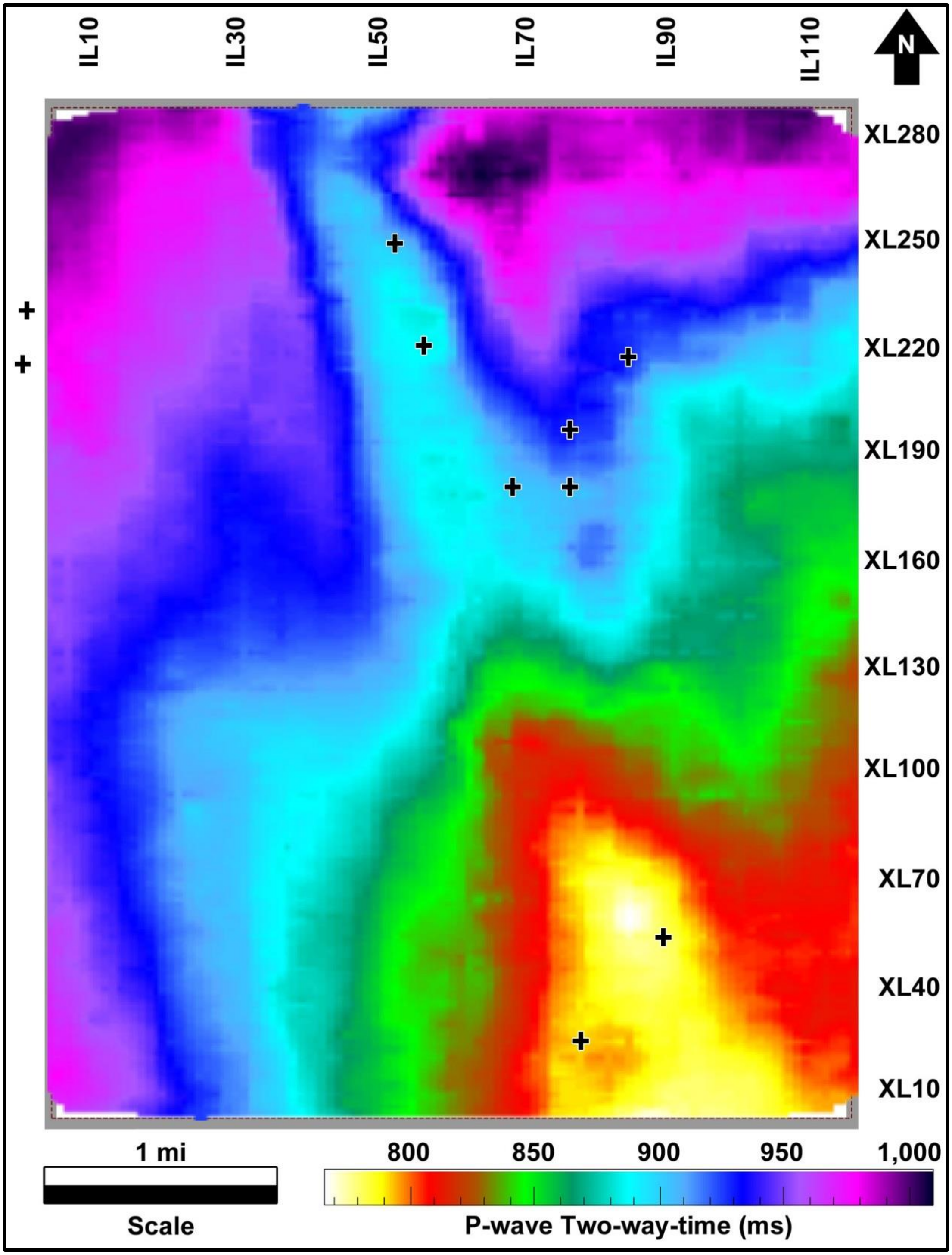

Figure 52. Time structure map for H3 in P-wave TWT.

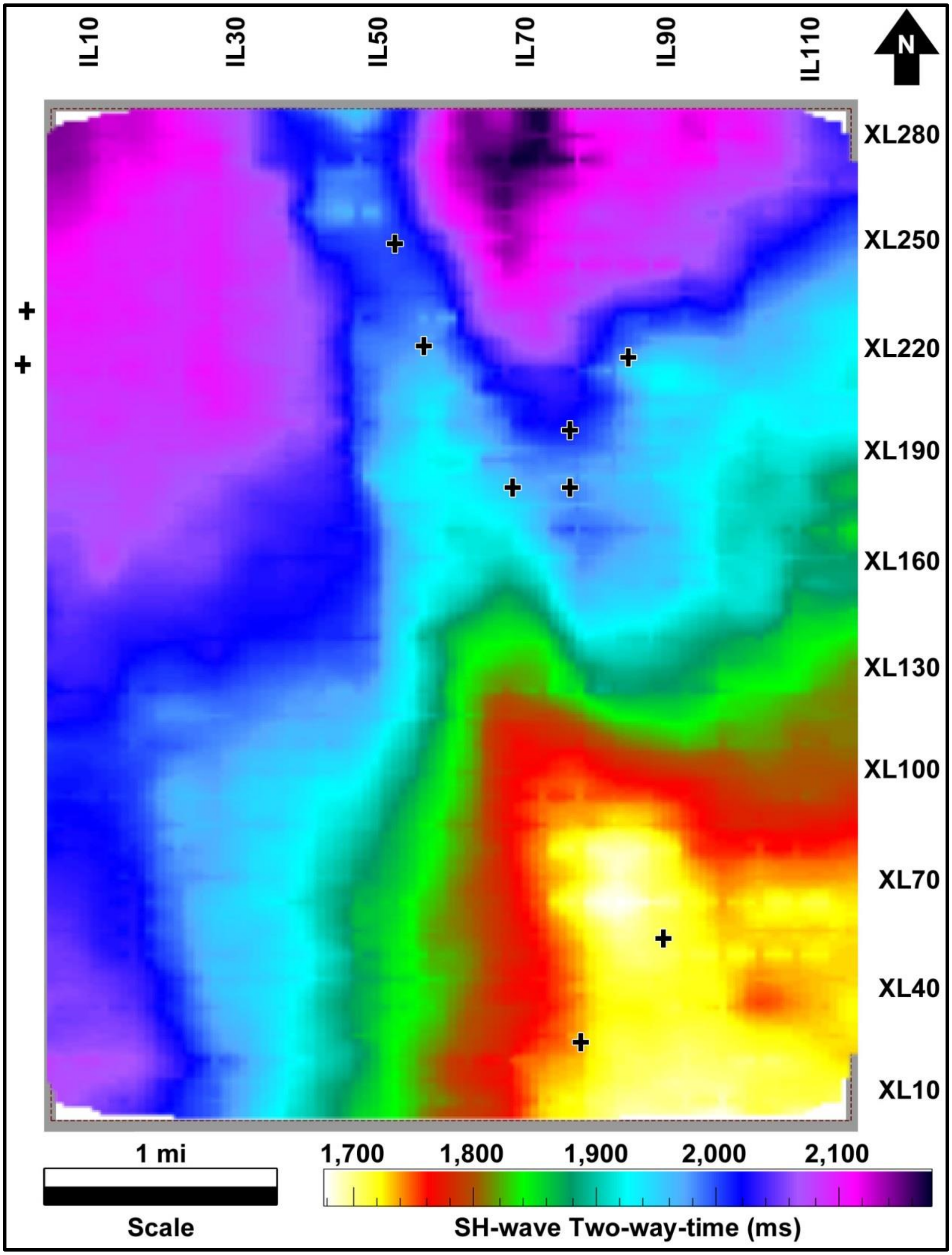

Figure 53. Time structure map for H3 in SH-wave TWT.

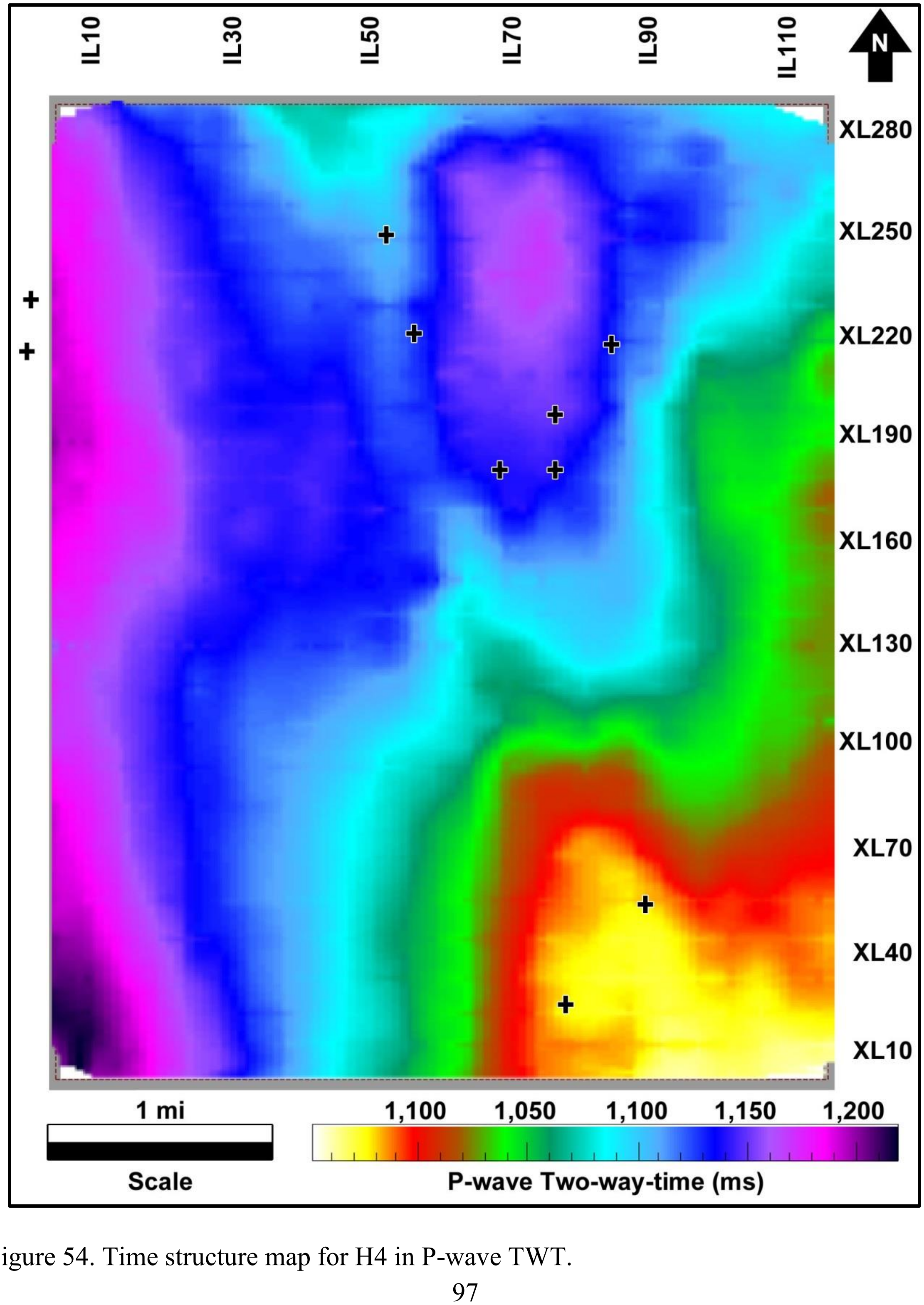

Figure 54. Time structure map for H4 in P-wave TWT.

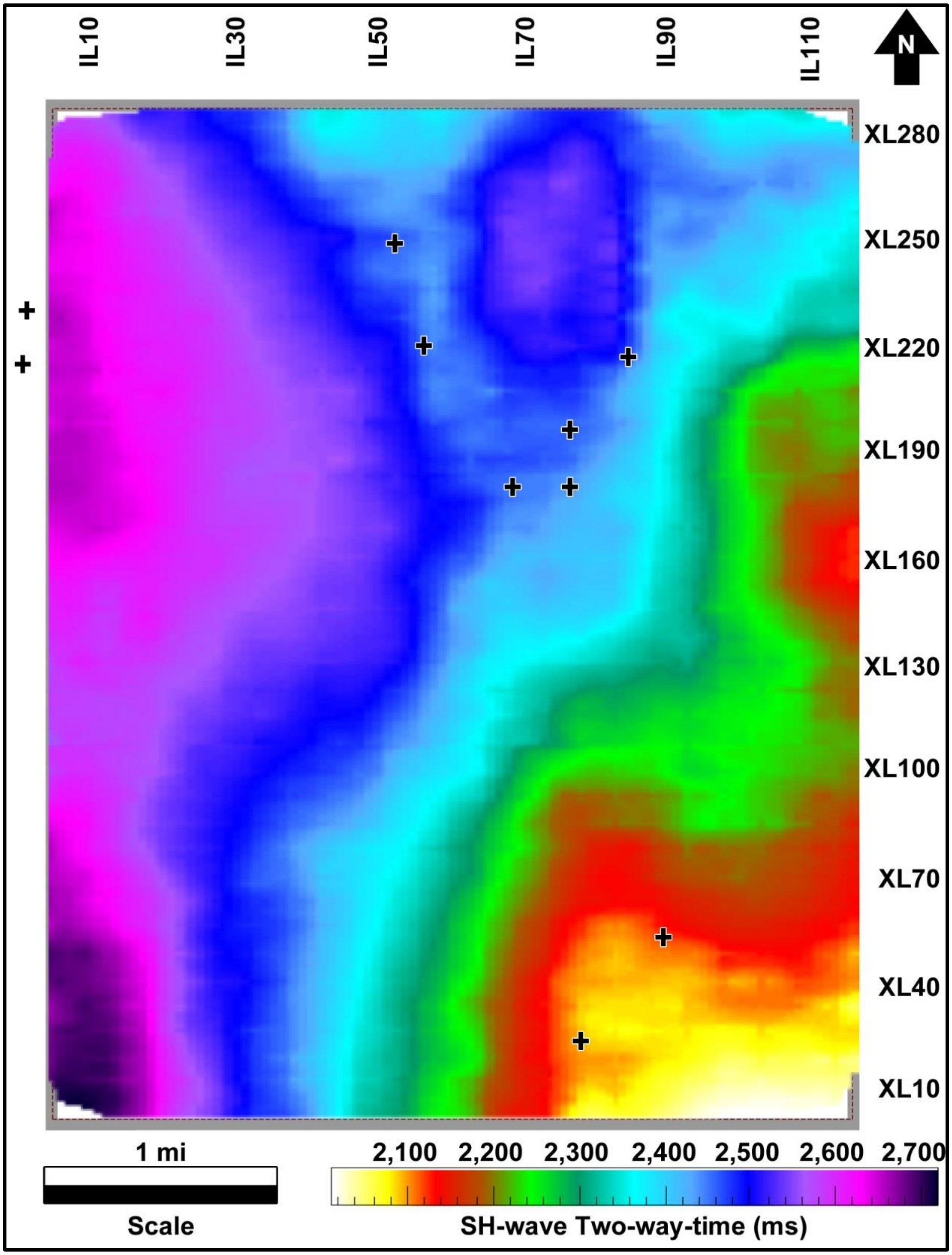

Figure 55. Time structure map for H4 in SH-wave TWT.

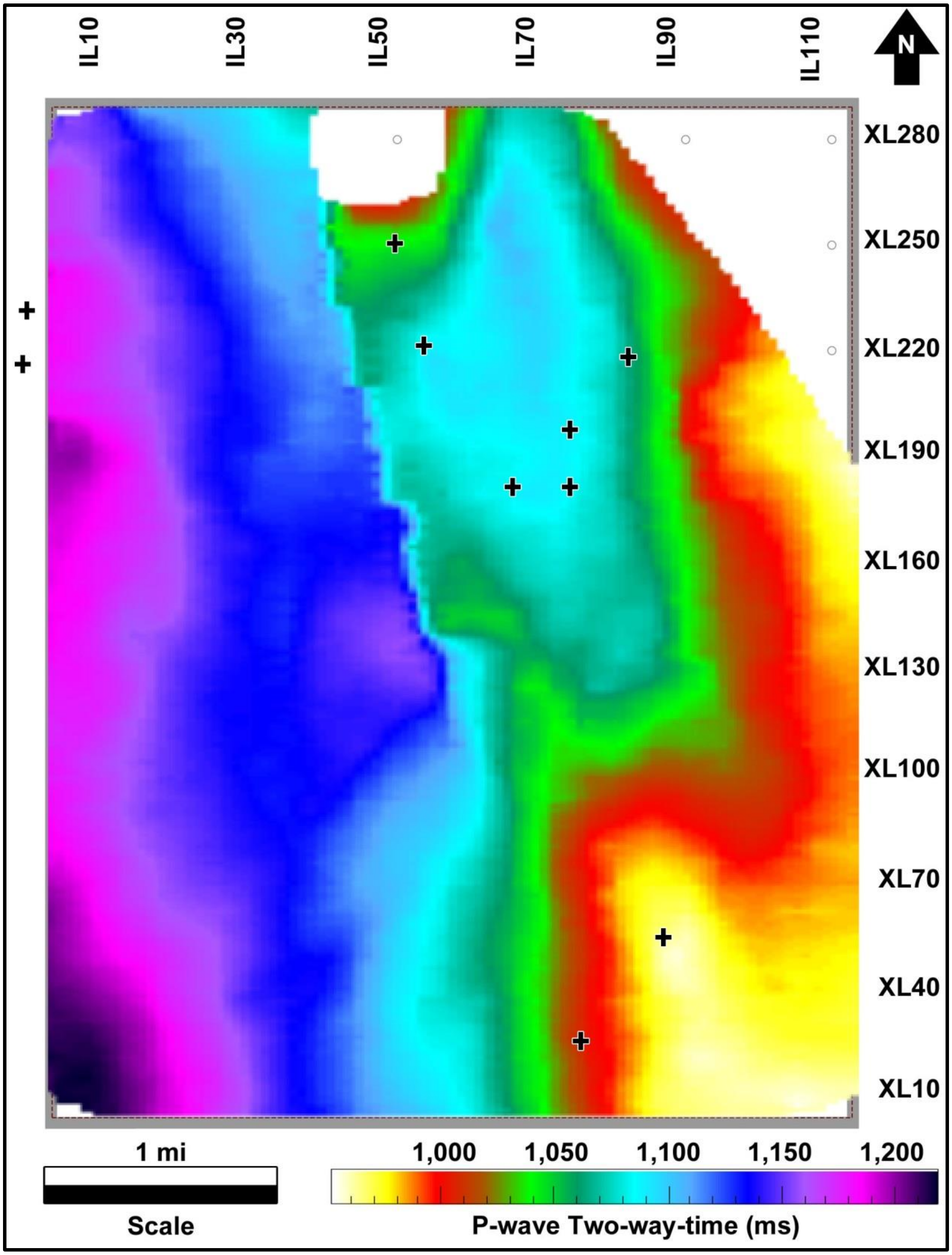

Figure 56. Time structure map for H5 in P-wave TWT.

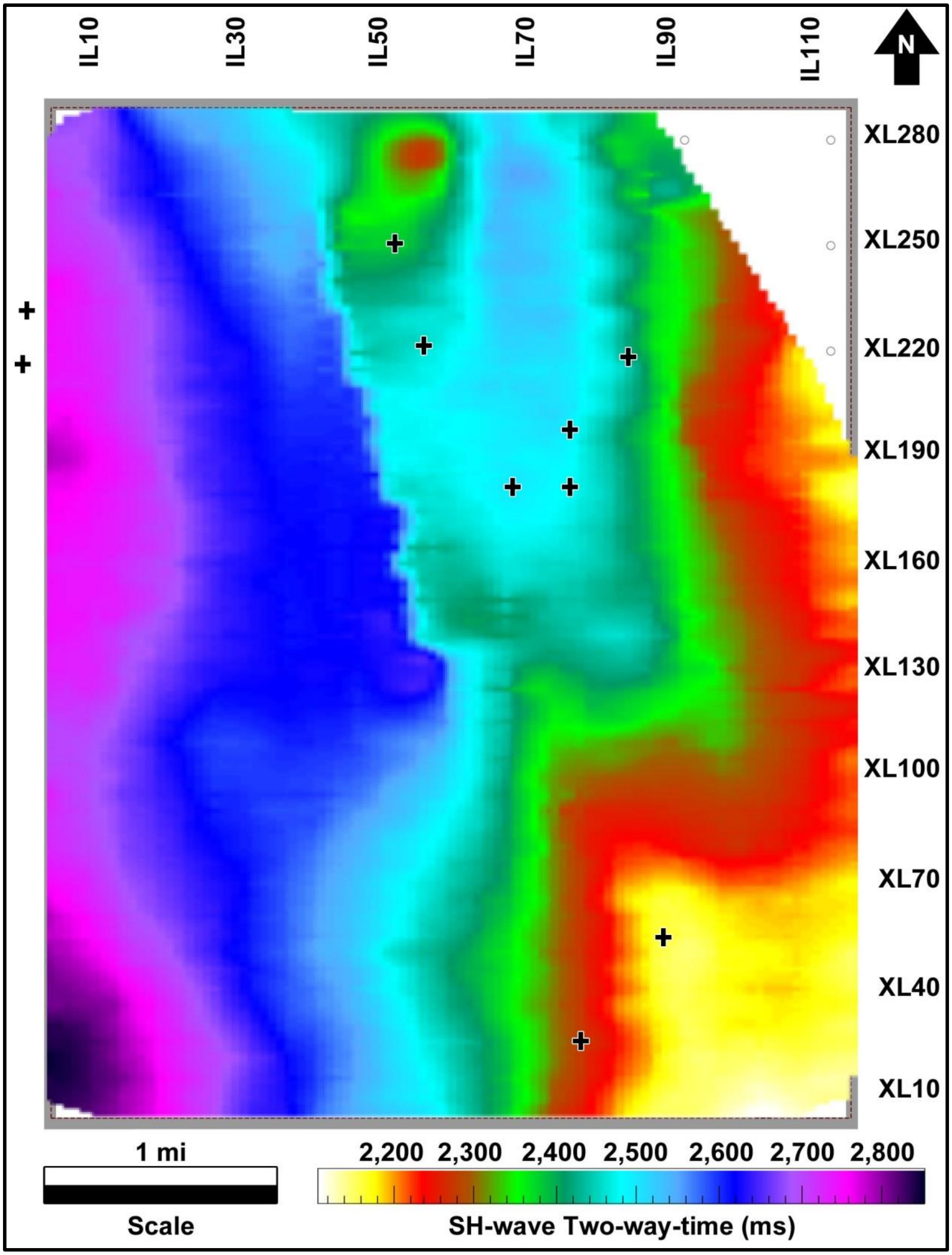

Figure 57. Time structure map for H5 in SH-wave TWT.

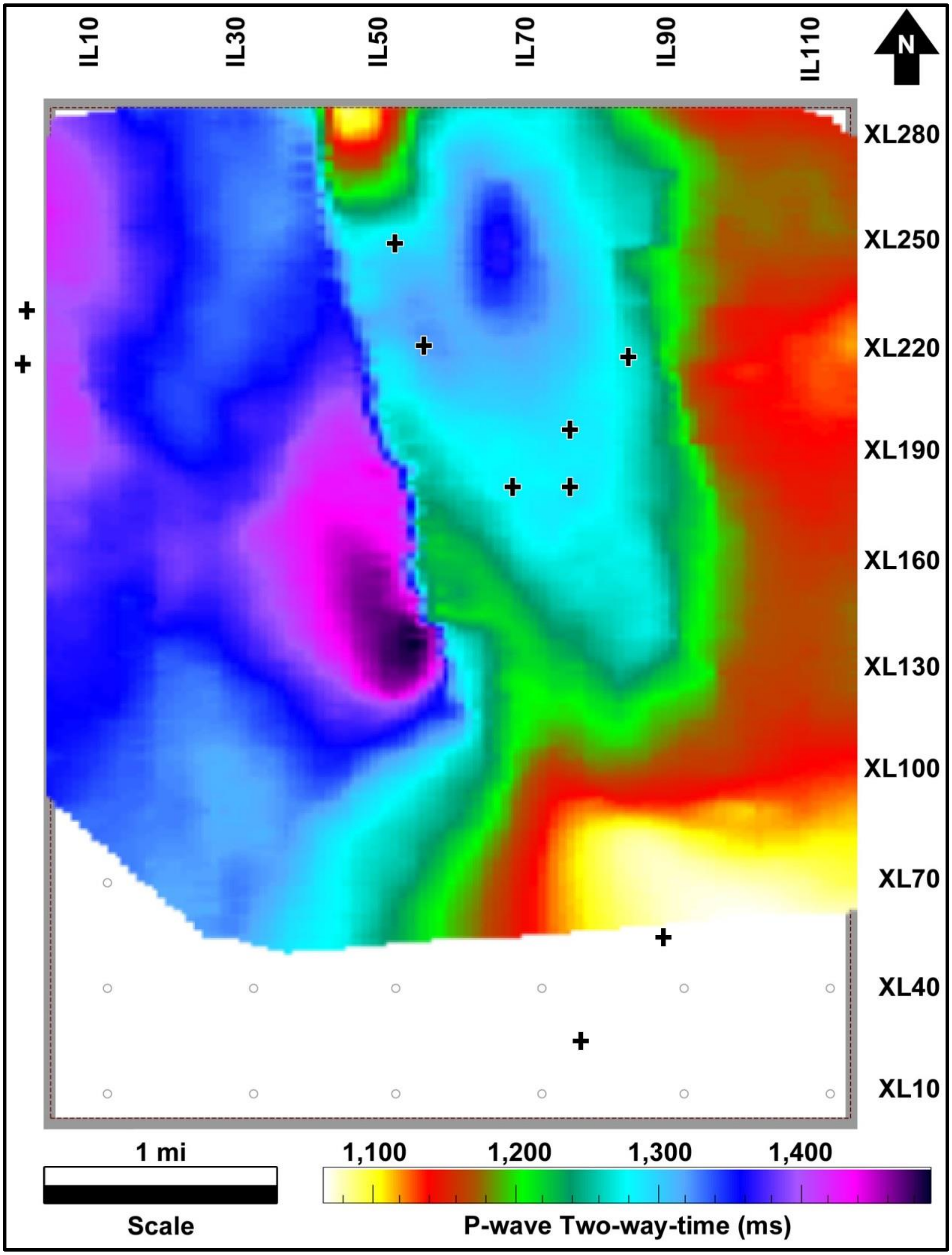

Figure 58. Time structure map for H6 in P-wave TWT.

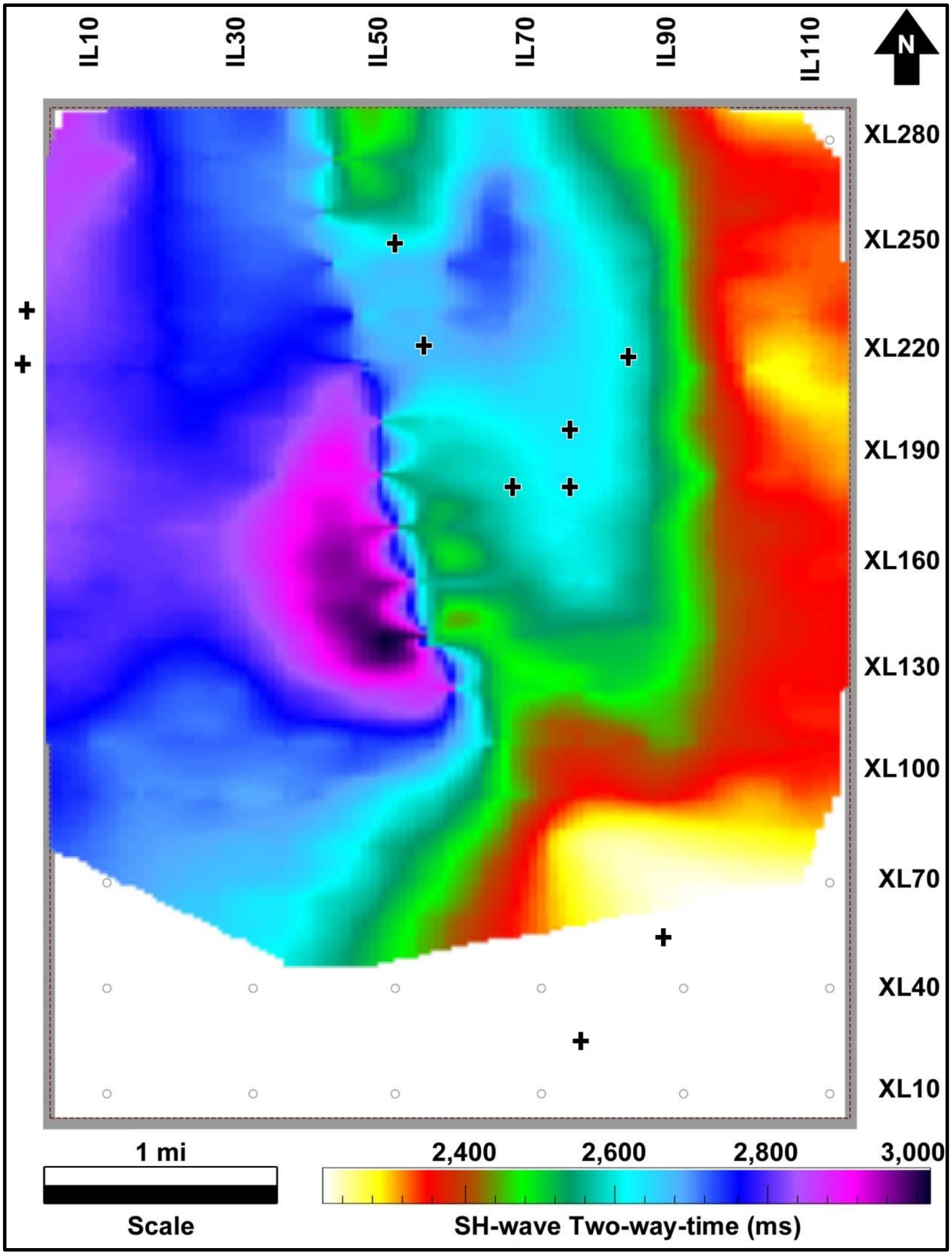

Figure 59. Time structure map for H6 in SH-wave TWT.

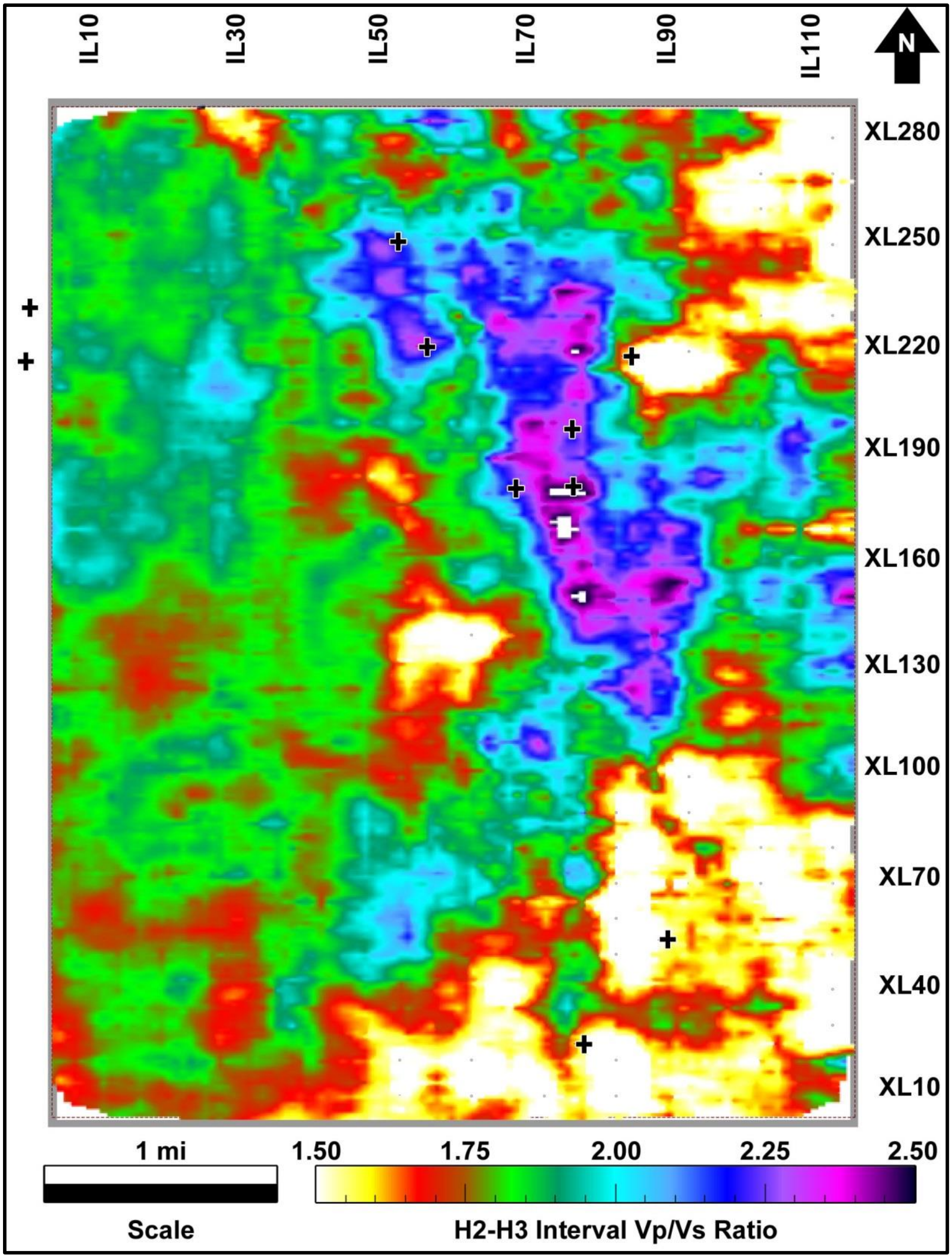

Figure 60. V_p/V_s in the interval between horizons H2 and H3.

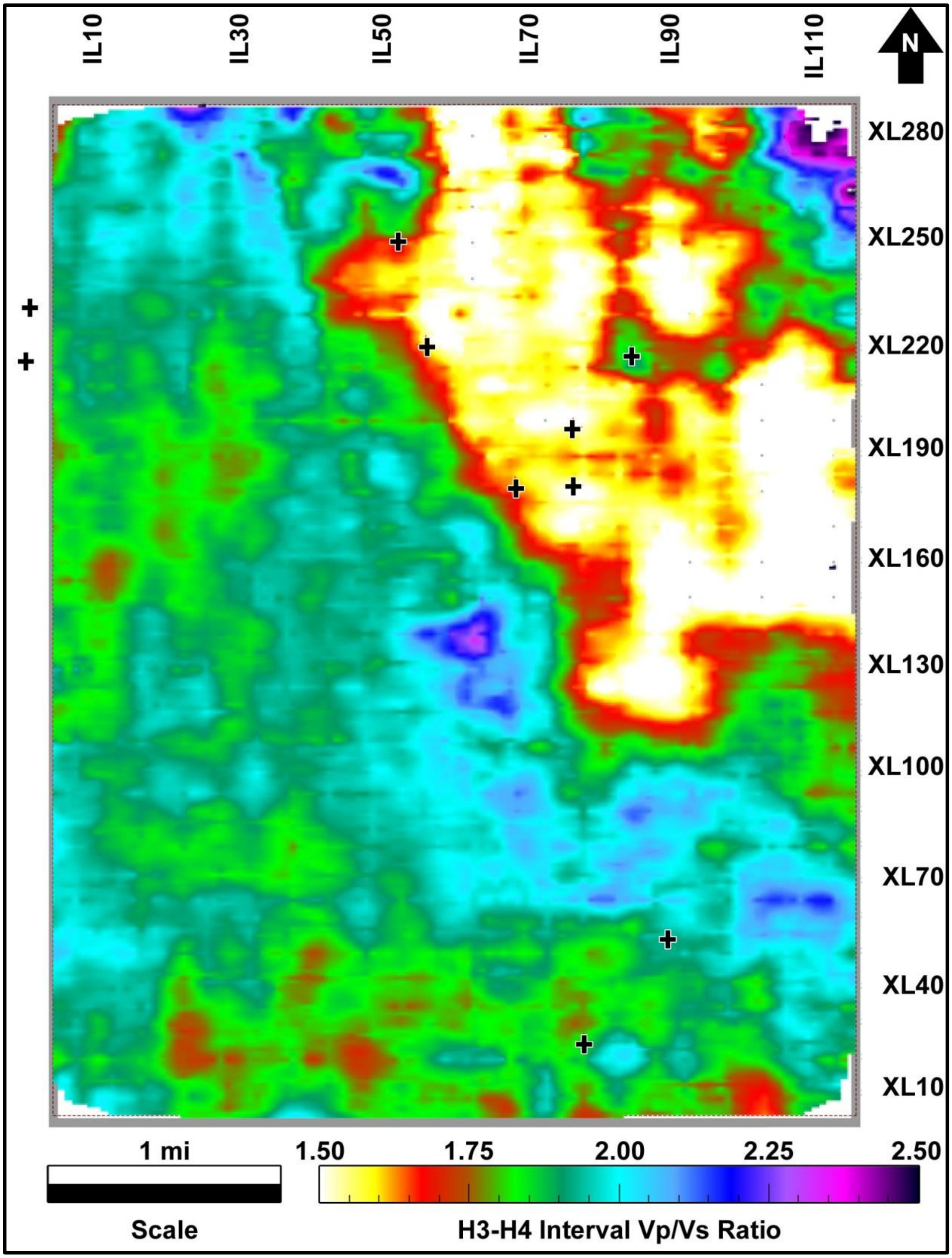

Figure 61. V_p/V_s in the interval between horizons H3 and H4.

Bibliography

Bahorich, M., and S. Farmer, 1995, 3-D seismic discontinuity for faults and stratigraphic features, the coherency cube: The Leading Edge, **14**, 1053–1058, doi: 10.1190/1.1437077.

Bennison, A. P., 1956, Springer and related rocks of Oklahoma: Tulsa Geological Society Digest, **24**, 111–115.

Billingsley, H. R., 1949, A subsurface study of the Sholem Alechem oil field, Stephens and Carter Counties, Oklahoma: Tulsa Geological Society Digest, **17**, 107–111.

Billingsley, H. R., 1956, Sholom Alechem oil field, Stephens and Carter Counties, Oklahoma, *in* SP 16: Petroleum Geology of Southern Oklahoma, Volume 1, American Association of Petroleum Geologists Special Volumes, 294–310.

Boyd, D. T., 2005, Oklahoma oil and gas production, its components and long-term outlook: Oklahoma Geology Notes, **65**, 4–23.

Branson, C. C., 1956, General geologic section of Oklahoma: National Oil Scouts and Landmen's Association Yearbook, **26**, 609.

Braun, J. C., 1961, A stratigraphic study of the Sycamore and related formations in the southeastern Anadarko Basin: The Shale Shaker Digest 3, **11**, 150–164.

Chopra, S., 2002, Coherence cube and beyond: First Break, **20**, 27–33, doi: 10.1046/j.1365-2397.2002.00225.x.

Cipriani, D., 1963, General geologic sections of Oklahoma and Northern Arkansas: Phillips Petroleum Company.

DeAngelo, M. V., and L. J. Wood, 2001, 3-D seismic detection of undrilled prospective areas in a mature province, South Marsh Island, Gulf of Mexico: The Leading Edge, **20**, 1282–1292, doi: 10.1190/1.1487261.

DeAngelo, M. V., M. M. Backus, B. A. Hardage, P. Murray, and S. Knapp, 2003, Depth registration of P-wave and C-wave seismic data for shallow marine sediment characterization, Gulf of Mexico: The Leading Edge, **22**, 96–105, doi: 10.1190/1.1559035.

Domenico, S. N., 1984, Rock lithology and porosity determination from shear and compressional wave velocity: Geophysics, **49**, 1188–1195, doi: 10.1190/1.1441748.

Fomel, S., and M. M. Backus, 2003, Multicomponent seismic data registration by least squares: 73rd Annual International Meeting, SEG, Expanded Abstracts, 781–784, doi: 10.1190/1.1818052.

Fomel, S., M. M. Backus, K. Fouad, B. A. Hardage, and G. Winters, 2005, A multistep approach to multicomponent seismic image registration with application to a West Texas carbonate reservoir study: 75th Annual International Meeting, SEG, Expanded Abstracts, 1018–1021, doi: 10.1190/1.2147852.

Gaiser, J. E., 1996, Multicomponent correlation analysis: Geophysics, **61**, 1137–1149, doi: 10.1190/1.1444034.

Gardner, G. H. F., L. W. Gardner, and A. R. Gregory, 1974, Formation velocity and density - the diagnostic basics for stratigraphic traps: Geophysics, **39**, 770–780, doi: 10.1190/1.1440465.

Hardage, B. A., 1997, Principles of onshore 3-D seismic design: Geological circular, Bureau of Economic Geology, University of Texas at Austin, GC9705.

Hardage, B. A., M. V. DeAngelo, P. E. Murray, and D. Sava, 2011a, Chapter 5: Depth registration of P and S data, *in* Multicomponent seismic technology: Geophysical References Series 18, Society of Exploration Geophysicists, 161–178, doi: 10.1190/1.9781560802891.ch5.

Hardage, B. A., M. V. DeAngelo, P. E. Murray, and D. Sava, 2011b, Chapter 3: Multicomponent data processing, *in* Multicomponent seismic technology: Geophysical References Series 18, Society of Exploration Geophysicists, 77–124, doi: 10.1190/1.9781560802891.ch3.

Hardage, B. A., M. V. DeAngelo, P. E. Murray, and D. Sava, 2011c, Chapter 1: Basic concepts, *in* Multicomponent seismic technology: Geophysical References Series 18, Society of Exploration Geophysicists, 1–30, doi: 10.1190/1.9781560802891.ch1.

Hicks, I. C., 1956, Geology of the Southwest Velma Field, Stephens County, Oklahoma, *in* SP 16: Petroleum geology of southern Oklahoma, Volume 1, American Association of Petroleum Geologists Special Volumes, 244–259.

IHS Energy, 2004, Data supplied by Petroleum Information/Dwights LLC dba IHS Energy Group, October 1, 2004.

Justice, M. G., M. D. McCormack, and S. S. Lee, 1987, Anisotropy in the Morrow formation of southeast New Mexico, *in* Danbom, S. H., and S. N. Domenico, eds., Shear-wave exploration: Geophysical Development Series 1, Society of Exploration Geophysics, 154–164, doi: 10.1190/1.9781560802761.ch4.

Kidd, G. D., 1999, Fundamentals of 3-D seismic volume visualization: The Leading Edge, **18**, 702–709, doi: 10.1190/1.1438362.

Kleen, H. J., 1994, Velma Sho-Vel-Tum field discovery: The Shale Shaker Digest 13, **44**, 329–331.

Marfurt, K. J., R. L. Kirlin, S. L. Farmer, and M. S. Bahorich, 1998, 3-D seismic attributes using a semblance-based coherency algorithm: Geophysics, **63**, 1150–1165, doi: 10.1190/1.1444415.

McCormack, M. D., J. A. Dunbar, and W. W. Sharp, 1984, A case study of stratigraphic interpretation using shear and compressional seismic data: Geophysics, **49**, 509–520, doi: 10.1190/1.1441686.

Murray, P. E., M. V. DeAngelo, B. A. Hardage, M. M. Backus, R. J. Graebner, and S. Fomel, 2003, Interpreting multicomponent seismic data in the Gulf of Mexico for shallow sedimentary properties, methodology and case history: Offshore Technology Conference, OTC 15118.

Nickel, M., and L. Sonneland, 2004, Automated PS to PP event registration and estimation of a high-resolution Vp-Vs ratio volume: 74th Annual International Meeting, SEG, Expanded Abstracts, 869–872, doi: 10.1190/1.1843330.

Pardus, Y. C., Conner J., Schuler N. R., and Tatham R. H., 1990, V_p/V_s and lithology in carbonate rocks: a case study in the Scipio Trend in Southern Michigan: 60th Annual International Meeting, SEG, Expanded Abstracts, 169–172, doi: 10.1190/1.1890101.

Paschal, E. A., 1941, Major tectonic provinces of Southern Oklahoma and their relation to oil and gas fields: American Association of Petroleum Geologists Bulletin, **25**, 1–22.

Robertson, J. D., 1987, Carbonate porosity from S/P traveltime ratios: Geophysics, **52**, 1346–1354, doi: 10.1190/1.1442247.

Rutledge, R. B., 1956, The Velma oil field, Stephens County, Oklahoma, *in* SP 16: Petroleum Geology of Southern Oklahoma, Volume 1, American Association of Petroleum Geologists Special Volumes, 260–281.

Sheffield, T. M., D. Meyer, J. Lees, G. Kahle, B. Payne, and M. J. Zeitlin, 1999, Geovolume visualization interpretation, color in 3-D volumes: The Leading Edge, **18**, 668–674, doi: 10.1190/1.1438352.

Sheriff, R. E., 2002, Encyclopedic Dictionary of Applied Geophysics: Society of Exploration Geophysicists, doi: 10.1190/1.9781560802969.

Sheriff, R. E., and L. P. Geldart, 1995, Chapter 2: Theory of seismic waves, *in* Exploration seismology, Second edition: Cambridge University Press.

Stommel, H. E., and J. M. Graul, 1978, Current trends in geophysics: 7th Annual Convention Proceedings, Indonesian Petroleum Association, 133–158.

SynTool^{TM} Software User Guide, 2010, Halliburton - Landmark Software and Services.

Tatham, R. H, M. D. McCormack, E. B. Neitzel, and D. F. Winterstein, 1991a, Chapter 4: Multicomponent seismic data acquisition techniques, *in* Multicomponent seismology in petroleum exploration: Society of Exploration Geophysicists, 13–42, doi: 10.1190/1.9781560802556.ch4.

Tatham, R. H, M. D. McCormack, E. B. Neitzel, and D. F. Winterstein, 1991b, Chapter 7: Multicomponent interpretation, Case Histories, *in* Multicomponent seismology in petroleum exploration: Society of Exploration Geophysicists, 187–244, doi: 10.1190/1.9781560802556.ch7.

The Oilfield Glossary, 2014, The Oilfield Glossary – Schlumberger, Schlumberger Oilfield Resources, Accessed March 17, 2014, http://www.glossary.oilfield.slb.com/.

U.S. Crude Oil, Natural Gas, and Natural Gas Liquids Proved Reserves, 2009, United States Energy Information Administration, http://www.eia.gov/naturalgas/crudeoilreserves/archive/2009/cr2009.html.

Van Dok, R., and P. Kristiansen, 2003, Event registration and V_p/V_s correlation analysis in 4C processing: 73rd Annual International Meeting, SEG, Expanded Abstracts, 785–788, doi: 10.1190/1.1885425.